EXPERIMENTAL CHARACTERIZATION AND VALIDATED MULTI-FIDELITY ANALYSIS OF RECONFIGURABLE CURVATURE IN SHAPE MEMORY ALLOY COMPOSITE SHEETS

A Thesis

by

AARON CARL POWLEDGE

Submitted to the Office of Graduate and Professional Studies of
Texas A&M University
in partial fulfillment of the requirements for the degree of

MASTER OF SCIENCE

Chair of Committee,	Richard J. Malak
Co-Chair of Committee,	Darren J. Hartl
Committee Member,	Daniel A. McAdams
Head of Department,	Andreas Polycarpou

May 2015

Major Subject: Mechanical Engineering

ABSTRACT

Model validation is often a critically important part of the design process where physics-based models are utilized to explore varying design parameters. Without validating a model with experimental data, it is difficult to determine the usefulness and appropriateness of the model for its intended purposes. This work proposes a framework for validating physics-based models for self-folding laminate structures which employ active materials to achieve deformation. The framework utilizes 3D digital image correlation techniques as a means of capturing physical deformations in physical space to compare to data generated by traditional modeling methods, including finite element analysis simulations and system performance predictions which are based on classical laminate beam theory. Comparisons between models and the physical system are prepared by calculating the mean Hausdorff distance between the three dimensional surfaces, a method proven to be mathematically reliable for shape matching between objects. This distance metric, implemented along with a visualization tool, provides a fast and intuitive means for judging how well the physics-based model approximates the real system, and allows for models of varying fidelity to be easily compared.

Such an assessment effectively facilitates studies of modeling tradeoffs between accuracy and resource cost – a tradeoff must be made at some level for almost every type of system being modeled, to allow for engineers to make an informed design decision. Though this work follows the development of a particular shape memory alloy based self-folding laminate system, the methodology and process described are

applicable to other types of systems concerned with a changing surface curvature in the system being simulated. The work also describes details and methods considered for fabrication and testing of the laminate specimens considered herein, creating and implementing the physics based models, and considers the verification and validation of the tool which assesses and compares the experimental and simulated results.

ACKNOWLEDGEMENTS

I would like to thank my committee co-chairs, Dr. Richard Malak and Dr. Darren Hartl, and committee member Dr. Daniel McAdams, for their guidance and support throughout the course of this research.

Thanks also go to my friends and colleagues and the department faculty and staff for making my time at Texas A&M University a great experience. Finally, thanks to my mother and father for their encouragement and to my wife for her patience and love.

NOMENCLATURE

ρ	Density
E_A, E_M	Modulus of Elasticity
ν_A, ν_M	Poisson's Ratio
α_A, α_M	Coefficient of Thermal Expansion
A_f	Austenite Finish Transformation Temperature
A_s	Austenite Start Transformation Temperature
M_f	Martensite Finish Transformation Temperature
M_s	Martensite Start Transformation Temperature
C_A, C_M	Stress Influence Coefficient
n_1, n_2, n_3, n_4	Transformation Hardening Exponents
H_{Max}, H_{Min}	Transformation Strain
k_t	Transformation Strain Parameter
k	Thermal Conductivity Coefficient
c_p	Specific Heat
d	SMA Wire Diameter
N	Discretization Points Per Dimension Used in MHD Calculation

TABLE OF CONTENTS

Page

LIST OF FIGURES

Page

LIST OF TABLES

Page

1. INTRODUCTION

1.1 A NEED FOR VALIDATION

Engineers and designers often desire to create models to understand and predict the behavior of complex systems. Models allow one to explore the impact of varying certain design parameters on the system's performance without the need to dedicate as much time or as many resources to building and testing physical representations for each case of interest. However, developing and testing specimens physically similar to those being simulated is still critically important for establishing the extent to which a model reflects the real system it represents. Measurements of the real system allow one to build trust that a model is capable of sufficiently predicting system behavior within the realm of design parameters in which it has been validated.

Before relying upon a physics-based model to predict system behavior, one should appropriately validate the model using experimentally collected data from a real implementation of the system. Failure to properly validate a model can lead decision makers to trust simulation predictions inappropriately – a mistake that may often carry severe penalties.

In order to establish trust in a model, both verification and validation steps should be taken. Verification is the process of ensuring that a conceptual model has been transferred into a calculable model in such a way as to faithfully represent what the mathematical model is intended to represent. Validation is the process of ensuring that the model implementation is sufficiently accurate to be used for its intended purpose [1].

While it is important to remember that there is no such thing as a model which is 100% accurate, a model is useful if it is accurate enough to provide useful information.

The degree of accuracy required for a model depends upon the intended use of the model output. Someone seeking to use a model to predict something with a very high precision would likely require much greater accuracy from their model than someone trying to get a “ballpark” estimate on a system’s performance. Often there is a tradeoff between how accurate a model can be and the time and resources required to obtain the model output. Frequently, a faster but less accurate model is actually more useful during early stages of development. Designers need to decide what level of accuracy and precision they require from their models. This decision allows them to have a standard by which a model may be validated.

For complex system behavior, it is often difficult to sufficiently capture all of the important factors which impact the dynamic behavior of the system. This makes it difficult to accurately predict the behavior of the system, increasing the value of performing experimental testing to validate the model against physical specimens to improve faith in the accuracy of the model.

1.2 VALIDATION FRAMEWORK

It is the goal of this work to establish a framework which can be implemented for experimentally measuring, characterizing, and analyzing deforming surface topography such that experimental data can be used to judge the effectiveness of physics-based models for predicting system behavior. Although it is often desirable to use high fidelity

models to explore the system design space, rather than needing to conduct experimental trials for all cases of interest, models must first be characterized and validated across a range of design parameters before they may be considered useful for simulating system behavior without additional verification through experimentation. To this end, the framework presented in this work continues beyond methods of measurement and analysis of physical specimens to consider processes and metrics sufficient for comparing measured and simulated system behavior. Additionally, these metrics are applied in the comparison of measured and modeled data, and physics-based models of the system are characterized so as to examine the effects of implementing the models under differing assumptions and techniques. Doing this allows us to characterize and analyze the properties unique to the particular application of the framework application investigated in this work, which helps to provide a context for assessing how the models might appropriately be used and re-used for this application [2, 3]. Through this process, validation of system models may be pursued by using a number of different experimental samples to establish a context in which the model's usefulness is assessed – this is important to establish as failing to consider the context in which a model is validated can lead to unjustified engineering decisions [4].

Although model validation typically considers whether or not a model is sufficient for a particular application, this work seeks to characterize multiple different physics-based model implementations rather than define a single particular application's requirements as a basis of validation. In this way, focus is placed on characterizing aspects of the modeling process – this model characterization is important for

understanding the effect of utilizing various different modeling assumptions and techniques, and is significant when considering validating models for a specific purpose, as some applications may require greater model fidelity than other applications. Through characterizing the tradeoffs in modeling the system presented in this work, the usefulness of applying the validation framework for model assessment is demonstrated.

At a high level, the modeling process may be generalized to encompass the interactions between a conceptual model, a problem entity, and a computerized model. Figure 1 denotes the interactions between these components. The conceptual model is the theoretical representation of a given system, the problem entity is the physical implementation of the conceptual model, and the computerized model includes physics-based simulations of the system. Between these three components, the conceptual model validation considers the determination that theories and assumptions underlying the conceptual model are correct and reasonable for the intended application and implementation, which is done through analysis and modeling [5]. Computerized model verification is the process of ensuring that the models used to predict and simulate system behavior are implemented and reflect the system as intended – this can be done through creating or developing the code used to simulate the system and ensuring that it is implemented as anticipated. Operational validation is concerned with determining that the computerized models can predict system behavior with sufficient accuracy for the intended purpose of the model's output; operational validity is assessed by carrying out experiments to compare simulation results to measured data from the physically implemented system. The framework of methods presented in this work are used to

assess this operational validation step through measuring system surface deformations in three dimensions and comparing measured surface deformations to predicted deformations through metrics which are useful for characterization and analysis of folding actions in self-folding composite systems.

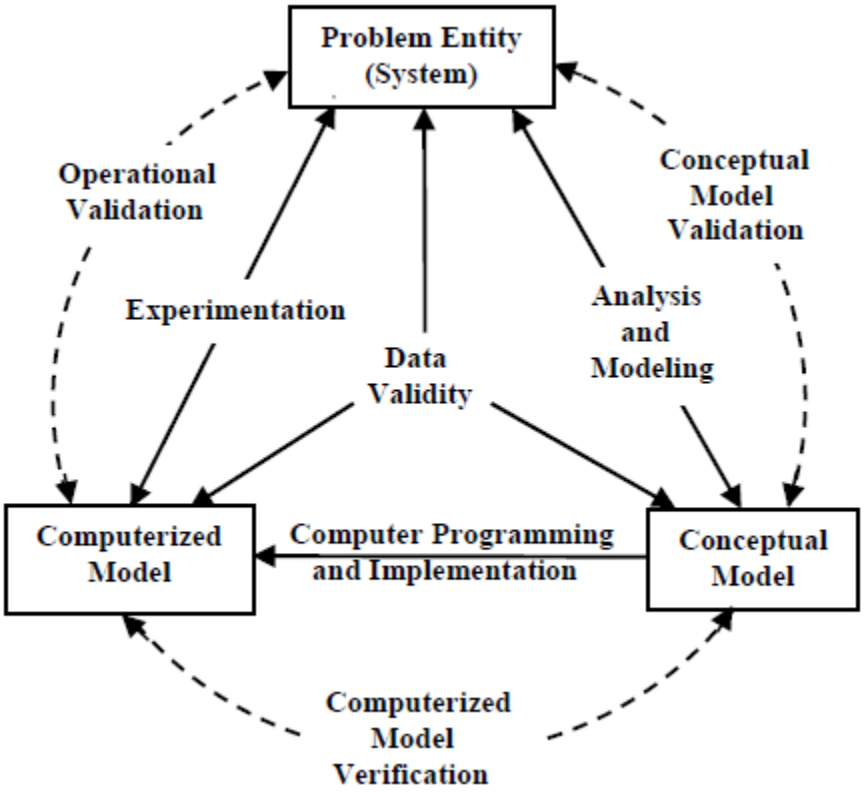

Figure 1. Generalized model process interactions [5].

This work specifically considers the development of a framework for measuring local surface curvature of a self-folding laminate structure for the purposes of validating physics-based models of the laminate. The framework is developed and implemented

with regards to a particular shape memory alloy based self-folding laminate concept under development by a team at Texas A&M University [6-12], but the methods involved may extend to other works where local surface curvature measurements are important for model validation. As the methods discussed herein were developed with regards to a particular laminate concept, the details of the design concept will be discussed throughout this work, as testing performed on the laminate specimens effectively serves as a case study in which the methods may be examined. The framework aims to aid in evaluation of physics-based models for which physical data exists, to provide both quantitative and qualitative feedback about how well the model matches the physical system.

The laminate structure utilized in the development of the framework considered here was proposed by a team at Texas A&M University [6-12], and is supported by funding provided by the National Science Foundation and Air Force Office of Scientific Research. The origami inspired laminate design uses shape memory alloy (SMA) wire to achieve reconfigurable self-folding. The laminate consists of two SMA wire meshes separated by a passive compliant medium. This pliable medium consists of an elastomeric material which acts to thermally separate the SMA layers such that local regions on either side of the laminate may be thermally actuated with minimal thermal bleed through to the opposing side of the laminate. This allows the SMA meshes to be thermally actuated separately, giving the laminate structure the ability to generate compound folding behavior. The SMA laminate concept will be discussed in Section 1.4.

The bulk of this work will consider the application of the framework to the specific case of this SMA laminate concept. However, the process used here is applicable to other systems with deforming surface topography, and the methods presented for comparing data from multiple experimental trials and multiple simulations are more broadly applicable to systems beyond the SMA laminate concept. At a high level, the process undertaken through application of the framework can be thought of as three distinct steps, as shown in Figure 2.

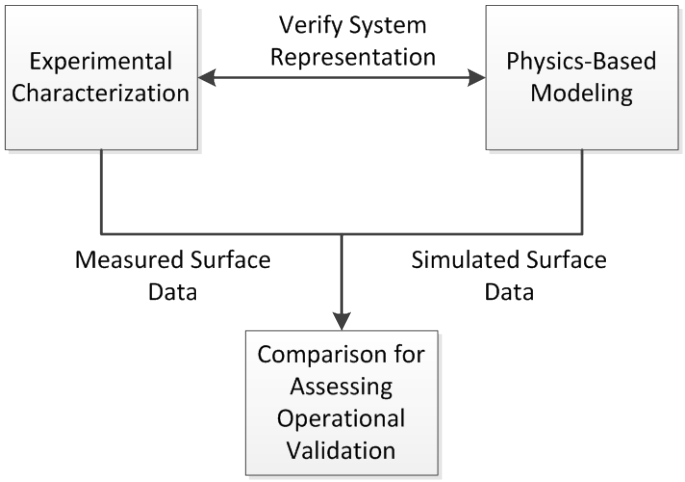

Figure 2. General application of validation framework.

Experimental characterization involves the steps and methods taken to characterize and analyze the system behavior; for the SMA laminate concept, a simplified configuration allows for the characterization of a single folding action, while more complex configurations allow for compound and complex folding actions. Measurement techniques capable of measuring three dimensional deformations and

metrics sufficient for characterizing the tightness of folding, and for capturing and comparing small differences in surface topology are used to convey measurable system performance. Physics-based modeling involves the creation of simulations for predicting system behavior. Characterizing the impact of utilizing various modeling assumptions and techniques allows for one to consider how best to approach developing a model which is sufficiently accurate for a given application. From experimental characterization and physics-based modeling, we obtain data representing system performance – once both of these steps have been taken comparisons can be made to assess how well the simulations predict measurable system performance. This comparison of measured and simulated surface data is the heart of operational validation; a shape matching metric is employed to quantify the difference in measured and predicted system behavior so that conclusions may be drawn regarding the model's usefulness. Much of this work is dedicated to detailing how these steps are applied for the case of the SMA laminate system.

1.3 BACKGROUND ON SHAPE MEMORY ALLOYS

Much of the work detailed here depends upon the implementation of shape memory alloy (SMA) wire, which is embedded in the laminate specimens and used as an actuator to achieve folding behavior. As such, it is important to establish a basic understanding of fundamental SMA behavior. SMAs are a type of active material. Active materials exhibit a mechanical response to non-mechanical fields, typically orders of magnitude greater than responses from conventional materials [13, 14]. This

allows SMAs to be particularly effective actuators – the tight coupling between thermal and mechanical fields means that SMAs can generate mechanical deformation under thermal loading.

SMAs also exhibit what is known as the shape memory effect: If the SMA is deformed from the twinned martensitic phase and then unloaded at a temperature below the austenite start transformation temperature (A_s), when it subsequently undergoes heating to a temperature above the austenite finish transformation temperature (A_f) it regains its original shape upon transforming back into the austenitic phase [13, 14]. This shape memory effect can be illustrated by following a thermo-mechanical loading path through stress-strain-temperature space such as the path shown in Figure 3: starting from the austenitic phase, the SMA is cooled while stress free, so that the SMA forms twinned martensite. From the twinned martensitic phase, the SMA is then loaded isothermally until it forms detwinned martensite. The material is then elastically unloaded but remains in the detwinned martensitic state. By now heating in stress free conditions to a temperature above A_f, the SMA transforms back into the austenitic phase as it began.

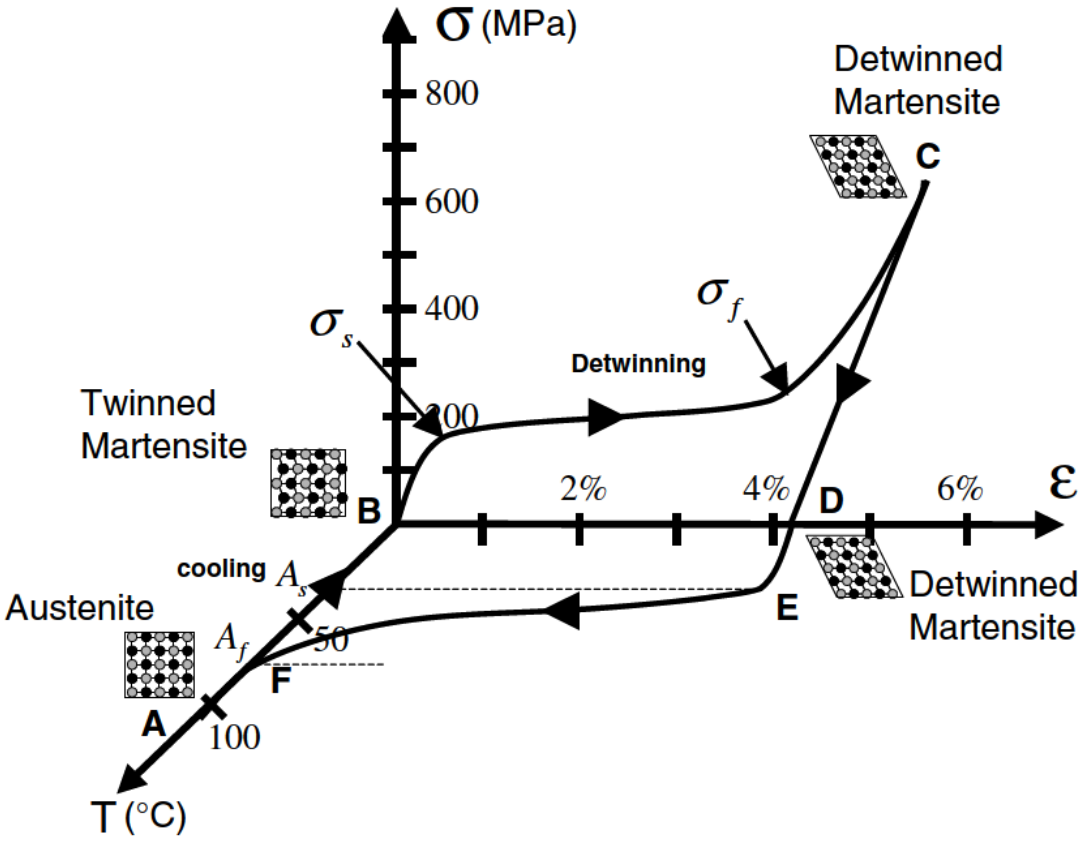

Figure 3. Exhibited shape memory effect typical for a NiTi SMA material [13].

The shape memory effect can also be observed from heating and cooling under isobaric loading conditions. For a sample under constant stress, the shape memory effect provides nearly complete strain recovery. Figure 4 illustrates the strain recovery from heating and subsequent cooling of the SMA at constant stress. The ability of SMA material to exhibit this shape memory effect is useful for creating the reconfigurable folding in the self-folding laminate concept mentioned in Section 1.2, as this effect is what allows the laminate sheet to return to an unfolded state upon cooling, recovering

the strain induced during transformation.

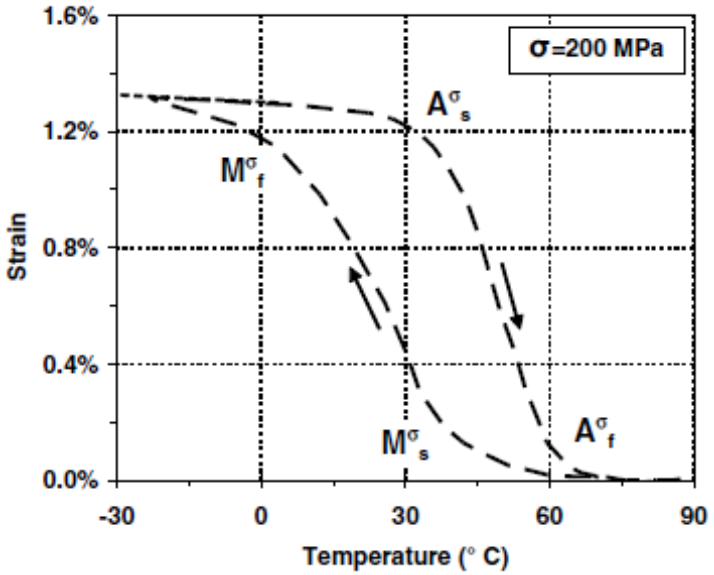

Figure 4. Strain recovery of NiTi SMA during heating and cooling under isobaric loading conditions [13].

Of the many different possible SMA compositions, NiTi SMAs are used in the greatest number of commercial applications. The alloy system's strong two way shape memory effect, pseudoelastic behavior, corrosion resistance, and biocompatibility make it an ideal candidate for a variety of industries ranging from medical devices to aerospace applications.

NiTi SMA and other active materials have been used as actuators in a number of morphing systems [7, 8, 11-23]. These include the use of piezo-composites in the development of a biomimetic wing section [17], the use of $Ni_{60}Ti_{40}$ SMA in morphing

aerospace structures [16], and smart composite plates for active buckling control [15]. SMA actuators have been further investigated with regards to the development of models and simulations to better understand smart material structures generally – pointing to cases such as adaptive aircraft wing control, control of segmented robotics for locomotion, and inclusion of SMA actuators in microelectromechanical systems [14, 18]. The fact that the behavior of NiTi SMAs has been well studied and that they are suitable for a wide range of applications make NiTi SMAs an ideal choice for consideration as an actuator material in the laminate system considered in this work.

1.4 SELF-FOLDING LAMINATE SYSTEM

A team at Texas A&M University has begun development of a novel concept for an origami-inspired SMA actuated laminate structure, which is capable of enacting reconfigurable fold-like operations in order to change its shape. Reconfigurable self-folding capabilities have potential applications for emerging technologies in a range of fields, and are especially desirable for remote applications such as in space or underwater [7, 8, 11-13, 16, 19-22].

The laminate concept consists of a pliable elastomer mid-layer, and outer layers each containing a SMA wire mesh. Each of the meshes is comprised of two sets of pre-strained NiTi SMA wires, interwoven with equal spacing between wires. The two meshes on either side of the compliant layer are offset by half of the wire spacing so as to minimize thermal effects between meshes. The general design of this laminate concept is shown below in Figure 5.

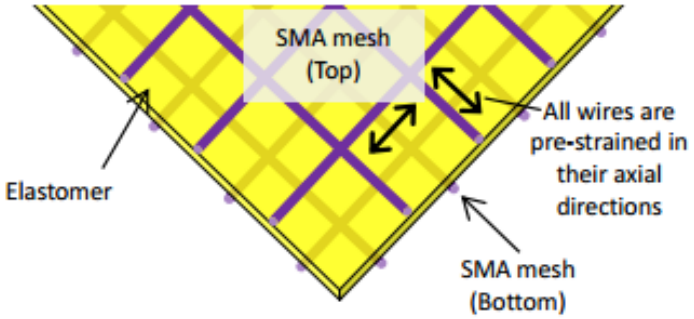

Figure 5. General Schematic of the SMA-based laminate [12].

When local regions of the laminate are heated such that the SMA wire transforms, a deformation is induced in the SMA wires which causes fold-like behavior in the laminate sheet. By controlling the heating of localized regions of the sheet, it is possible to cause the laminate to move in ways that allow for single or compound folding, which can be controlled to direct the laminate to take on a desired shape. Figure 6 illustrates how localized heating of the SMA wires might be used to induce folding behavior in the composite.

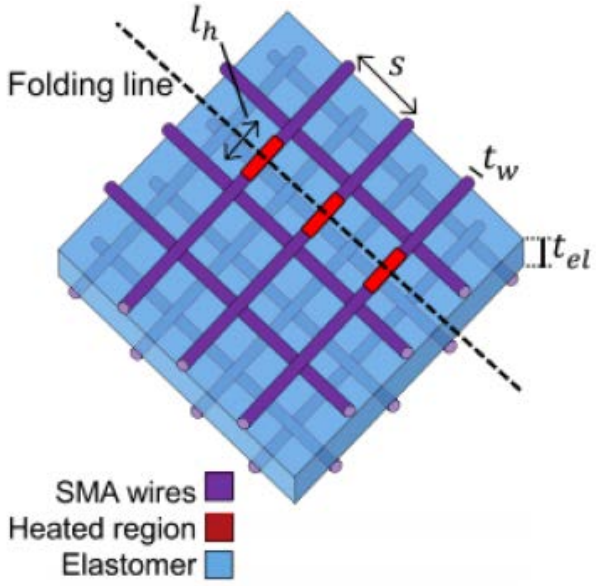

Figure 6. Schematic of the SMA based laminate folding [12].

A variation of this design that is considered in this work is a “reduced complexity” laminate specimen. This variation of the design incorporates an SMA mesh on only one side of the elastomer layer. Further, instead of having wires running in orthogonal directions, the reduced complexity case consists of wires embedded in only a single axial direction. A schematic of the reduced case is shown in Section 2 with a more complete description.

This simplified case is an important starting point for validation of the laminate design, as it can be actuated by external means, such as by uniform convective heating, reducing the number of factors which could potentially affect the performance of the laminate. For a laminate with wires in more than one axial direction, or with wires on opposing sides of the elastomer, heating the specimen could cause the laminate to

contract such that some wires oppose the motion of other wires in the specimen. This effect is useful for creating compound folding, or “bowl” curvature in the sheet, but can complicate measurements of how thermal energy input directly influences actuation of the sheet in a single direction.

For the reduced complexity case, since the wires are all parallel to one another, the specimen can be heated by external means, and the entire laminate can be expected to fold uniformly by contracting along the axial direction of the wires. Unlike more complicated cases of the laminate design, confining folding motion to a single direction with the reduced complexity case does not require control of localized heating with on-board heaters. Instead, the reduced complexity laminate specimens can be placed in an enclosure whose temperature is uniformly heated above the transformation temperature of the SMA. By doing this, the entire specimen can be actuated controllably and predictably. By ensuring that the specimen is visible in such an enclosure during this process, data can be captured using visual measurement techniques such as three-dimensional digital image correlation (3D DIC).

1.5 PHYSICS-BASED MODELING

In an effort to explore the design space and to study various implementations of a given system without requiring lengthy or expensive testing, it is often desirable to develop models which can be reliably utilized to predict system behavior. To this end, finite element analysis tools or analytical models are often utilized to create simulations to represent the physical phenomena occurring in the real system.

To model the SMA-based laminate system, two approaches are employed in this work. First, a finite element analysis (FEA) script was developed to model the laminate system. This approach is commonly followed in both research and industry environments and was pursued as it represents a standard modeling approach. Scripting in the Python programming language allowed commands to be directed to Abaqus, a widely employed FEA tool, which was used in conjunction with a user-defined material subroutine (UMAT) to appropriately handle the material properties of the SMA during transformation conditions. Using this approach allowed for standardized scripts to be developed to consistently create models which accurately represented the laminate system's design and conditions during testing, and tailor material properties to the properties match the values of the materials used during experimental trials. Overall, the development of the FEA scripts provided a way to model the physical system high fidelity. The FEA models will be discussed in greater detail in Chapter 4.

Second, a more simplified analytical approach was considered. To understand how such a system might behave in a less computationally intensive fashion than FEA modeling might yield, researchers from Texas A&M University developed a model which draws upon classical laminate plate theory (CLPT) to predict a uniform curvature response generated by actuating a laminate system like the one previously described [6, 7]. The CLPT model considers fully non-linear stress distributions and is capable of handling hysteretic SMA constitutive behavior. This model was validated against corresponding high-fidelity FEA models to produce predictions of system behavior with less than 10% normalized RMS error for several cases [6]. By adapting this model to

match the material properties and environmental conditions used in FEA models and in experimental testing, this method can also serve as a means of predicting system behavior by implementation of a physics-based model. This CLPT model and its implementation will be discussed further in Chapter four.

1.6 SHAPE COMPARISON USING HAUSDORFF DISTANCE METRIC

A quantitative metric is desired to succinctly capture the difference over the entire area of each of the compared surfaces. Although the radius of curvature measurement is sufficient as a performance metric for conveying the general tightness of folding behavior for reduced complexity samples, it cannot convey subtle changes in surface topography. A metric which provides a measure of shape matching over the entire surface is more desirable for cases where samples may exhibit non-uniform folding, including lateral twisting or compound folding. Development of the SMA laminate concept seeks to allow for compound folding to be achieved such that the laminate may be caused to fold into useful structures. A metric such as the Hausdorff distance measurement allows for shape comparison that goes beyond a single fold or uniform folding and is more adept at comparing complex geometry. The Hausdorff distance is a measure of the closest distance between a point on one surface and the closest possible point on the adjacent surface. The *mean* Hausdorff distance provides a measure of the average distance between a given point on one surface and the other surface. This average value is useful as a measure of how closely the surfaces are similar

in shape; two identical surfaces overlaid upon one another would have a mean Hausdorff distance of exactly zero.

For measuring the approximation error between the real surface data taken from experiment and the surface predicted by FEA models of the laminate system, the mean Hausdorff distance (MHD) was used. The mean Hausdorff distance has been provably demonstrated in other applications to be an effective metric by which images can be compared to provide a measure of shape similarity [24-29]. The MHD is applied here to provide a measure of shape similarity between overlaid surfaces, allowing for a comparison to be made between experimental and modeled surface data.

For the discussion of the distance measurement, we assume that for any two points a and b, the distance between the two points is defined as the Euclidean distance $d(a,b) = \big||a-b|\big|$. Given a point p and a surface S, represented by a set of n points such that $S = \{s_1, \dots, s_n\}$, the distance between the point p and the surface is defined as

$$e(p,S) = \min_{s \in S} \big||p-s|\big|, \tag{1}$$

where $e(p,S)$ is the Euclidean distance between point p and the closest point on surface S in Euclidean space, E^N, where N is the number of dimensions. A one sided distance between two surfaces S_1 and S_2 can then be defined as

$$E(S_1,S_2) = \max_{p \in S_1} e(p,S_2), \tag{2}$$

which is the greatest distance between a point p on surface S_1 and its closest neighboring point on surface S_2. It is important to note that the one sided distance is not generally symmetrical; the one sided distance taken from a point p on surface S_1 to the surface S_2 is not necessarily equal to the one sided distance from a point p' on surface S_2 to the

surface S_1. This non-symmetrical relationship is illustrated in Figure 7, where the one sided distances taken from two surfaces are not equal, meaning $E(S_1, S_2) \neq E(S_2, S_1)$.This is because the distance $e(b, S_2) < e(a, S_1)$.

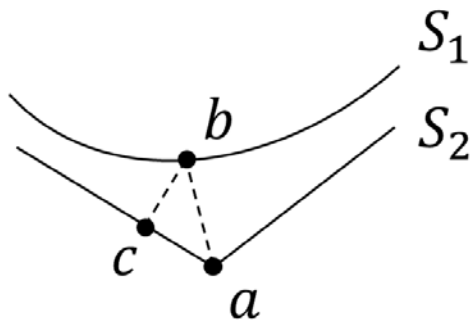

Figure 7. Non-symmetrical nature of one sided distance measurements.

The two sided Hausdorff distance is taken to be the greater of the one sided distances between surfaces, which is the maximum of $E(S_1, S_2)$ and $E(S_2, S_1)$. The mean distance between the two surfaces then is the surface integral of the distance divided by the area of the surface:

$$E_{mean}(S_1, S_2) = \frac{1}{|S_1|} \int_{S_1} e(p, S_2) ds. \quad (3)$$

Now, the two sided mean Hausdorff distance between the two surfaces can be defined as the maximum of the opposing one sided mean distances:

$$H_{mean}(S_1, S_2) = \max[E_{mean}(S_1, S_2), E_{mean}(S_2, S_1)]. \quad (4)$$

The mean Hausdorff distance (MHD) provides a measure of geometric difference between two surfaces. As such, when utilized for comparing two nominally similar

surface topologies, it is useful for providing a quantified measure of how much they differ. Ideally a perfect model would be able to supply the exact same surface prediction as is measured in physical trials. In such a case, where two identical surfaces, $S_1 = S_2$, were oriented and translated to a common origin and coordinate axes, the surfaces would exactly overlay one another with no difference between them. In this scenario, the two sided mean Hausdorff distance between the surfaces would be zero; $H_{mean}(S_1, S_1) = 0$ for an ideal case. The MHD is often preferred to the classical Hausdorff distance as the MHD is less sensitive to outliers or noise in the data [28].

1.7 ORGANIZATION OF FOLLOWING WORK

The remainder of this work follows the conceptual development of the SMA laminate concept, application of 3D digital imaging techniques for experimental data collection, physics-based modeling for prediction of system behavior and exploration of the design case, and novel application of a validation framework for smart material based structures. The validation considers the mean Hausdorff distance measurement as a more complete means of comparing simulation data to experimental trial data. This measurement has been reliably used in other fields as a basis for conducting shape comparison measurements, and is proposed as a basis for establishing an effective and intuitive surface comparison by which the validity and usefulness of a physics-based model may be judged for predicting feasible system behavior. After discussion of the aforementioned concepts, the extension of this framework to other works is established.

These topics are organized as follows: Chapter 2 introduces and discusses the materials and fabrication techniques utilized in the production of the physical SMA laminate specimens. Chapter 3 discusses the use of 3D DIC as a means of capturing system deformation in three dimensions, presents the methods used in experimental trials of the SMA laminate samples and the results of experimentally measuring the deformation of specific laminate samples. Chapter 4 of this work presents and discusses methods used to develop high fidelity physics-based models of the laminate system, focusing on two main approaches: finite element analysis (FEA) models, and a reduced order analytical model applying classical laminate plate theory. Chapter 4 also presents the system behavior predicting by six different physics-based model implementations of the laminate system. Chapter 5 introduces the validation framework in greater detail and describes the implementation of MHD calculations. The chapter also presents and discusses the results of carrying out the comparison of model and experimental data for the basis of validating the physics-based models. Finally, in Chapter 6, conclusions are drawn regarding both the methodology and the results presented in this work, and considerations are made for application of the techniques beyond the SMA laminate system concept.

2. FABRICATION AND MATERIALS

Before discussing how physical specimens are tested and analyzed, it is important to consider how the conceptual model is implemented. This chapter will detail how samples are developed and fabricated for testing, present the material properties as measured through characterization experiments and used in physics-based modeling, and discuss the SMA laminate variants to be investigated. This chapter is intended to help the reader understand how the conceptual model is incorporated into the creation of physical specimens, and highlight design parameters which are shown to affect system performance in Chapter 3.

2.1 DEVELOPMENT OF PHYSICAL SPECIMENS

Following the proposal of the design concept given in Section 1.4, it was desirable to create prototypes to determine how the concept might be physically implemented. Creating physical specimens allows for various aspects of the design to be refined and provides a means for later validating models of the system, using data collected from experimental testing performed on the specimens. Building and testing specimens in parallel with developing physics based models of the system also allowed for the selection of materials suitable for envisioned purposes where the self-folding laminate concept might be applicable, and afforded a means to design a method for controlling the variation of design parameters in the specimens.

The shape memory alloy (SMA) based self-folding laminate design is realized by embedding an SMA mesh into either side of a pliable elastomeric sheet. To do this, molds are created from ABS plastic such that wire spacing, laminate layer thickness, and the arrangement of wires could be controlled. By utilizing the molds to weave the SMA meshes and subsequently injecting a room-temperature vulcanizing (RTV) silicone elastomer, nominally similar samples can be repeatedly created for testing purposes. Further, changes can be made in one parameter of the mold design in order to create samples whose critical design parameters vary nominally in only one degree of freedom. This allows for testing to examine the effects of varying parameters such as wire diameter, elastomer layer thickness, and wire spacing. A more detailed description of how the specimens are made is provided in Section 2.4 of this chapter.

2.2 MATERIALS

The laminate specimens utilized in testing were made from room temperature vulcanizing (RTV) silicone elastomer and NiTi SMA wire. The material property values used here are the same as those used by the teams at Texas A&M University in previous analysis of the SMA laminate concept [12]. The material properties found by the teams at Texas A&M were measured through characterization experiments, taken from literature, or were given by manufacturer's specifications so that models could utilize properties as similar as possible to the real materials used in experiment. Though several different types of silicon RTV were used during development, one particular blend was chosen for continued use through the remainder of developmental testing, as it

adequately met temperature and adherence requirements for the desired testing conditions chosen for the laminate concept. The silicone RTV chosen for development was Permatex Clear Silicone RTV. The SMA wire chosen for development of the laminate specimens was SAES Getters "Smart Flex" Nitinol wire. Mechanical properties for both of these materials are given in Table 1. The provided Nomenclature includes definitions of the symbols for these properties.

Table 1. SMA laminate specimen material properties [12].

NiTi SMA Material Properties			
$\rho = 6450\ kg/m^3$	$c_p = 320\ J/kgK$	$\nu_A = \nu_M = 0.33$	$\alpha_A = \alpha_M = 4 * 10^{-6}$
$A_f = 362.45\ K$	$A_s = 337.45\ K$	$M_f = 302.15\ K$	$M_s = 332.15\ K$
$C_A = 9.54\ MPa/K$	$C_M = 9\ MPa/K$	$E_A = 48000\ MPa$	$E_M = 42932\ MPa$
$H_{Max} = 0.044$	$H_{Min} = 0.0$	$k_t = 0.24\ MPa^{-1}$	$n_1 = n_2 = n_3 = n_4 = 1$
$k = 10 W/m^2K$			

RTV Silicone Elastomer Material Properties			
$\rho = 3000\ kg/m^3$	$E = 0.6\ MPa$	$\nu = 0.45$	$c_p = 141\ J/kgK$
$k = 0.15\ W/m^2K$			

2.3 LAMINATE SPECIMEN VARIANTS

The specimens utilized in testing were variants of the SMA based laminate specimen shown in Section 1.4. These laminates are similarly comprised of NiTi SMA wire, embedded into a pliable sheet of silicone elastomer. Three variants of the general laminate design are considered, scaling in complexity; choosing to work with different versions of the laminate design allows for the investigation of different aspects of the design.

For the purposes of discussing the laminate design variants, a convention for identifying the parameters of a particular specimen should be established. Three primary variants of the laminate design case are possible using a single fabrication technique, which vary with regards to the SMA mesh complexity. While all three are possible to create using current techniques, initial efforts to validate physics-based models of the system will consider testing of only the most simplified laminate design variant. This will help to minimize potential confounding factors introduced by folding induced in more than a single direction, as is possible with the more complex variants. The general laminate design incorporates a mesh of SMA wires on two sides of the elastomer layer, with each mesh containing wires oriented in two axial directions, which are orthogonal to one another and parallel with the surface of the laminate. Such a laminate will be referred to as being two sided with wires in two directions. The next variant is one step simpler than this, in that it also contains SMA wires on two sides, but for each mesh, SMA wires are stretched in a single axial direction. These will be referred to as being two-sided with wires in one direction. Finally, the variant with the greatest reduction in

complexity contains SMA wire on only one side of the elastomer and all of the SMA wires are oriented in a single axial direction. Figure 8 shows these three main laminate design variants.

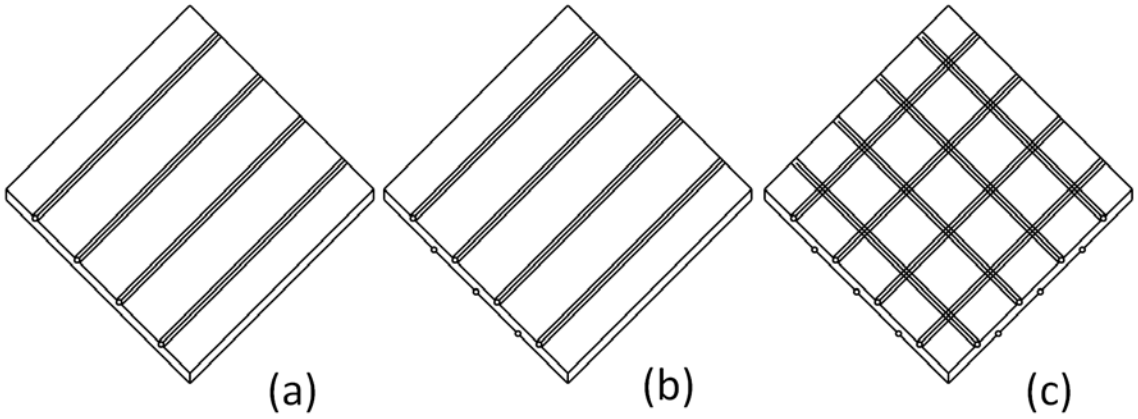

Figure 8. The primary laminate design variants: (a) one-sided, one direction; (b) two-sided, one direction; (c) two-sided, two directions.

For each variation on the laminate design, there are certain parameters whose values influence the behavior of the sheet when the SMA wires are actuated. Specifically, for a given configuration, the thickness of the elastomer layer, the spacing between wires, and the diameter of the SMA wires all impact how tightly the laminate can fold under similar conditions. Figure 9 shows a schematic highlighting these parameters. The diameter of the wire is given by d, the spacing between parallel wires is given by s, the total laminate thickness by t. The thickness of the elastomer, t_{el}, is nominally given by $t_{el} = t - nd$ where n is either 1 or 2, depending on the number of SMA meshes in the laminate variation.

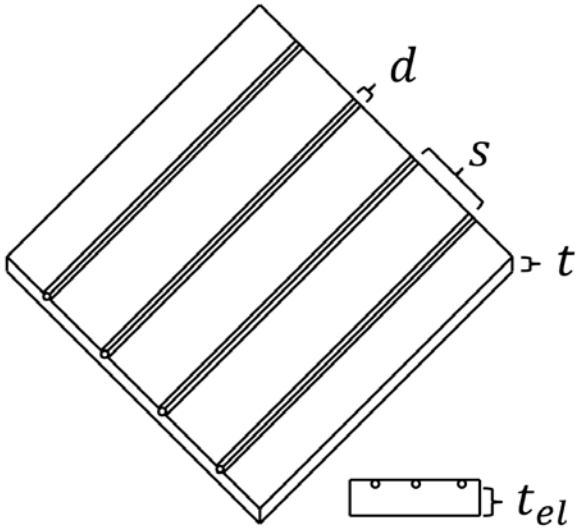

Figure 9. Schematic of SMA laminate specimen.

2.4 FABRICATION PROCESS

In order to control the quality and consistency of the laminate specimens, custom molds were created for use during the fabrication process. Each mold contains grooved notches on which the SMA wires can be woven into a mesh. These notches serve to maintain alignment and spacing of the wires to ensure that the meshes remain in the correct position and to ensure that wires on opposing sides of the laminate are offset by one half the wire spacing to provide the optimal thermal isolation for the SMA from heating on the opposite laminate face. The molds can also be customized to set the desired elastomer layer thickness for each new specimen; as this parameter is set by the mold, it allows for a consistent separation of opposing SMA meshes across the entire laminate, improving the quality and consistency of the samples and the uniformity of the system's performance. While molds can be re-used to create dimensionally similar

specimens, new molds are required for desired changes in elastomer layer thickness or wire spacing.

Molds utilized in the fabrication of the laminate specimens are designed in Solidworks, a standard computer aided drafting (CAD) software. These files are then realized via 3D printing of the mold out of ABS plastic using the fused deposition modeling (FDM) technique. Producing the molds this way allows for dimensionality control suitable for prototype development and facilitates rapid specimen production. Further, the molds are designed in such a way that the CAD files can quickly be changed and re-printed to accommodate changes in desired design parameter values. A portion of a representative mold used in the production of the laminate specimens is shown in Figure 10, with SMA wires stretched in the same axial direction.

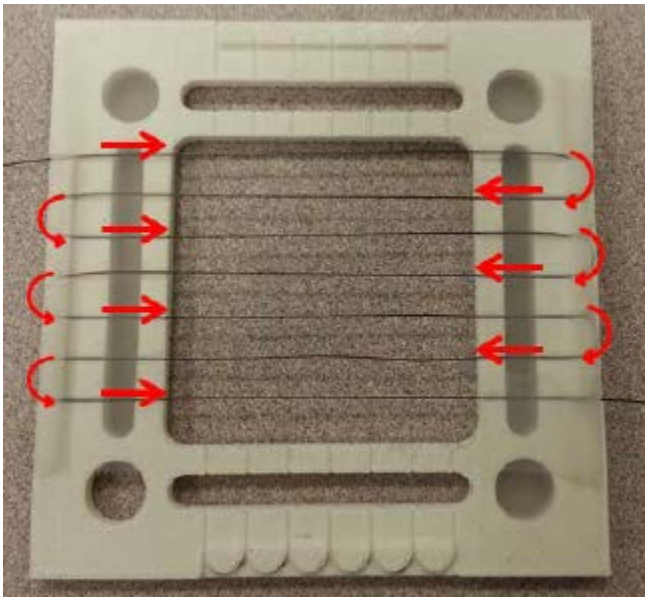

Figure 10. Mid-portion of a representative mold, used in laminate specimen production, showing SMA routing to achieve common axial orientation.

Each mold's dimensions have a direct impact on the dimensions of the finished laminate specimen. Accordingly, each mold is used to create a laminate specimen with design parameter values corresponding to that particular mold. Once the mold is fabricated, SMA wire can be woven through the notches on the desired sides of the mold, leaving a cavity for the elastomer layer. After the SMA meshes have been woven, liquid silicone RTV is injected into the cavity in the mold, and the mold is sealed and set aside for 24 hours at room temperature to allow the RTV to cure into a solid elastomeric layer containing the SMA meshes. Once cured, the finished specimen can be removed from the mold and used for experimental testing.

As Figure 10 shows, SMA wires can be strung around the posts and through the notches on the mold piece to form a linear array of aligned wire segments. By offsetting the alignment of notches on the top and bottom sides of the mold, SMA wire can be strung in such a way as to create the half period offset intervals characteristic of the laminate variations shown in Section 2.3. To create the woven pattern of orthogonally oriented wire segments on a single side of the laminate, such as in variant c, wires are first strung in a single direction to create a lattice, then another length of wire is woven through the notches on the adjacent side of the mold. Wires are woven such that horizontally and vertically aligned wire segments are as close as possible to laying in a common plane.

Once the wires are woven through the notches of the mold piece as desired, the silicone RTV can be injected. Flat lids are attached to cover the top and bottom of the mold such that, upon injection, the RTV fills the inner cavity. The mold is then sealed,

and the RTV is allowed to cure for 24-48 hours at room temperature. To prevent voids from forming in the finished specimen, excess liquid elastomer is injected before sealing the mold, to ensure that the entire cavity is filled with the liquid RTV elastomer. The mold lid pieces are designed such that excess liquid elastomer is squeezed out via a sprue, allowing the flashing to be trimmed off once cured. Once the RTV has fully cured, the lid pieces are removed, and the specimen is cut loose from mold. After any remaining flashing has been trimmed away, the specimen can be speckled and used in testing. Chapter 3 will discuss methods used in experimentally testing the laminate samples and the results of testing selected laminate variants.

3. EXPERIMENTAL DESIGN & RESULTS

This chapter is intended to provide details regarding how the physical SMA laminate specimens are tested, characterized, and analyzed. Non-invasive imaging techniques are discussed for capturing surface deformations in three dimensions, testing procedures for actuating the SMA laminate specimens are presented, and the results of testing various different samples are presented to examine the effect of changing design parameters. The methods presented in this chapter are presented as a useful way to capture deforming surfaces in three dimensions in such a way as to allow for comparison of surface deformations amongst multiple experimental trials and for comparison of measured data to simulation data.

3.1 DIGITAL IMAGE CORRELATION

To achieve the highest degree of accuracy, the method of measurement used should interfere as little as possible with the deforming system. For the self-folding laminate, the surface curvature profile resulting from actuation of the SMA wires may be influenced by a number of factors, including but not limited to: wire spacing, elastomer layer thickness, temperature, and the number of wires present. As with any real system, there exists some aleatory uncertainty. While some uncertainty may be reduced by tighter control or measurement of variables, there will always be some remaining irreducible uncertainty. In an effort to minimize additional factors contributing to this total uncertainty, a visual measurement method was desired to allow for the surface

topography to be measured during deformation without physically interacting with the laminate specimen.

Various techniques have been developed to capture information about three-dimensional surfaces by optical means, including fringe projection and photogrammetry techniques. Fringe projection techniques, which have been used in biomedical applications and some industrial applications, rely upon the projection of a structured pattern onto the object surface. The modulation of the pattern over the surface is then recorded and an algorithm is applied to determine the mapping of the distorted pattern to 3D coordinates to represent the object [30]. Fringe projection techniques however are best suited for certain situations; common problems arise from the presence of shadows, and the lack of effective methods of removing the carrier-phase component of the measured phase. Additionally, non-sinusoidal waveforms in the recorded pattern are known to cause significant phase measurement error.

Photogrammetry techniques rely upon images taken at a variety of angles, usually taken by a single camera, and an algorithm for correlating the images to determine an object's shape in three dimensions. With a single camera, these techniques are best suited to capturing deformation of objects at rest. It has frequently been used to monitor geographical features [31, 32] but has also been widely used to capture objects on a variety of scales and in environments that may prove challenging for other techniques [33]. Stereophotogrammetry overcomes some of the challenges of single camera photogrammetry by using more than one camera to resolve the object scale.

Digital Image Correlation (DIC) is a visual measurement technique extending stereophotogrammetric methods. One or more cameras are used to take images of the deforming specimen at fixed intervals. DIC has become increasingly important and useful in recent years, as it represents a fast and highly accurate tool for deformation and shape analysis [34]. It is also starting to be considered for work with smart materials, including the validation of SMA constitutive models [35] and in fatigue induced deformation measurement in NiTi SMAs [36]. DIC requires a speckle pattern to be applied to the surface of specimens to be captured. The underlying principle of the method is that these speckles are assigned to subsets – as the specimen deforms, the subsets are tracked and from this a displacement vector may be calculated from the change in the location of a subset between the reference and deformed image. Figure 11 illustrates this process.

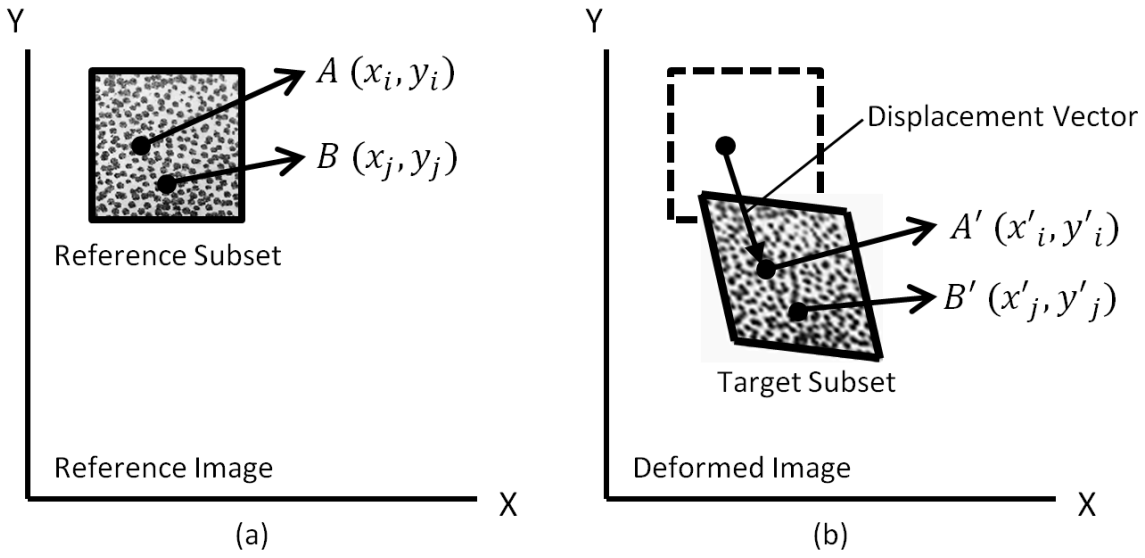

Figure 11. Visualization of subset tracking technique utilized by the Digital Image Correlation method.

These images are later analyzed to extract data about the occurring deformations. This allows for users to take measurements non-invasively so as to avoid introducing systematic error to the measured performance. 3D DIC uses two or more stereoscopic cameras to account for deformations along three mutually orthogonal axes. This overcomes many of the limitations of 2D DIC which requires that deformations occur in a plane perpendicular to the line of sight of the camera for high fidelity. One such limitation stems from the fact that 2D DIC measurements use only a single camera to capture images of the deforming specimen. This can be problematic in certain situations - a 200% isotropic deformation of an object will appear to be identical to the object which simply translates to one half its original distance to the camera without deforming. This phenomenon, which is illustrated in Figure 12, requires that for appropriate use of 2D DIC, the object remain a constant distance from the camera during image capture, and implies that deformation should only occur in a plane perpendicular to the viewing direction of the camera in order to accurately be measured.

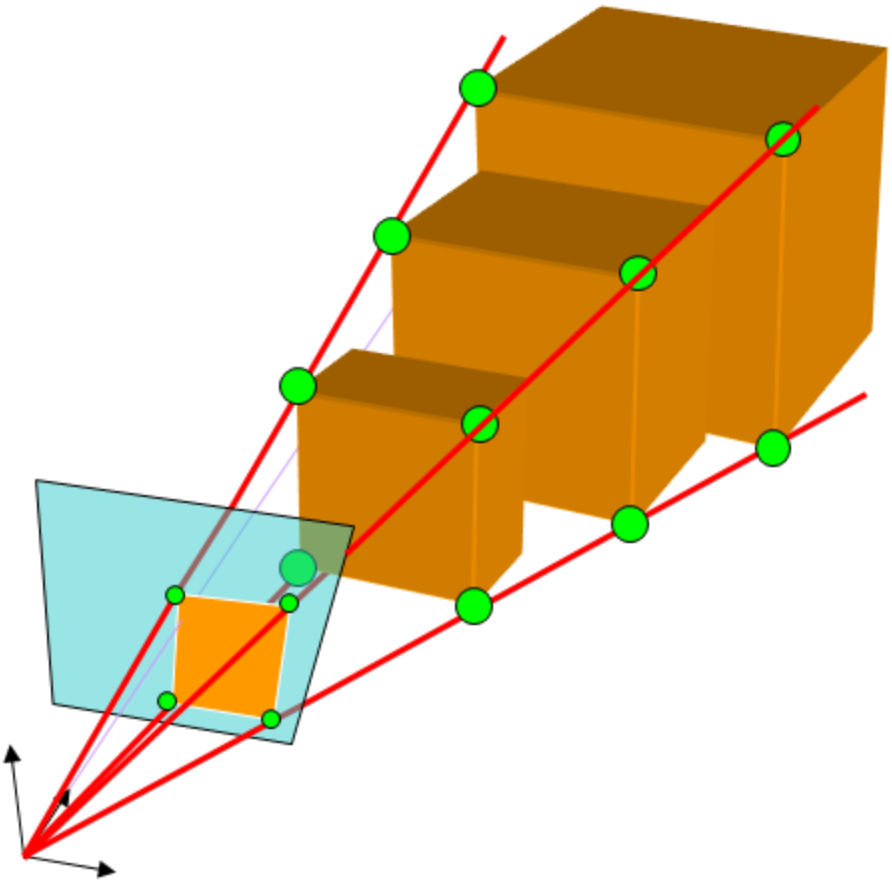

Figure 12. Cyclopean vision limitations associated with 2D DIC [37].

3D DIC relies not upon a single camera, but on two or more cameras. This provides a way to capture the scale of the object without restricting measurements to a fixed distance or to capturing only in-plane deformations. Figure 13 illustrates how 3D DIC provides object scale resolution.

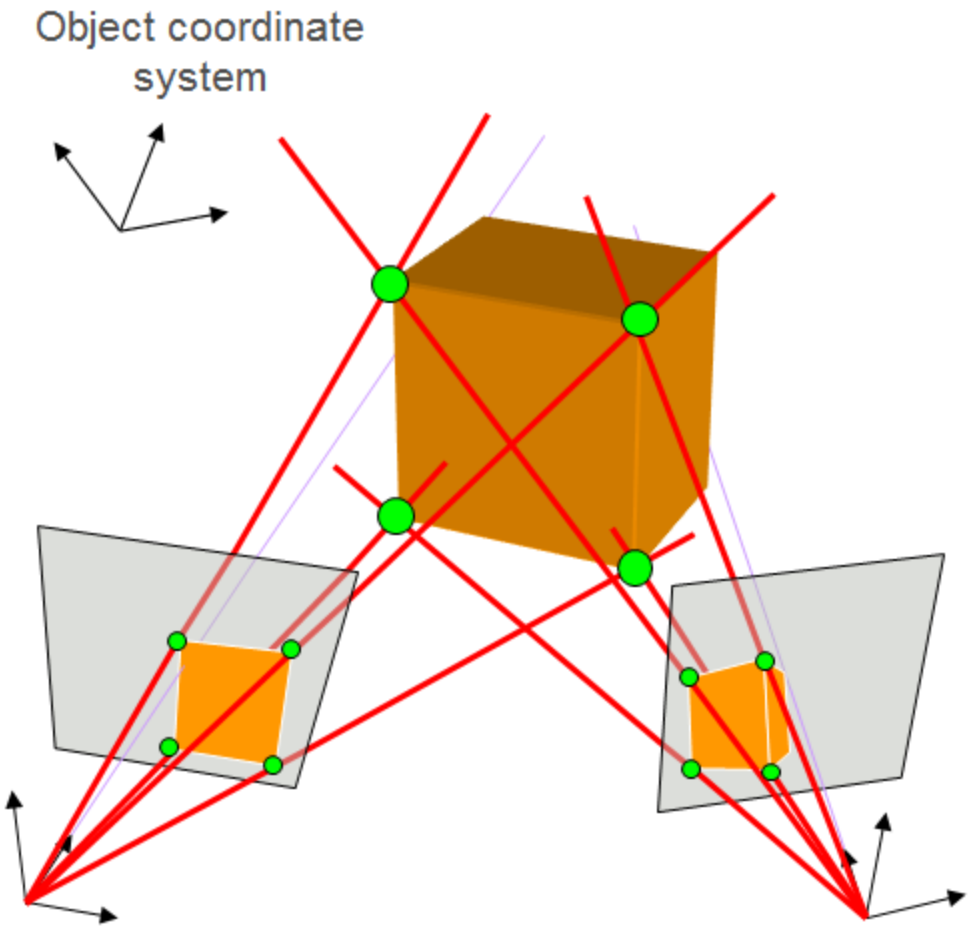

Figure 13. Scale resolution of objects by 3D DIC method [37].

With two or more points of view of the specimen at each point in time and a calibrated stereoscopic camera rig, it is possible to calculate where in space a point on the specimen lies, based on its position in the images from each camera. This fundamental advantage over other visual methods, such as 2D DIC, allows for capturing complicated out of plane deformations in 3D space quickly and accurately with

commercially available 3D DIC software and hardware. For this reason, 3D DIC was chosen for measuring dynamic surface topography changes.

The capability of 3D DIC to capture surface deformations along 3 independent axes also provides for an effective way to examine the effects of how defects or variations in the tested specimens cause behavior that would not be expected in a theoretical model. For example, for the reduced complexity case, one would expect deformations in only a single plane. For a specimen oriented with its length in the y direction, width in the x direction, and thickness in the z direction, folding behavior in a reduced complexity specimen should occur only in the y-z plane, given consistent offset of SMA wires from the neutral axis of the laminate. However, defects or stochastic variation among nominally similar samples may yield small differences which create out of plane twist when heated. While effects such as these may not show up in idealized physics-based model of the system, they may manifest during testing. It is therefore important when validating models to consider a method for measuring these out of plane effects.

3.2 EXPERIMENTAL SETUP

To effectively compare physics-based models to experimental results for the case of the SMA-based laminate structure, a tool must be developed to measure the physical deformation of the specimen in 3D space and compare that data to 3D deformations of the system as predicted by physics-based models of the nominally similar system. This

tool should be able to overlay the real and modeled system data, and provide a visual and quantitative measurement of the difference in performance.

To this end, the experimental method used must measure and assess system performance using 3D DIC to capture surface topography as the laminate is heated to a temperature above the austenitic transformation temperature of the SMA wire. For the SMA laminate system, the radius of curvature averaged over the surface provides a meaningful measure of performance, as it indicates the tightness of folding in the actuated system. For a larger or more complex laminate variation where multiple folds might be desired, the radius of curvature would serve as a measure of performance of a single folding action. The MHD, as a measure of shape matching, could be used both for simplified and complex laminate variations to compare multiple surfaces.

A custom enclosure was constructed in order to test the reduced complexity samples. The enclosure consists primarily of four insulated walls, a glass lid, and a semi-transparent platform. The enclosure is further equipped with lighting, circulating fans, a heating element, and a thermocouple probe. A schematic of the enclosure and its orientation relative to the stereoscopic 3D DIC cameras is shown in Figure 14.

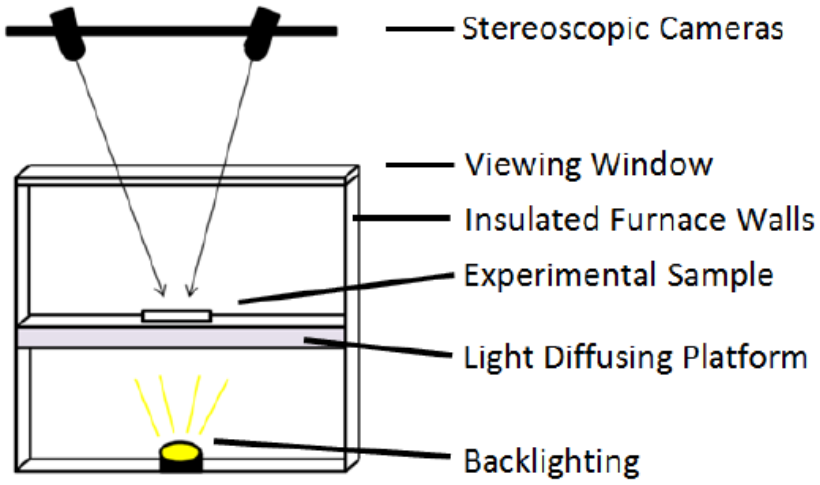

Figure 14. Custom enclosure for testing reduced complexity laminate specimens.

The enclosure allows the specimen to be heated more uniformly from room temperature (roughly 22°C) to temperatures in excess of 120°C. This allows for specimens to be heated through the temperature range required to fully transform the SMA wire in the samples, inducing a fully actuated response in the laminate. During this process, the stereoscopic cameras capture images of the specimen at a specified frequency of 1 Hz.

While the circulating fan does help to reduce thermal gradients within the enclosure, small temperature gradients may still exist. To investigate the magnitude of the thermal gradient over the platform, a grid was marked out over the center of the platform covering measuring approximately 75 mm wide and 75 mm long. The grid was divided into nine evenly sized squares such that each square measured approximately 25 mm by 25 mm. Two calibrated thermocouples were used to investigate the temperature

across this gridded space. One thermocouple was fixed in the center square and was used as a reference for comparison. The second thermocouple was fixed in one of the nine squares and was used to measure the local temperature of that square. Five measurements were taken by heating the enclosure from 40°C to 80°C and measuring the local grid temperature, using the reference temperature of the thermocouple in the middle of the grid to compare temperatures taken at different locations. The measured thermal gradient across the test grid was found and is shown below in Table 2.

Table 2. Measured thermal gradient in testing enclosure

Top Left Position: 80.0°C		Top Right Position: 82.2°C
	Center Position: 82.7°C	
Bottom Left Position: 76.1°C		Bottom Right Position: 76.3°C

To use DIC techniques to measure deformations, specimens must have a speckle pattern applied to the surface of interest. This speckle pattern is important as it affects how well the DIC algorithm will be able to distinguish between subsets of the surface as the surface deforms. As such, the speckle pattern should have certain characteristics: it should be distributed over the area of interest with a uniform density per subset, be randomly distributed, and have dark regions of various sizes. For the highest degree of accuracy, the goal is to create a speckle pattern for which each subset is unique and easily identifiable; this requires that the speckle pattern also be non-repetitive, isotropic, and have high contrast [37]. Further, it is important to consider how the speckle pattern

is applied, as the speckles must be able to deform with the sample and remain intact under testing conditions. The testing conditions for each specimen should be carefully considered before choosing how to apply the speckle pattern. For example, paint may be an appropriate medium for speckling a surface in certain situations, but it may be inappropriate for others; for the SMA laminate system, paint applied to the elastomeric surface is prone to cracking and stretching as the specimen deforms under heating. For the SMA specimens used in this work, dark points were applied to the surface using a fine point permanent marker. As techniques for performing 3D DIC analysis have been developed over several years, resources exist to assist with this. Figure 15 shows a representative speckle pattern suitable for testing the laminate specimens.

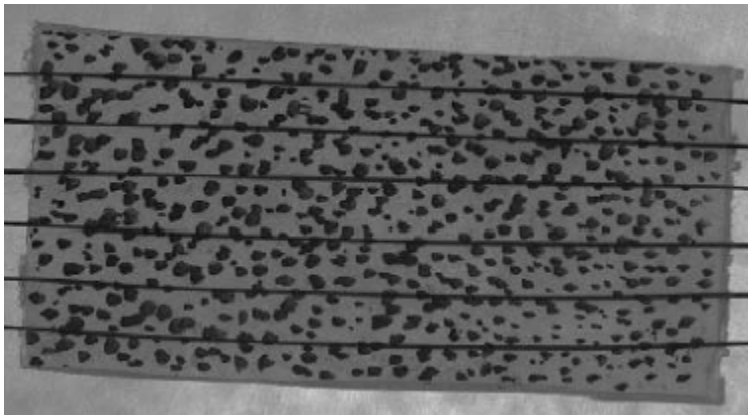

Figure 15. Representative speckle pattern applied to a laminate specimen.

Once the laminate specimens have been speckled and are ready for testing, they are placed in the testing enclosure, which begins at room temperature. The clear lid is fixed in place and a circulating fan is switched on; these measures help to keep the

enclosure as near as possible to a uniform temperature and minimize any thermal gradients near the specimens during testing. With the samples in view of both DIC cameras, the enclosure is gradually heated from room temperature to approximately 100°C. During this span of time, the stereoscopic DIC cameras record the deforming specimen. A specimen is considered to be fully actuated when it exhibits a steady state response after continuing to heat the sample above A_f. As the exhibited curvature is non-monotonic during heating, a decrease in curvature is observable with continued heating above this point towards a steady state response. After full actuation is observed in the sample, the heating element is switched off and the enclosure is brought back down to room temperature. Due to the hysteretic nature of SMAs, it is important to compare data for heating and cooling separately. In this work, only the response of the laminate during heating is considered.

After conducting the test, the images are processed by the DIC software. For this study, the programs “Vic Snap” and “Vic 3D” were used for image correlation. After processing the images, the principle curvature is calculated across the whole specimen surface. The tightest achievable folding of the laminate occurs where the principle curvature is maximized; at the point where this is measured, nodal data is extracted for later comparison. Extraction of this data is useful for comparing the measured performance against other experimental trial data and against simulated predictions for the achievable performance of the laminate variant. By using the point of maximum curvature for the point of comparison and nodal data extraction, the MHD between experimental and model data surfaces can be calculated to compare the laminate system

surfaces at a similar state. As the laminate system is still currently under development by teams at Texas A&M, there is interest in determining the capabilities of the laminate system; choosing the point of tightest folding also highlights the achievable performance for a certain laminate variation under specified conditions. Simulation of laminate behavior and methods for comparing experimental data for simulation predictions will be discussed in later chapters.

Before testing any of the laminate specimens, it was important to verify DIC measurement accuracy (i.e. that the DIC is able to measure a known radius of curvature to within an acceptable tolerance). To do this, four constant radius speckled plastic pieces were measured. The known curvature values of the verification pieces and the measured curvature values are shown in Table 3.

Table 3. DIC verification results.

	Object 1	Object 2	Object 3	Object 4
Known curvature (1/mm)	0.0287	0.0248	0.0229	0.0210
DIC measured curvature (1/mm)	0.0276	0.0240	0.0242	0.0203
Relative Percent Error	3.7%	3.2%	5.7%	3.1%

One of the primary goals of analyzing and modeling the SMA laminate system is to characterize the capability of the system to achieve folding. To this extent, the metric chosen to measure the folding performance of an actuated section of the SMA laminate is the average radius of curvature; folding behavior in non-zero thickness materials will not have a perfectly sharp crease but will instead bend with some curvature. The radius

of curvature serves as a measure of the tightness of achievable folding – smaller achievable radius of curvature values indicate tighter achievable folding, while larger values indicate less sharp folding behavior.

While the radius of curvature measurement is useful for characterizing a single fold, larger and more complex implementations of the laminate design could be capable of exhibiting multiple folds, compound folding, or folding in more than a single direction. Sample size for the reduced complexity specimens presented in this work was chosen such that the folding behavior of the entire surface could be thought of as a single fold. As such, radius of curvature measurements for the samples presented will consider the entire area of the surface interior to the fold. For larger or more complex laminate variations, radius of curvature measurements should be taken only over an area representative of a single folding action. To establish the groundwork for later analysis of the laminate and to provide a more complete analysis of folding behavior beyond that of a single folding action, a metric for shape matching will be used. Establishing such a metric provides a way to analyze non-uniform folding behavior and is useful for comparisons between multiple surfaces. The mean Hausdorff distance measurement, discussed in Chapter 5, was chosen as the basis for a measure of shape matching in laminate samples.

3.3 EXPERIMENTAL RESULTS

Before considering the effect of varying parameters on system performance, it is useful to establish a reference for the amount of stochastic variance which is introduced

due to the fabrication process. To investigate this, three samples were built to share the same nominal dimensions as closely as possible using the fabrication techniques discussed in Chapter 2. The actual measured dimensions of the finished sample variants are given in Table 4.

Table 4. Stochastic variation sample variant dimensions.

	Variant 1	Variant 2	Variant 3
Total Laminate Thickness (mm)	2.02 ± .05	1.88 ± .04	2.00 ± .09
Wire Spacing (mm)	6.30 ± .32	6.46 ± .05	6.43 ± .06
Width (mm)	12.91 ± .14	13.67 ± .08	13.19 ± .07
Length (mm)	49.27 ± .11	49.31 ± .09	49.27 ± .11

All three specimens were speckled with a different identifying color, as seen in Figure 16, and were tested simultaneously to ensure each specimen underwent similar testing conditions as nearly as possible. Specimens were heated from room temperature until full actuation was observed in all specimens, which occurred around 90°C. Figure 17 shows how the principle curvature of each sample changed during heating.

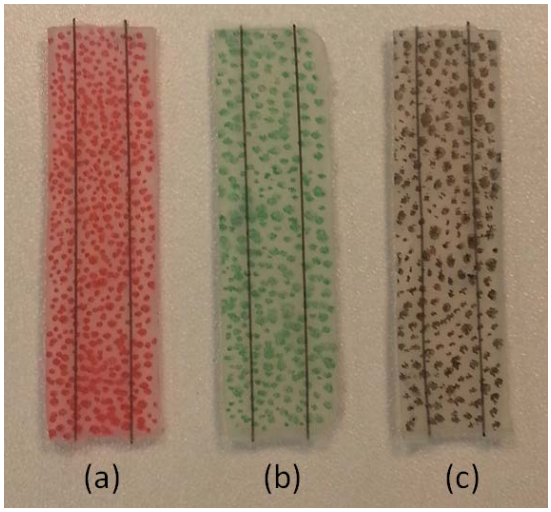

Figure 16. Stochastic variance testing specimens: (a) variant 1, (b) variant 2, and (c) variant 3.

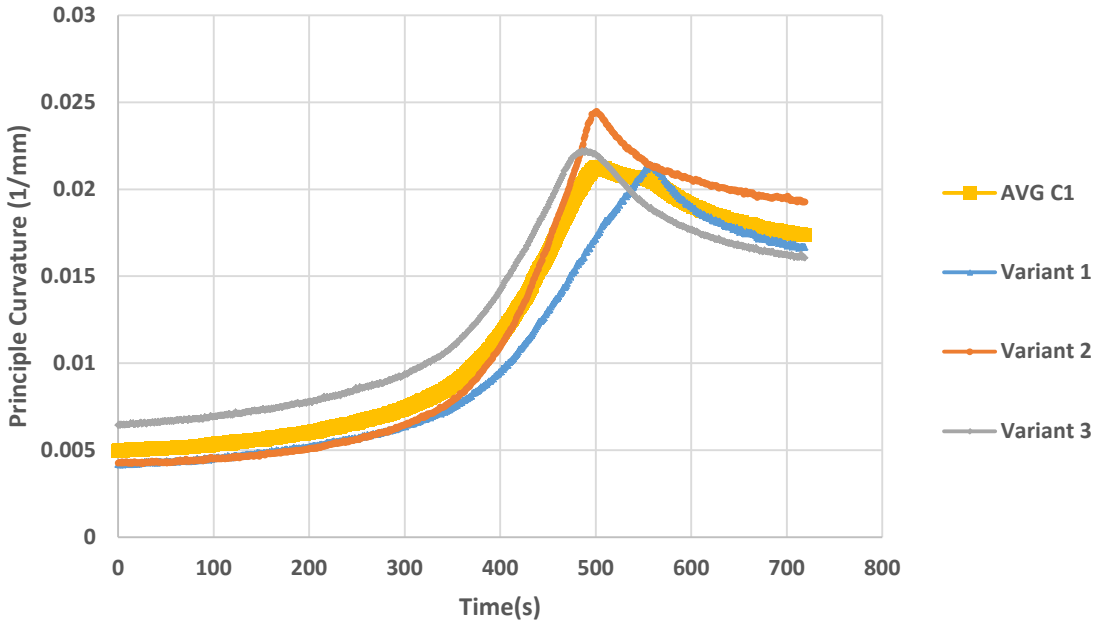

Figure 17. Principle curvature measured as the sample variants undergo simultaneous heating.

Though the curvature of the variants differs both in tightest achievable folding curvature and the time/temperature state at which this occurs, the achievable radius of curvature difference is small. Differences in performance may be attributed to the small differences in sample dimensions, and small temperature gradients which may exist in the testing enclosure.

After testing the three nominal variants, the nodal data was extracted and analyzed using the techniques presented in Chapter 5. Radius of curvature measurements and the standard deviation of mean Hausdorff distance (MHD) to a common reference were computed to provide a sense of variation among these nominally similar variants. Table 5 shows these results.

Table 5. Stochastic variation results.

	Variant 1	Variant 2	Variant 3
Radius of Curvature (mm)	46.7	40.9	45.0
Avg R | R Std Dev.	44.2 mm | 3.0 mm		
MHD Std Dev.	0.075 mm		

For these three variants, the radius of curvature measurement was taken as an average over the entire surface, and the mean Hausdorff distance was taken to a common referenced flat surface. Computation of the MHD is discussed further in Chapter 5. For the purposes of examining the SMA laminate concept and demonstrating the validation framework, these results sufficiently illustrate that SMA laminate specimens which are

physically distinct, but nominally similar, and are produced via the methods described in Chapter 2 should yield similar results under similar conditions.

In addition to investigating stochastic variation of similar samples, it is useful to consider samples which are distinctly different. Changing the values of the laminate thickness and the wire spacing have a significant impact on the achievable folding curvature. In order to investigate this effect, three separate reduced complexity samples with the following properties were tested. Actual dimensions of the finished physical samples were measured using digital calipers:

Table 6. Reduced complexity laminate specimen parameter values.

	Sample 1	Sample 2	Sample 3
Total Laminate Thickness (mm)	3.00 ± .02	1.18 ± .04	1.25 ± .02
Wire Spacing (mm)	6.51 ± .10	6.88 ± .50	3.60 ± .39
Width (mm)	27.41 ± .44	28.66 ± .17	13.50 ± .19
Length (mm)	49.18 ± .12	49.34 ± .27	49.61 ± .27

As shown in Table 6, samples 2 and 3 share similar elastomer thicknesses, while samples 1 and 2 share similar wire spacing. Choosing these parameters allows us to independently investigate the effect of changing either the thickness or wire spacing. Each sample was heated from room temperature to about 100 °C, or until full actuation was observed. Surface deformation for each sample was captured using 3D DIC and each test was conducted five times to account for stochastic variance in each of the three

samples. Table 7 illustrates the resulting change in the surface averaged tightest achievable radius of curvature caused by changing thickness and spacing parameter values.

Table 7. Tightest achieved surface averaged radius of curvature for five experimental trials per sample.

	Sample 1	Sample 2	Sample 3
Radius of Curvature Trial 1 (mm)	94.4	68.1	64.2
Radius of Curvature Trial 2 (mm)	98.3	61.6	65.8
Radius of Curvature Trial 3 (mm)	100.9	70.8	66.7
Radius of Curvature Trial 4 (mm)	99.6	71.4	64.2
Radius of Curvature Trial 5 (mm)	96.9	66.7	67.3
5 Trial Average (mm)	98.0	67.7	65.6
Standard Deviation (mm)	2.5	3.9	1.4

For each of the experimental samples, local surface curvature was calculated by post-processing the data. It is interesting to note that the folding of the sheet is non-monotonic; as the laminate sheet undergoes heating, the sheet exhibits folding behavior until a maximum curvature is reached, then the fold flattens back to some extent as it moves towards a lesser steady state curvature. The difference between the maximum achievable curvature value and the steady state curvature is dependent upon the chosen design parameters of the laminate. Specifically, the thickness of the elastomer layer

plays a large role in determining this difference. By plotting the average surface curvature while heating the laminate specimens during the experimental trials, we can observe this trend. Figure 18 shows the non-monotonicity of the laminate folding behavior for a single trial run of the one-sided, one-directional laminate specimens under heating from room temperature to full actuation.

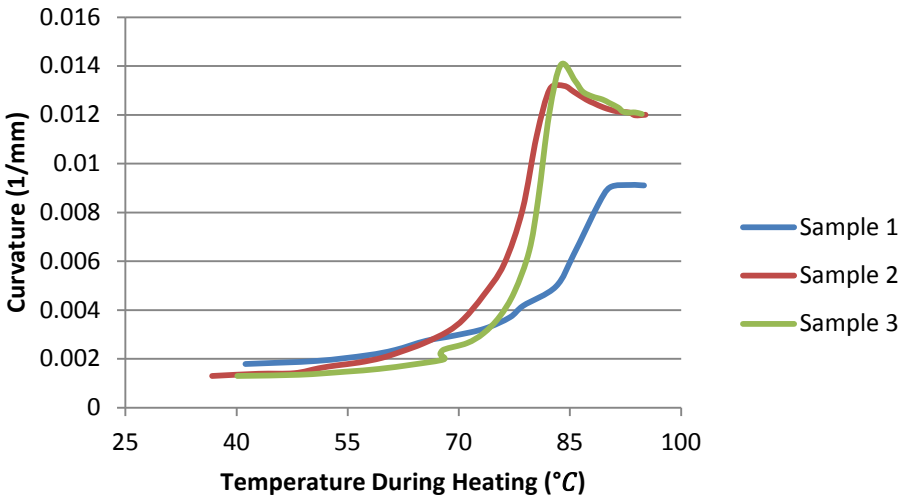

Figure 18. Non-monotonic curvature trend for experimentally measured laminate specimens under heating.

As the results indicate, samples 2 and 3, which have a thinner total laminate thickness, exhibit a higher maximum curvature than sample 1. This effect is reasonable to expect; for samples with a thinner total laminate thickness, the SMA wires lay closer to the neutral plane of the system. For a given amount of strain induced in the SMA wires during heating, strain induced in the wires closer to the neutral plane of the

laminate system will cause a larger bending moment in the laminate, causing tighter folding and a higher curvature.

Also for samples 2 and 3, the degree of non-monotonicity is greater than for sample 1. For these samples, the amount of SMA relative to the amount of elastomer is greater; so it is reasonable to expect that the non-monotonic behavior caused by aniostropic transformation of the SMA between A_S and A_F during heating would be more pronounced in samples 2 and 3, than in sample 1, where there is a greater amount of elastomer material to resist the motion caused by the anisotropic transformation induced strain.

As Figure 18 shows, trials indicate that for samples 2 and 3, while there is a difference in the tightest achievable curvature and steady state curvature, the curvature profiles during heating are fairly similar; the difference between these profiles is on the same order of magnitude as seen between the nominally similar specimens. This suggests that changing the wire spacing does not have as profound an effect on the tightest achievable curvature as changing the total laminate thickness. This same trend is suggested by observations from plotting the tightest achieved radius of curvature for each experimental trial for each of the three samples, as is shown in Figure 19.

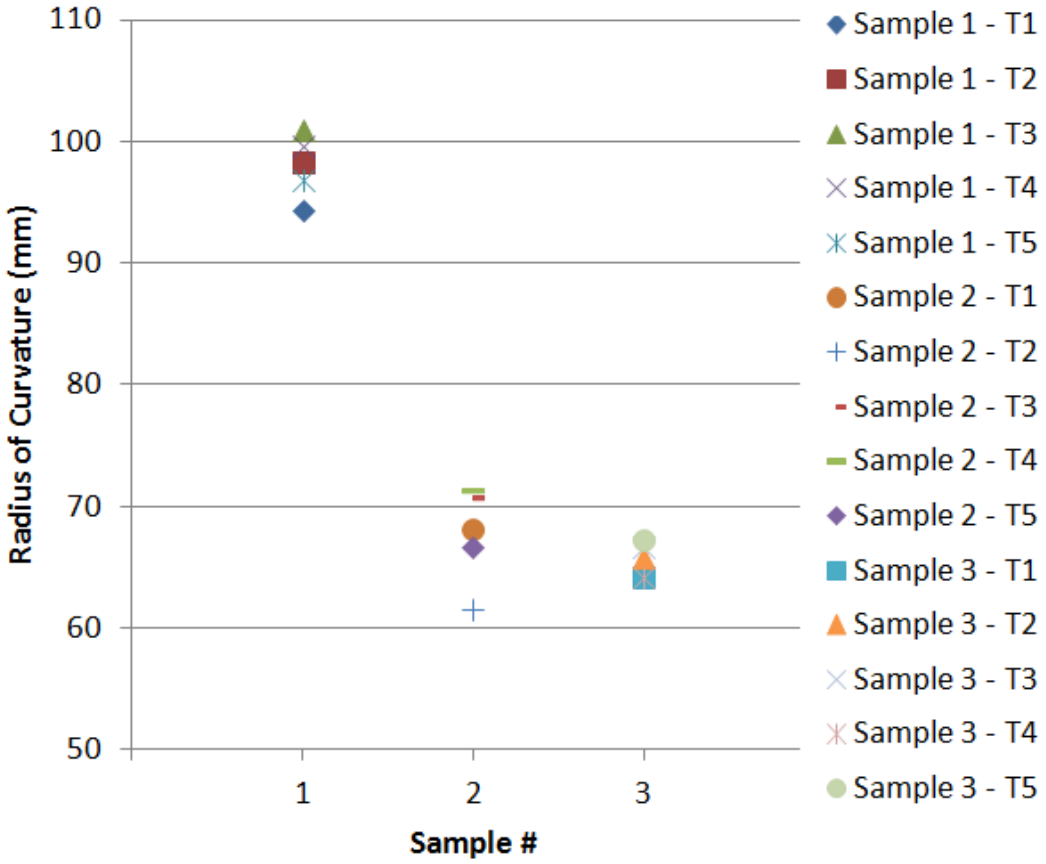

Figure 19. Tightest achieved radius of curvature for each experimental trial, for each sample case.

4. PHYSICS-BASED MODELS & RESULTS

This chapter is intended to provide an account of the development of high fidelity models to simulate the SMA laminate concept, using the material properties presented in Chapter 2 and the boundary conditions matched by experimental testing as presented in Chapter 3. This chapter discusses application of both FEA techniques and an analytical model using classical laminate plate theory to predict the resulting curvature of the same SMA laminate variants which were experimentally tested. Consideration of these techniques are paired with an investigation of two different modeling assumption cases to develop six different modeling approaches to simulate the system. By taking this approach, it is possible to investigate the impact of using these different techniques and assumptions on the resulting level of agreement between simulation data and measured data. The results of applying these six modeling approaches to the three experimentally measured parameterized samples are also presented.

4.1 FINITE ELEMENT MODELING

With most complex systems, it is desirable to develop models or simulations by which system behavior may be reliably predicted. This is especially true for systems which are either time-consuming or resource expensive to build or test. In the case of active material systems such as the SMA laminate concept, prototype samples can be or have been developed and experimentally tested. However, it is desirable to develop high

fidelity models such that different or more complex implementations of the system may be simulated with reliable fidelity to a real implementation of the modeled system. As with modeling any real system, one should always be conscientious of the limitations of a model. No model is perfect – the physically implemented counterpart to a modeled system will always include some unaccountable variation which may impact the performance of the system. As such, a model should be able to provide the user information about the performance of the system with fidelity sufficient for the intended purpose of the model's output. However, there is almost always a tradeoff between accuracy and resource cost; it is up to the designer to understand and choose an acceptable tradeoff between resource cost and model fidelity.

Further, if one truly wants to understand the value of making certain modeling assumptions, it is useful to compare the results of modeling the same system under changing assumptions. In the course of developing a physics-based model of the SMA laminate concept, several different modeling assumptions and idealizations were varied. The assumptions investigated include the consideration of gravity, modeling the wire geometry as round or square, and the choice of using a FEA simulation or a model which considers the implications of classical laminate plate theory. These different modeling assumption cases are discussed further in Section 4.3.

For the purposes of adapting the methodologies to the case study of the SMA-based laminate structure, the system was modeled using Abaqus 6.12, a FEA solver, in conjunction with a user-defined material subroutine (UMAT) to appropriately handle to the transformation of the shape memory alloy material. The UMAT is based upon a

proposed constitutive model [38, 39] and was also used in previous works to model SMA behavior in laminate systems [9, 10]. This approach has also been used to apply constitutive models of SMA behavior to model to other types of systems [40], including active panel structure actuation [41] and an active joint rigidity system [42].

To control the consistency between model iterations and more easily allow for the verification of model implementations, FEA models were created using Python scripting. This allowed the proper commands to be sent to Abaqus to construct the laminate model and incorporate material properties and the Fortran implementation of the SMA UMAT. A similar process has been used to model SMA behavior in other active material systems [40, 43] as well as in prior efforts related to the laminate system primarily considered here [8-11]. In each model, the laminate was partitioned around the SMA region to ensure that meshes over the model were implemented smoothly and uniformly. Additionally, an analytical rigid surface is included in the model assembly to represent the platform on which the specimens rest during testing. While many of the figures illustrating the laminate model do not show this rigid surface, it is included in all of the FEA model implementations. Figure 20 shows a representative image of the deformed laminate in relation to this rigid surface.

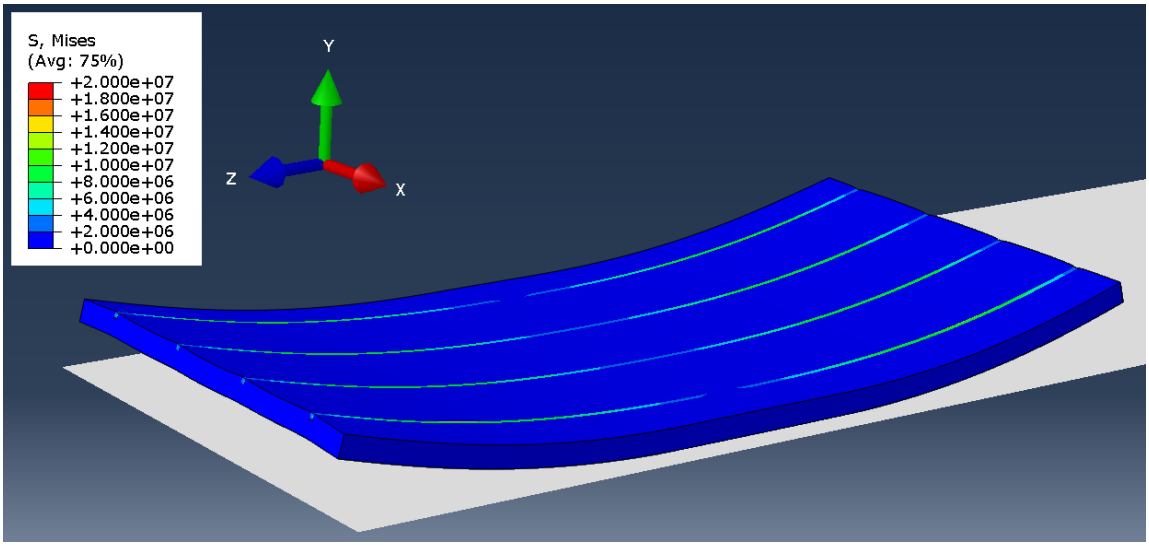

Figure 20. Representative illustration of laminate simulation. Rigid "floor" surface is shown here in white.

Three dimensional deformable elements with quadratic shape functions were selected for use in meshing the laminate model, both in SMA and elastomer regions. Second-order hexahedral (C3D20) elements were primarily used, except around the SMA wire regions when modeled as having a round cross section. In these regions second-order wedge elements (C3D15) were used as they improved the uniformity of the mesh. Meshing parameters were chosen such that the size and number of elements were sufficient to capture the deformation of the laminate. This will be demonstrated in a mesh convergence study to follow. No temperature-displacement elements were required in these meshes; the experimental testing of the laminate specimens considered the thermal response to be spatially uniform and temporally quasi-static.

Figure 21 shows the laminate models partitioned for both square and round wire approximations prior to meshing. Figure 22 and Figure 23 show representative meshes for the two different wire geometry approximations, the former showing a square wire approximation and the latter showing the SMA wires modeled as round.

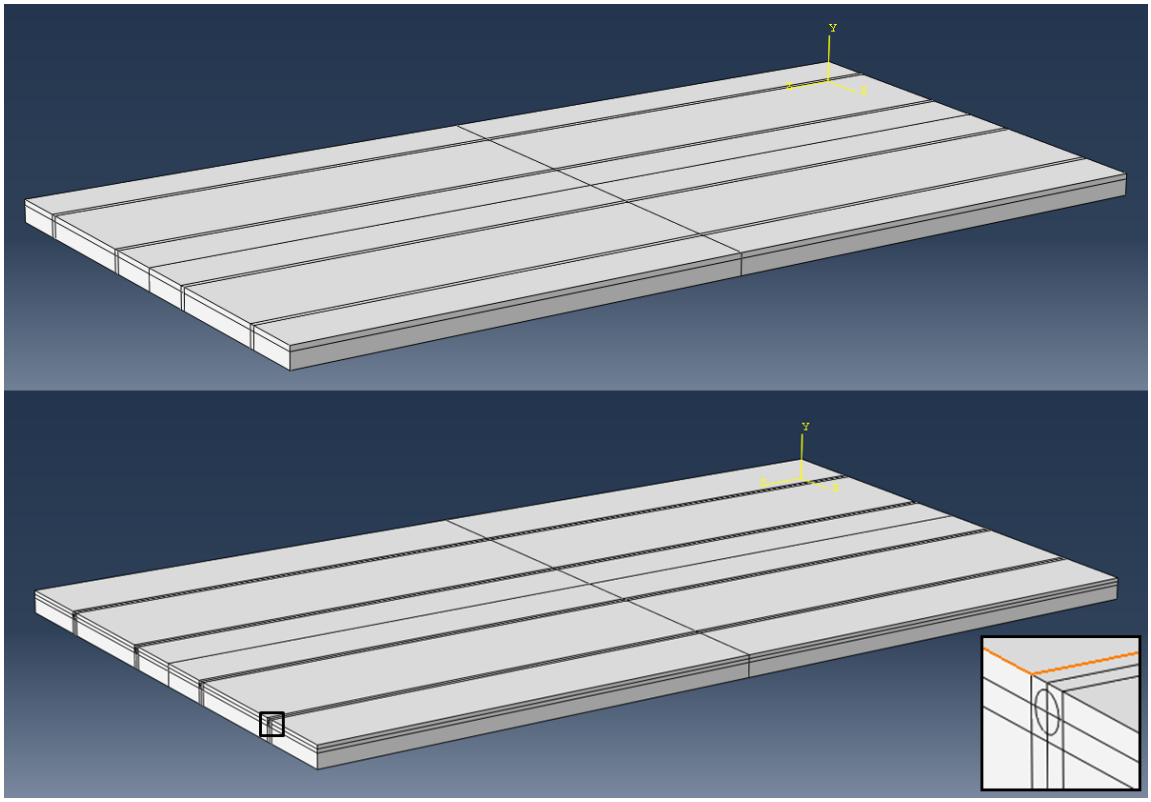

Figure 21. SMA laminate model prior to meshing. Shown are both square wire (top) and round wire (bottom) geometry approximations.

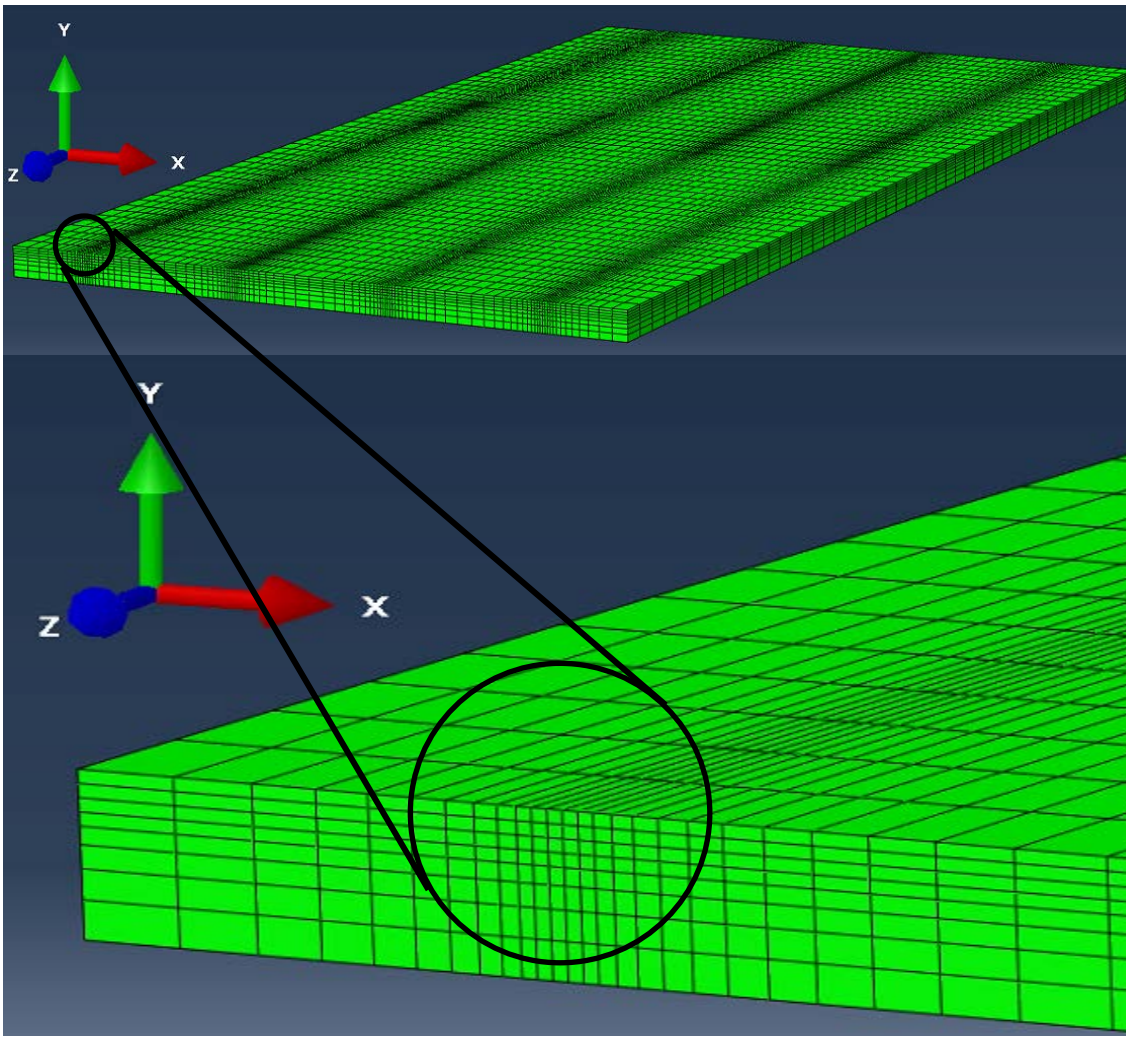

Figure 22. Example of FEA laminate model mesh using square wire assumption.

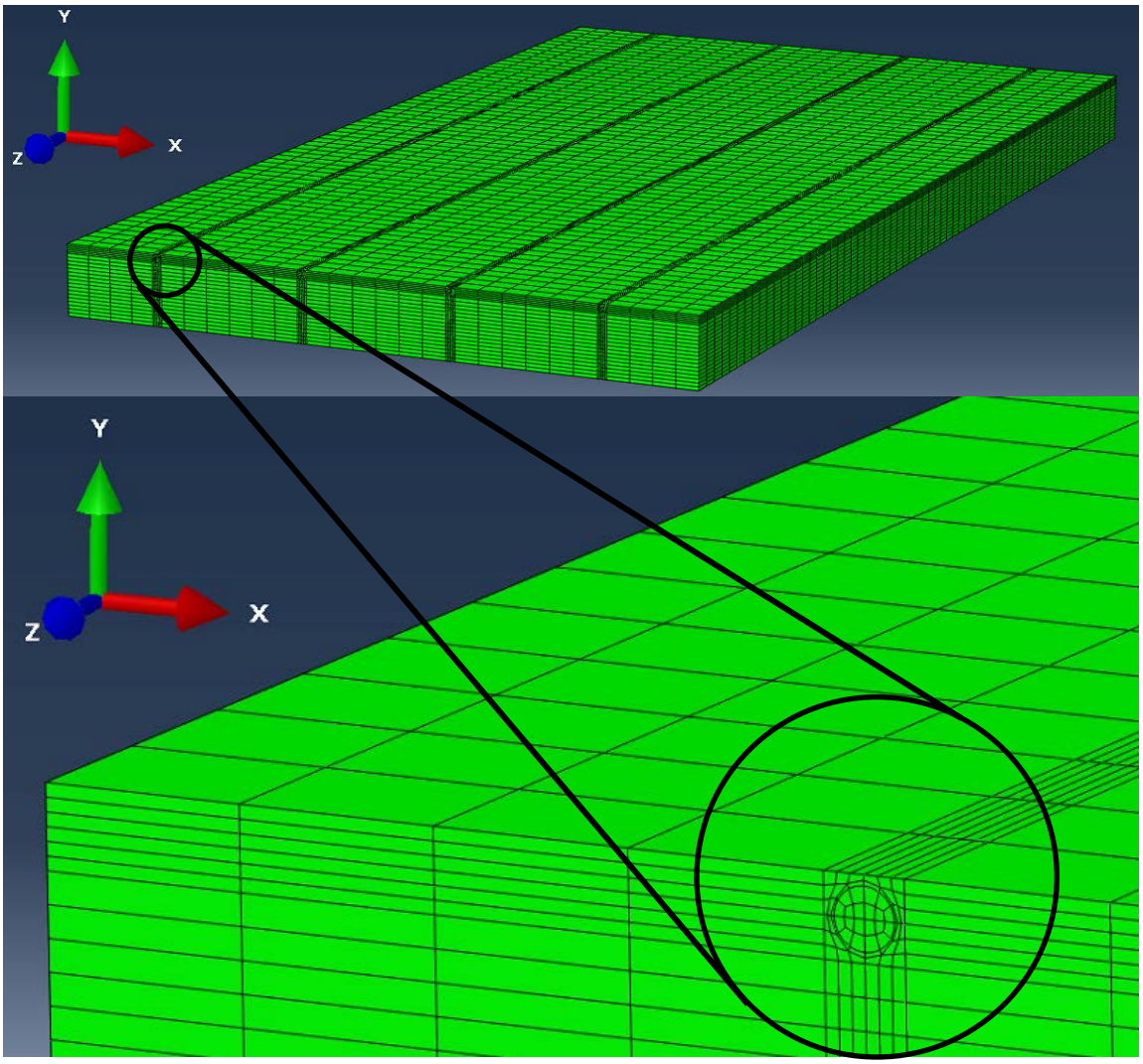

Figure 23. Example of FEA laminate model mesh using round wire assumption.

In order to investigate the effect of changing the level of mesh refinement in the FEA model, the size of the meshing seeds were varied and the results of the FEA simulation compared for one of the laminate samples. For this investigation, the FEA model of sample 2 was used with a square wire approximation. For consecutive

iterations the size of the mesh seeds were changed and constrained to fixed partitions placed in regards to the dimensions and locations of the SMA wires. The relative size of the mesh seeds in each iteration is larger than the size of the seeds used in the finest mesh by the specified multiplier; as Table 8 shows, mesh seeds in mesh refinement 1 are eight times larger than mesh seeds in mesh refinement 6. Some of the mesh refinement variations are shown in Figure 24 to highlight how the mesh density changes as the mesh seed size is altered. Results from the convergence investigation are given in Table 8 and Figure 25.

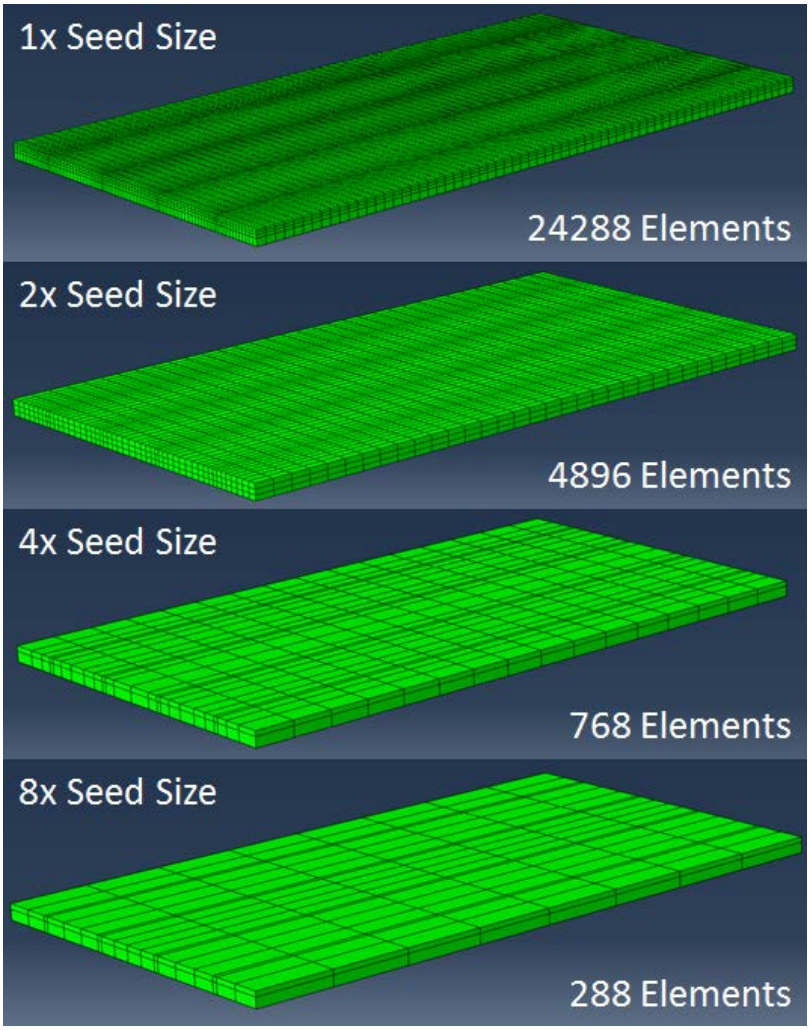

Figure 24. Mesh convergence iterations for square wire geometry model.

Table 8. Mesh convergence iteration results for square wire geometry model.

	Mesh Seed Size Multiplier	Total Number of Elements	Predicted Radius of Curvature (mm)
Mesh Refinement 1	8	288	151.5
Mesh Refinement 2	4	768	144.7
Mesh Refinement 3	3	1320	136.2
Mesh Refinement 4	2	4896	141.8
Mesh Refinement 5	1.5	11264	144.1
Mesh Refinement 6	1	24288	143.9

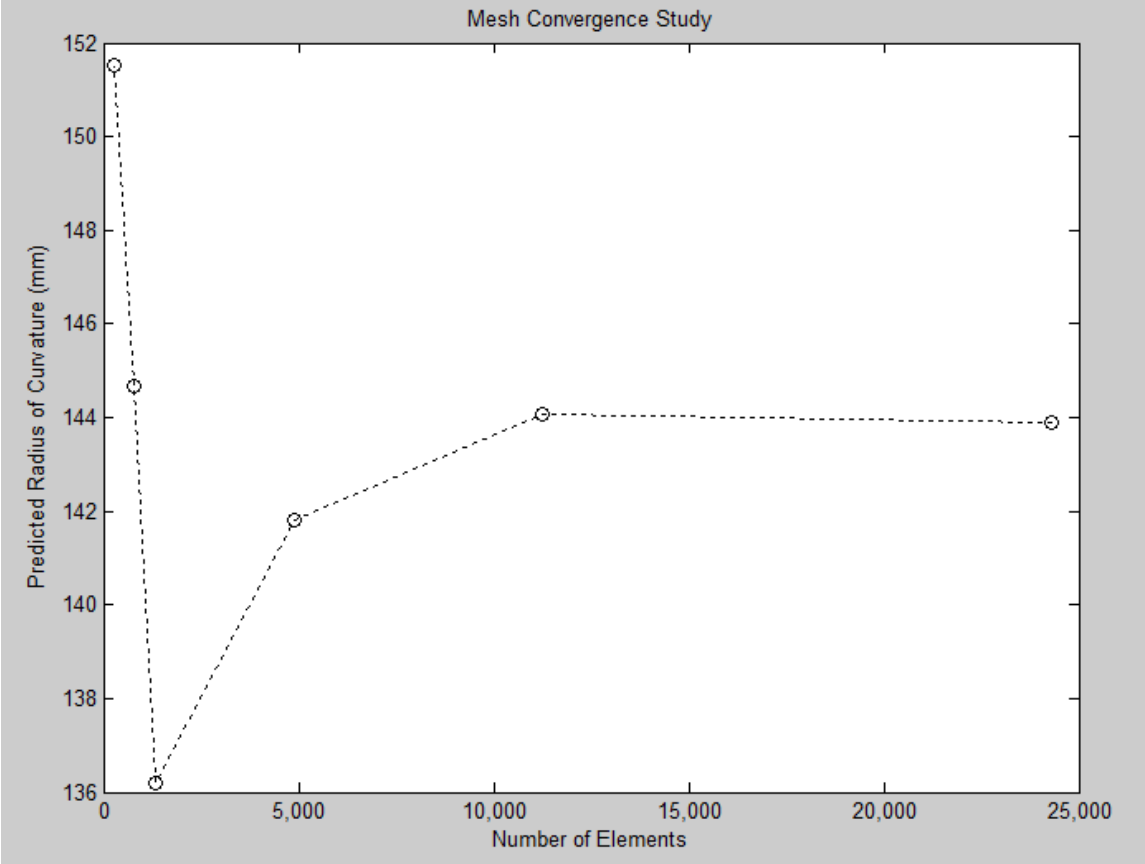

Figure 25. Radius of curvature prediction with increasing mesh refinement for square wire geometry model.

For all comparisons to other simulations or to experimental data, mesh refinement 6 was used as a standard for mesh seed size to prevent yielding erroneous curvature predictions. Mesh refinement considerations were also accounted for in the models considering round wire cross sections and were implemented for all sample cases. In consideration of the relative difference between mesh refinement iterations, it is useful to recall that the difference in predicted radius of curvature between mesh refinement 5 and 6 is smaller than both the measured standard deviation amongst the nominally similar stochastic variants tested and the standard deviation of five iterative trials of any single laminate specimen tested.

4.2 CLASSICAL LAMINATE PLATE THEORY MODELING

Spurred by a desire to sufficiently predict the behavior of embedded SMA mesh laminates at a lower computational cost than that of FEA simulations, Halbert et al. [6, 7] developed a reduced-order model which draws upon classical laminate plate theory while still allowing for a stress distribution within the SMA. The classical laminate plate theory (CLPT) model requires that certain simplifying assumptions be held regarding the modeled system, including: perfect bonding between adjacent layers, linear variation of in-plane strains through the thickness, zero transverse strain, and zero transverse normal stress. From these assumptions, governing equations can be developed by decomposing the elastic strain and 3D equations of equilibrium. The model combines these laminated plate equations with the SMA constitutive equations proposed by Lagoudas et al. [38] to solve for the curvature of the laminate sheet.

Halbert et. al. [6, 7] discuss that, as a means of reducing the order of the model, the analysis is simplified to one dimension such that variation is only considered in the z direction, as defined in Figure 27. To approximate the SMA laminate, the CLPT model uses geometric parameters of the physical system to create two types of effective layers; layers which contain both SMA and elastomer material, and layers which contain only the flexible elastomeric material. To ensure that variation occurs only in the z direction, layers which include both SMA and elastomer material must be reduced to a single effective medium. This effective layer homogenization is substantially different from the FEA models previously described, whereby the elastomer and wire were modeled independently and in great detail. Figure 27 shows the approximation of the real system as an effective medium layer description of the system. To obtain effective properties in order to describe behavior of the SMA/elastomer layers, a spacing factor is used to represent the ratio of the wire spacing to the wire thickness. SMA properties are scaled either directly or inversely with this spacing factor as appropriate. The CLPT model was verified and validated against high fidelity FEA models of the SMA laminate system using effective layers incorporating SMA and elastomer properties [6].

In this validation, both one-sided and two-sided SMA laminate configurations were tested for cases considering total laminate thicknesses of 1.2 mm and 3 mm, and two different wire spacing factors, which represent the ratio of wire spacing to wire thickness. The results from the validation for the one-sided cases are shown below in Figure 26. All test cases for the validation of the CLPT model compared to effective medium FEA models showed RMS error in the prediction of radius of curvature less

than 20% relative to the FEA models. For the cases in the validation study, the CLPT model was able to simulate each case in less than one second, while the corresponding FEA model required more than one minute per case. This highlights that the CLPT model provided a reduction in computational requirements compared to FEA while maintaining an RMS error below 10% for most cases and less than 20% for all cases [6].

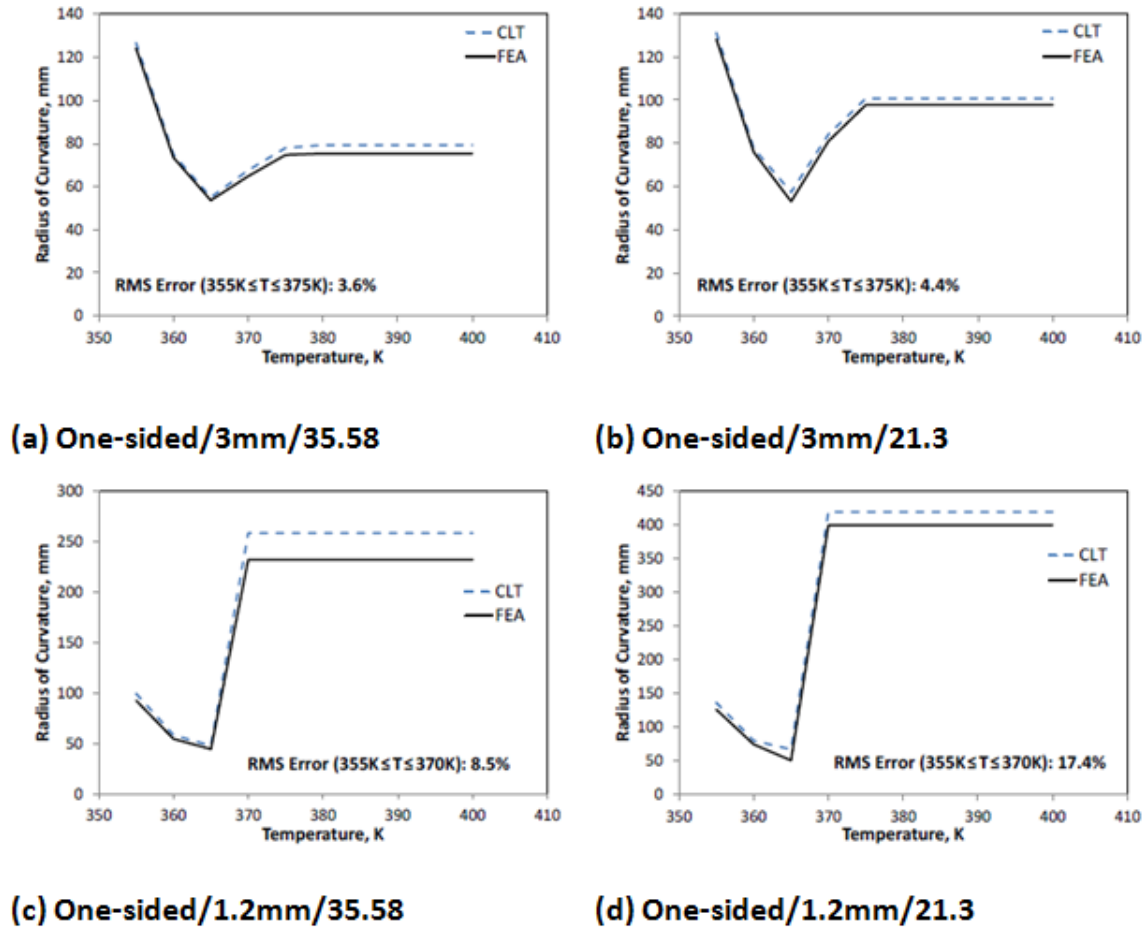

Figure 26. Radius of curvature for CLPT and FEA models with increasing temperature for one-sided cases [6].

While the FEA models used in their validation of the CLPT model used effective medium layers, the FEA models developed and discussed in this work consider individual wires within the laminate layer to analyze SMA and elastomer behavior separately instead of as a single effective medium; the models developed for comparison to experimental samples do not combine the material properties to create an effective medium layer.

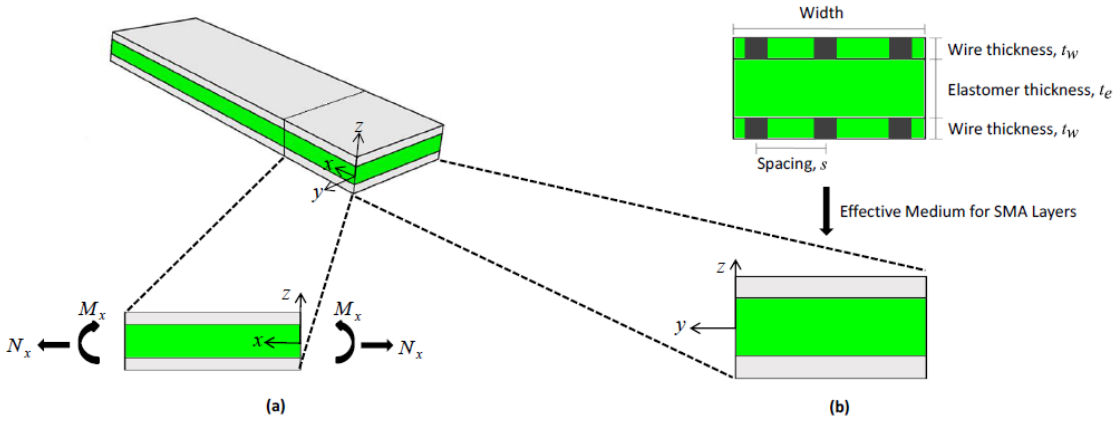

Figure 27. Illustration of (a) free body diagram of laminate system and (b) approximation of real system geometry as effective medium layer description [6].

Only the one or two-sided reduced complexity laminate variations can suitably be modeled using the CLPT modeling method; laminate variations which include SMA wires oriented in more than a single axial direction would be misrepresented by the model. Additionally, this model assumes that the response of the laminate is uniform along the *y* axis. While this simplification is convenient for later calculating a radius of curvature response, as the entire top surface is predicted by CLPT to have a single radius

of curvature, it is a simplification which may not accurately reflect the real surface. While a constant radius of curvature is useful for approximating the system behavior, the FEA model shows that interactions between the SMA and elastomer can affect the surface topography. Figure 28 illustrates this interaction near a free end of the laminate, as simulated using FEA.

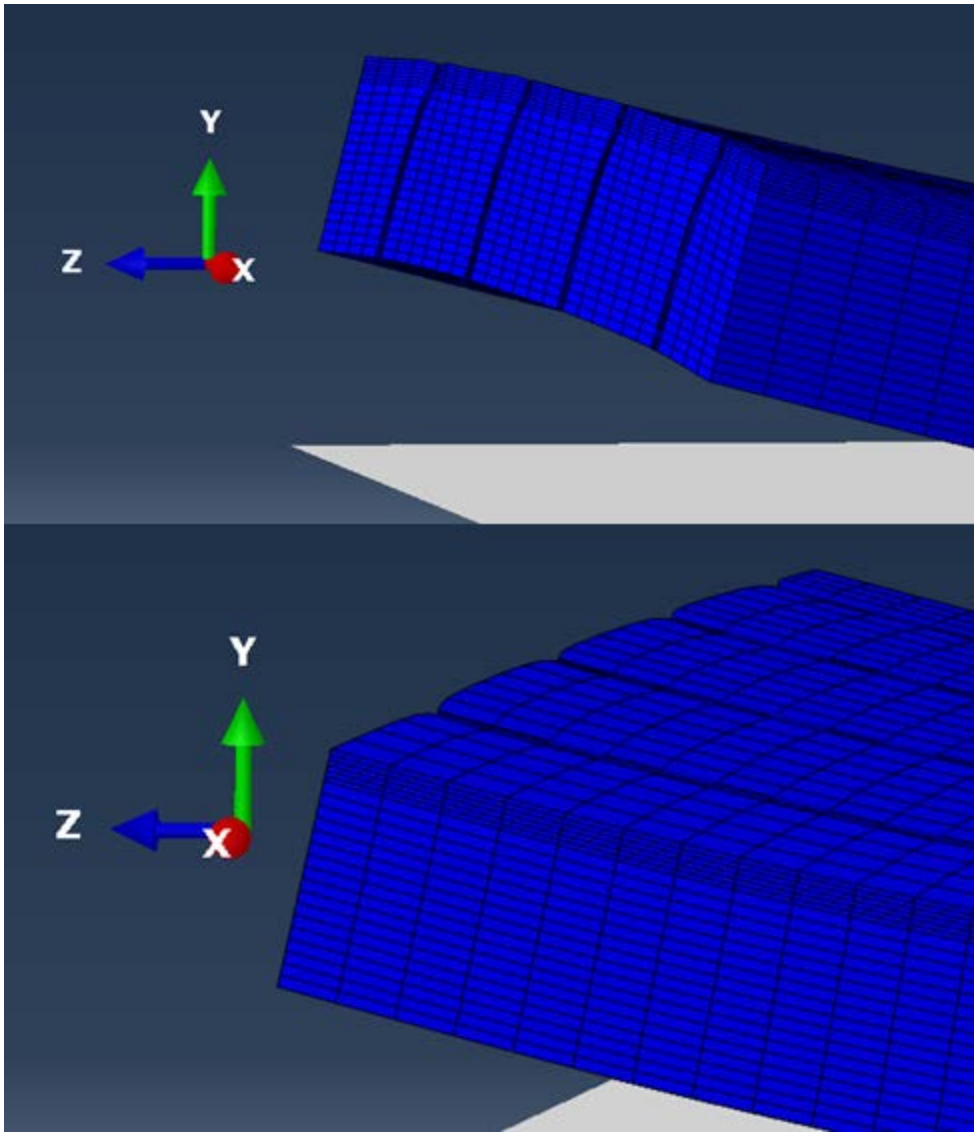

Figure 28. FEA simulated effect of material interactions on surface shape near free end, including: (top) small relative curvature variation along width, and (bottom) elastomer distortion by SMA wire contraction.

4.3 MODELING RESULTS

No model perfectly represents the physical system it characterizes; modeling assumptions are generally a part of a simulation which sacrifices accuracy for simulation

speed. However, before an informed decision can be made regarding an appropriate tradeoff between accuracy and speed, the amount of accuracy sacrificed should be considered. In other words, how valuable is each modeling assumption? In consideration of the SMA laminate concept, the modeling assumptions investigated include: modeling the wires as square or round, gravity effects for small samples, and simulation using FEA or CLPT. All of the models assume a uniform thermal distribution, perfect bonding between SMA wire and elastomer material, and that sample dimensions adhere to their nominal measured values as presented in Chapter 3. Table 9 presents the different sets of modeling assumptions for the different physics-based models considered in this work.

Table 9. Modeling assumptions considered.

	Method	**Gravity Consideration**	**SMA Shape**
Physical System	3D DIC	Gravity	Round Wires
Model 1	FEA	Gravity	Round Wires
Model 2	FEA	Gravity	Square Wires
Model 3	FEA	No Gravity	Round Wires
Model 4	FEA	No Gravity	Square Wires
Model 5	CLPT	No Gravity	Round Wires
Model 6	CLPT	No Gravity	Square Wires

The performance of the real system will be affected by things such as surface contact and gravity, small variations in the position of the wires relative to the neutral axis, and a non-zero temperature gradient through the sample. Including these things in the physics based model should serve to improve the fidelity of the model. However, certain effects will have a more profound impact on the level of fidelity than others. Choosing a set of assumptions for a physics-based model depends upon understanding the most important factors affecting system performance, and selecting which assumptions to incorporate to achieve a model whose accuracy and speed are acceptable for its intended application.

Each of the six models was implemented for each of the three samples, and the radius of curvature in the direction of folding was calculated. These results are shown in Table 10. From these results, it is apparent that the modeling assumption differences between the six models yield notably different predictions for the system behavior.

Table 10. Physics-based model radius of curvature prediction.

Radius of Curvature Prediction (mm)	Sample 1	Sample 2	Sample 3
Model 1	61.0	76.2	133.5
Model 2	87.2	104.3	169.8
Model 3	49.1	41.4	63.5
Model 4	70.6	140.0	91.4
Model 5	57.4	47.1	65.9
Model 6	56.6	43.6	59.5

As might be expected, the FEA models which include gravity considerations generally predict the radius of curvature to be larger than the models which exclude this consideration. For the FEA models, using square wire cross section approximation consistently yields a higher prediction for the radius of curvature compared to modeling the wires as having a round cross section. Although the CLPT model actually predicts a larger radius of curvature for round cross section wires, the CLPT model yields predictions are fairly similar regardless of whether the wires are considered to have a round or square cross section.

To investigate tradeoffs between sets of modeling assumptions, we can use the same tool developed to compare the simulation results to experimental results – by superimposing multiple model-generated surfaces with the data for the real surface measured by DIC, the mean Hausdorff distance measurement can provide a quantitative measure of how well each set of assumptions models the real surface. These comparisons will be presented in Chapter 5.

5. VALIDATION

Having established the methods used for experimentally measuring surface deformations in Chapter 3 and developing physics-based models to simulate system performance in Chapter 4, this chapter is intended to introduce and discuss the methods by which measured and simulated data are compared for the purposes of operational model validation. This chapter discusses verification and validation as used in the context of comparing these data, presents how multiple surfaces are oriented and aligned for meaningful comparison, and how the mean Hausdorff distance is employed to distinguish between differences in surface deformations. The results of comparing simulation and experimental data are also presented and discussed to investigate the ability of the developed models to predict system behavior.

5.1 EXPERIMENTAL VALIDATION OF MODELS

In the context of model validation and verification, it is important to consider that without verifying that a model is correctly implemented (e.g., discretized and coded) or validating that it performs to a satisfactory level of accuracy, any results produced by the model may not actually reflect realistic system behavior; untested model results should be treated with skepticism. Only once a model has been shown to produce meaningful results should it be used in lieu of experimental testing. No model can ever be perfectly accurate, and there are often good reasons for creating a model to be less accurate than is possible to achieve. However, a model's results are only as useful as they are

trustworthy – verification and validation are the steps by which a model's accuracy is tested so as to build trust that the model can be trusted to perform as desired for its intended use.

Verification is the process of ensuring that a conceptual model is implemented correctly. In the case of creating a computerized model, verification steps ensure that the code works correctly – there may be a more efficient way to do it, but there are no 'bugs' in the code. Validation is the process by which a model is tested to see if it performs as accurately as desired [5, 44]. Often there is a tradeoff between simulation run time and the degree of accuracy which is achievable; a designer must decide what an acceptable balance is for a specific use in order to determine if the model performs adequately. Frequently, it is actually preferable to have a less accurate model which requires fewer resources to run. For example, demonstrations or relative comparisons may not require a high degree of absolute accuracy. In such cases, a fast but less accurate model may suffice.

The comparison of the model output to the experimental data utilizes 3D nodal data from both the 3D DIC measurements and the FEA model. Nodal data was collected from a uniform dispersion of points across the entire top surface of the laminate. This nodal distribution provides the greatest fidelity, as other non-uniform node distributions may bias curvature values towards values that are more representative of a sub-region of the system surface. Further, by using surface nodes for the comparison, it is simple to adjust the area of interest for cases where a comparison of only a portion of the surface is desired. To maintain a faithful comparison, nodal data was taken from DIC and FEA

results corresponding to the top surface of the laminate at the same physical state of the system: the tightest achieved curvature. For the experimental samples, this was found by plotting the curvature of the specimen during actuation and extracting nodal data at the point in time where the maximum curvature was measured.

5.2 HAUSDORFF METRIC IMPLEMENTATION

A program was written using Matlab in order to implement the process of calculating the mean Hausdorff distance (MHD) measurement. After conducting an experiment and running a simulation of the laminate system, nodal data is exported for simulation and experimental data, from Abaqus and Vic 3D respectively. The nodal data exports, for both experiment and FEA simulation, save X, Y, and Z coordinates as three separate one dimensional arrays; this process generates two separate .csv files – one for experimental data and one for FEA simulation. The Matlab program imports the 3D coordinate data from the .csv files and reads each data set to construct two separate three column arrays containing the 3D coordinates for the physical specimen and its modeled counterpart.

Once the coordinate arrays are stored in Matlab, the coordinate data are scaled and reoriented such that both sets of data share a common XYZ orientation and are converted to millimeter units. This process does not change the representation of the data – it is only necessary to account for differences between settings in Abaqus and Vic 3D. Before surfaces can be compared, they must be oriented correctly to one another, placed in a common length scale, and be aligned. Before performing a distance

measurement, the surfaces must be aligned to avoid including a positioning bias in the distance measurement. To do this, a common reference point is used to co-locate the surfaces. For the imposed testing conditions, the specimens fold about their midpoint when heated uniformly, and the middle of the specimen remains in place throughout actuation. As such, the midpoint of the surface in the xy plane (i.e., midpoint in width and length) is chosen as the common reference point. Surfaces compared to one another are translated in the z direction at this point to a common zero on the z axis. This process is used to align multiple surfaces by a physically meaningful reference point to a common origin. While this process is relatively straightforward for the reduced complexity case of the SMA laminate concept, choosing a meaningful reference point may require careful consideration for more complex shapes or systems.

Next, the area of the surface considered is trimmed such that comparisons account only for common regions of the laminate. This is necessary as the data collection area of the DIC is necessarily smaller than the overall speckled area, dependent upon the subset size used in analysis. Physics-based models must be sized to match the same physical dimensions of the tested sheet, but comparisons must be made within the area measurable by the DIC. Figure 29 illustrates this reduced area of consideration. If this process is not performed, the Hausdorff distance measurement may include bias, in that the compared surface data would not be sized similarly.

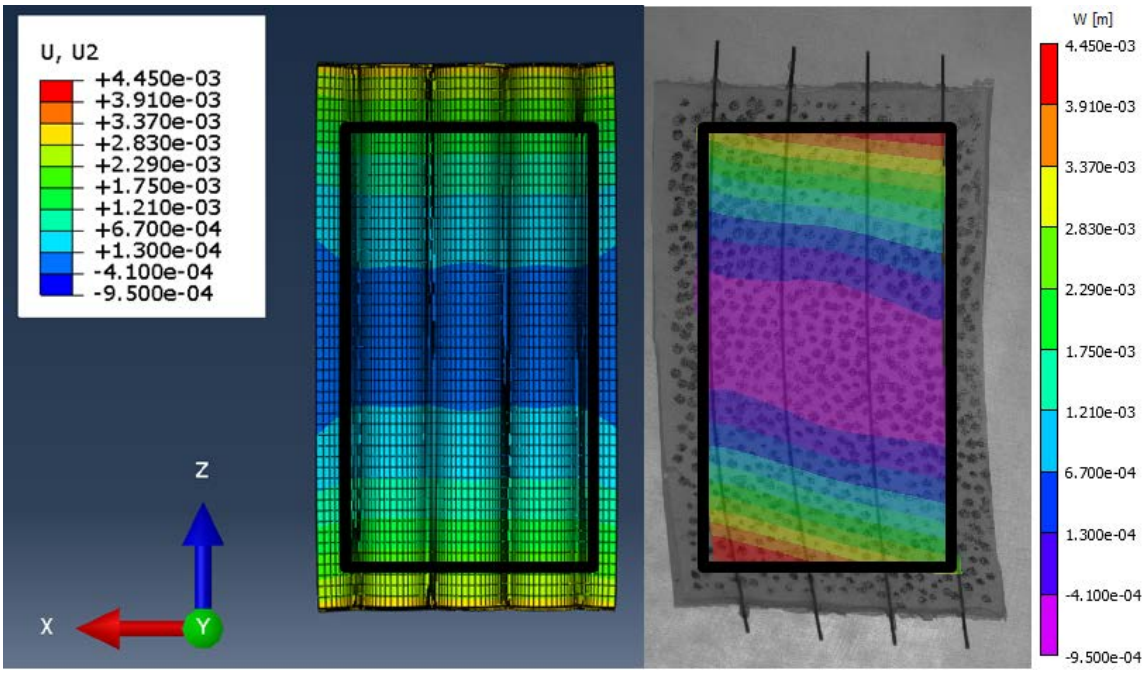

Figure 29. Reduced area of consideration for comparison between FEA models (left) and DIC data (right).

To carry out the Hausdorff distance calculations, the surface data for both experimental and simulation data are passed to Metro, which was developed as a general tool to compare the difference between surfaces [26]. The Metro program approximates provided surfaces as triangulated meshes and then computes the Hausdorff distances between surfaces. The MHD is returned for use as a measure of surface geometry similarity in data comparison for the purpose of model validation [26].

In order to verify that the program used to perform the mean Hausdorff distance measurement calculation was implemented correctly, two sets of test data were generated such that the two data sets represented the same surface, but offset (i.e.

translated and rotated) from one another in space. To verify that the code behaves appropriately, the program should be able to return a mean Hausdorff distance measurement (MHD) of zero for two identical surfaces. Further, it should be able to handle surfaces which are not referenced to the same position or orientation. To test these conditions, the two sets of data chosen were based off of a single experimental trial surface measurement such that the surface in the second data set was a rigid body displacement and rotation of the surface in the first data set, offset in x, y, and z axes. Figure 30 and Figure 31 show the test surfaces before and after alignment, respectively.

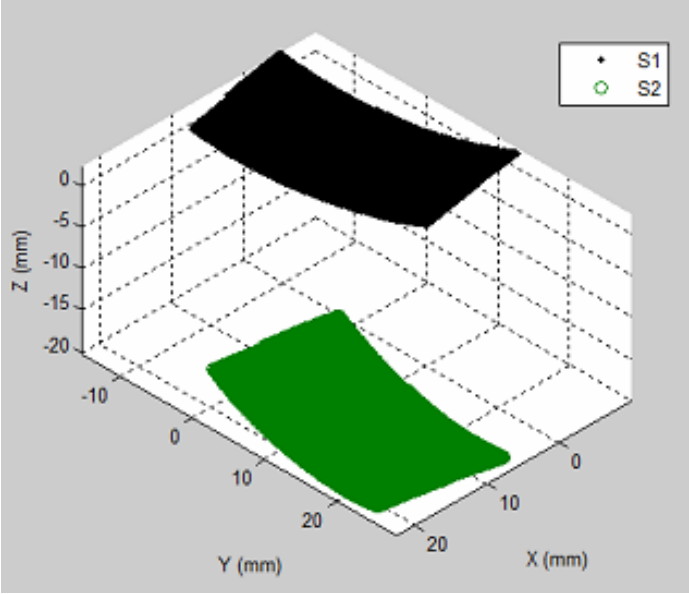

Figure 30. Test surfaces S1 and S2 prior to aligning position and orientation.

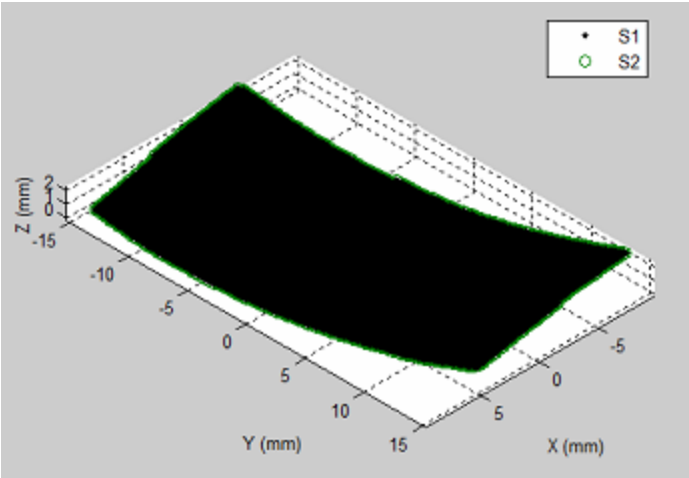

Figure 31. Test surfaces S1 and S2 after realignment and reorientation.

Prior to the realignment, the mean Hausdorff distance was calculated to be 22.1845 mm. Following alignment of the test surfaces at a common reference point, the mean Hausdorff distance was calculated and found to be zero. This demonstrates the ability of the program to reorient surfaces displaced and rotated from one another in multiple directions and highlights the importance of referencing the surfaces to a common point, as the MHD is non-zero before the surfaces are moved to a common reference point. It also verifies that the program correctly calculates a mean Hausdorff distance of zero for two identical surfaces superimposed upon one another.

After the surfaces for the experimental and simulation data are trimmed, reoriented, and co-located, the program generates new simulation surfaces using a user directed number of points. This number, N, represents the number of points generated in each dimension for the considered object; for a comparison between lines, the line will contain N points. For the surfaces considered here, each surface will contain N^2 points,

where N is specified by the user at the start of calculation and used by Metro to generate surfaces for calculation. It is actually these surfaces that are used in the Hausdorff calculation instead of the raw surface data. This aids the program later when the Hausdorff distance is measured between points, as each surface will now contain points with consistent spacing dictated by the desired level of refinement and interpolated spacing based on the surface size – taking the surfaces generated separately by the FEA model and from the DIC may result in different spacing between observed data, as the data sets may be of different sizes. This spacing mismatch can potentially bias the Hausdorff measurement, as the Hausdorff distance can only be measured at discrete points on each surface. As such, it is important to consider how the user-directed number of points affects the outcome of the Hausdorff measurement. The greater the number of points, the finer the resolution of the generated meshes becomes. This leads to greater precision in the final mean Hausdorff measurement. However, this increase also greatly increases the amount of time required to perform the calculation, as the distance must be measured at each point.

To consider the benefit of increasing N for improved measurement accuracy, a simple study was performed. Experimental data was collected for a one sided laminate with SMA wires in a single axial direction, heated from room temperature to 100°C. The laminate utilized NiTi wire with a diameter of 0.3 mm, spaced 3.25 mm apart, and the entire laminate was nominally 1.2 mm thick. An FEA model was created to match the dimensions of the specimen and the testing conditions. Nodal data for the top surface of the laminate for both simulation and experiment were taken at a common state. The data

was then read by the Hausdorff measurement program. Figure 32 shows the mean Hausdorff distance measurement between the surfaces and the corresponding time required to complete the calculation.

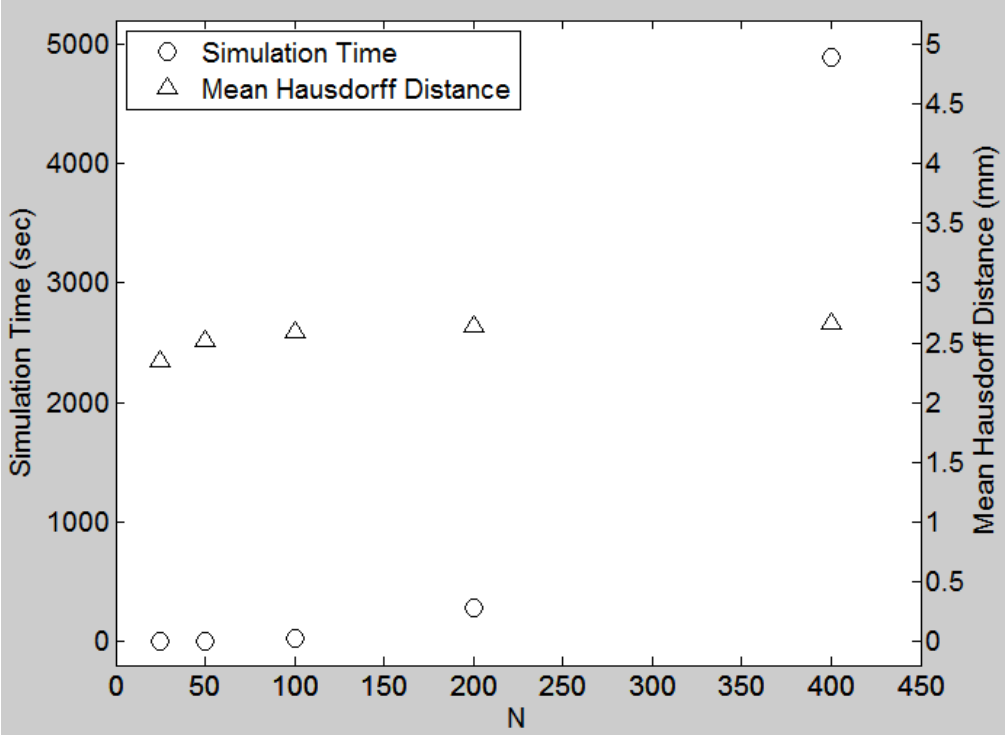

Figure 32. Tradeoff between calculated mean Hausdorff distance and required simulation time.

From this plot, it is apparent that as N is increased past a certain value, the time required to complete the simulation rapidly increases, while the computed mean Hausdorff distance converges quickly towards a constant value with increased values of N. At some point, it becomes impractical to invest an increasing amount of resources to obtain a prediction which approaches the steady state value increasingly slowly. This

point must be determined with regards to the indented purposes for which the prediction will be used, but the decision need not be entirely subjective. It is important to consider that there is a real resolution of the instruments used to capture the experimental data for a particular test setup, such as the 3D DIC cameras. One should not invest additional resources to obtain a prediction whose marginal shift towards the steady state value is within the resolution of the test setup. Any measurement can only be as precise as the least precise tool used to take the measurement. Table 11 shows the numerical results of performing the mean Hausdorff distance (MHD) measurement calculation with increasing N. In order to highlight the difference between distance measurements for each increase in required simulation time, the percentage difference was calculated, using the average of the two approximations as a reference such that:

$$Percentage\ Difference = \frac{|MHD_{N_1} - MHD_{N_2}|}{\frac{1}{2}(MHD_{N_1} + MHD_{N_2})} * 100\% \quad (5)$$

Table 11. Tradeoff between percentage difference in mean Hausdorff distance and required simulation time.

N	Simulation Time (sec)	Mean Hausdorff Distance (mm)	Percentage Difference in MHD	Additional Time Required (sec)
25	1.8485	2.3449	-	-
50	3.3008	2.5179	7.12%	1.4523
100	21.0953	2.5965	3.07%	17.7945
200	277.4475	2.6407	1.69%	256.3522
400	4887.9754	2.6623	0.81%	4610.5279

More important than the quantitative results of this convergence study are the trends shown; for each MHD calculation, increased refinement of the surfaces used for calculation will yield results closer to the converged MHD value but may take much longer to calculate. Where accuracy is desired, a higher value of N should be used. If a fast result is needed, lower values may be used, though at reduced accuracy. For the comparisons presented in this work, $N = 250$. The density of discretized points used in the Hausdorff calculation is given by:

$$Point\ Density = \frac{N^2}{Surface\ Area} \tag{6}$$

For a sample surface 50 mm long and 30 mm wide, this would mean that there are approximately 42 points per square millimeter used in the Hausdorff calculation for each surface in the comparison.

To get a sense of variance among multiple experimental trials, a flat and trimmed reference plane is also situated at the common reference point along with the compared surfaces. A flat reference plane was chosen as it represents the original reference shape of the system before deformation. The MHD can then be calculated between each surface and the reference plane. While this MHD alone is not meaningful in its own right, the standard deviation among the MHD values between each experimental trial surface and the reference plane provides a measure of the variance between the measured surface shapes in each trial.

5.3 VALIDATION RESULTS

Ultimately, for each set of nominal design parameters representing a physically implemented laminate specimen, the comparison code generates results after trimming and referencing experimental and physics-based model surfaces to a common position and reference, including but not limited to: the MHD between each model surface and each experimental trial, standard deviation of the MHD of each experimental trial surface to a common reference surface, and the surface-averaged radius of curvature of each surface.

To help illustrate the usefulness of using MHD to compare experimental trials and to visually compare the differences between the nominally similar specimens, the experimentally measured surfaces are shown in Figure 33. The MHD is measured between each experimental surface and the flat reference plane so that the MHD values can be compared to provide a measure of variation between surfaces. This same process can be used to compare surfaces of a single sample across multiple experimental trials, as illustrated by Figure 34, which shows five trial surfaces for sample 2.

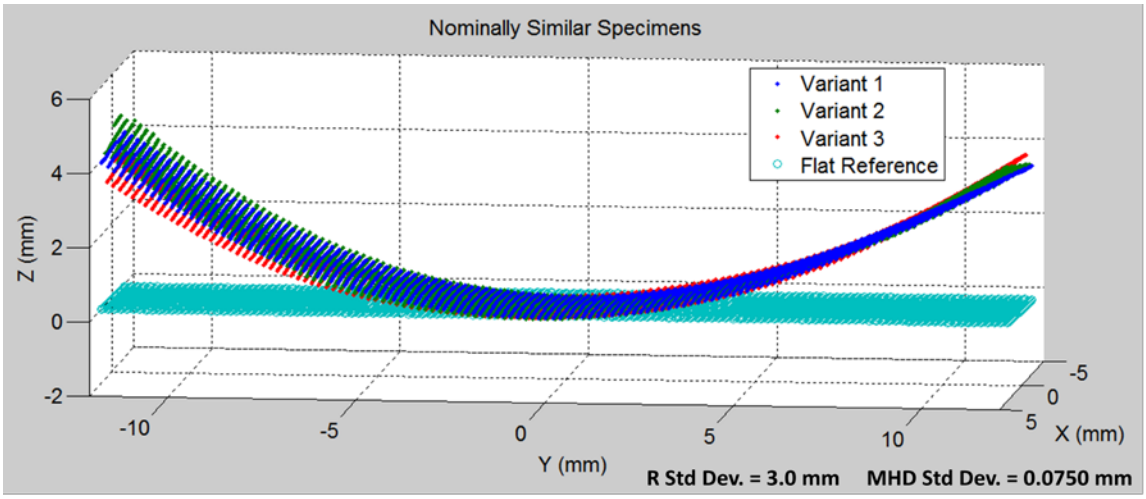

Figure 33. Visual comparison of nominally similar specimen surfaces, measured to common flat reference plane.

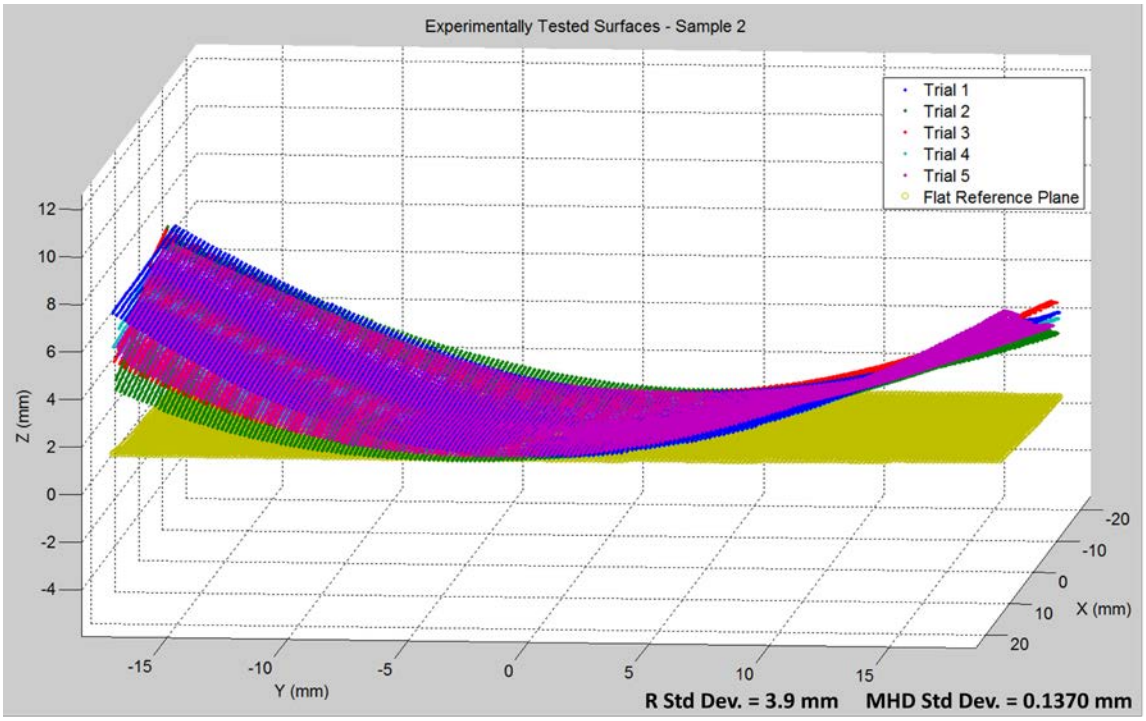

Figure 34. Visual comparison of experimentally measured surface data for a single specimen across five trials.

This flat plane is effectively used to provide a common reference by which multiple surfaces can be compared; as there is not a single “correct” surface to use as a reference for comparison to the other surfaces, the MHD can be calculated between each surface and this reference plane to establish a comparison. This plane can also serve to help provide a dimensionless measure of comparison between simulated surface data and experimental trial surface data. It is common practice to normalize data in order to understand the relation of a particular value to some reference value. In comparing simulated surfaces to experimental trial surfaces, the MHD between the experimental surface and the flat plane is used as the reference value to which the MHD between the simulated surface and the flat plane is compared. However, since it is possible for the MHD between the simulated surface and the flat plane to be greater than the MHD between a particular experimental trial surface and the flat plane, it is more meaningful to create a measure of difference which describes the relative difference between these distances, using the normalized ratio of the MHD values.

As a measure of relative difference between the experimental trial surfaces and the physics-based model predictions, the relative difference ratio (RDR) is calculated via the following equation:

$$RDR = abs\left(1 - \left(\frac{MHD_{MF}}{MHD_{EF}}\right)\right) * 100 \quad (7)$$

where MHD_{MF} is the MHD measured between a model surface and a flat reference surface, and MHD_{EF} is the MHD measured between an experimentally measured surface and a flat reference surface. For a model prediction which exactly matches the physical

system, the relative difference ratio would be 0, indicating that the surfaces are identical; any two identical surfaces superimposed onto one another would have the same MHD to a common reference surface. This ratio provides an intuitive sense of how different the model prediction is from the physical data, without a need for trying to grasp what the significance of the MHD alone means for a length scale which varies with the system being modeled. To consider how the models compare to the experimental data over several trials, the average value of the MHD between the experimental trials and a flat reference surface is used (MHD'_{EF}) to calculate a relative difference ratio for multiple trials (RDR'):

$$RDR' = abs\left(1 - \left(\frac{MHD_{MF}}{MHD'_{EF}}\right)\right) * 100 \tag{8}$$

It is important to consider that the relative difference ratio is not intended to be a sole measure of comparison, but is provided here to help provide a measure of intuition about what the MHD means with regards to a particular system by essentially creating a dimensionless window of margin around the target shape. This is useful because the value of MHD which is acceptable for a certain scale or system application may vary. For example, a MHD of 2 mm may be acceptable for a system whose dimensions are on the order of meters, while the same MHD value may be unacceptable for a system with dimensions on the order of millimeters. The relative difference ratio compares the MHD value to a trimmed, co-oriented, co-located, appropriate reference shape in order to establish a sense of intuitive meaning regarding the MHD value. Figure 35 and Figure 36

illustrate the use of a flat reference plane for comparison of experimental trial and simulated surfaces and the calculation of the relative difference ratio.

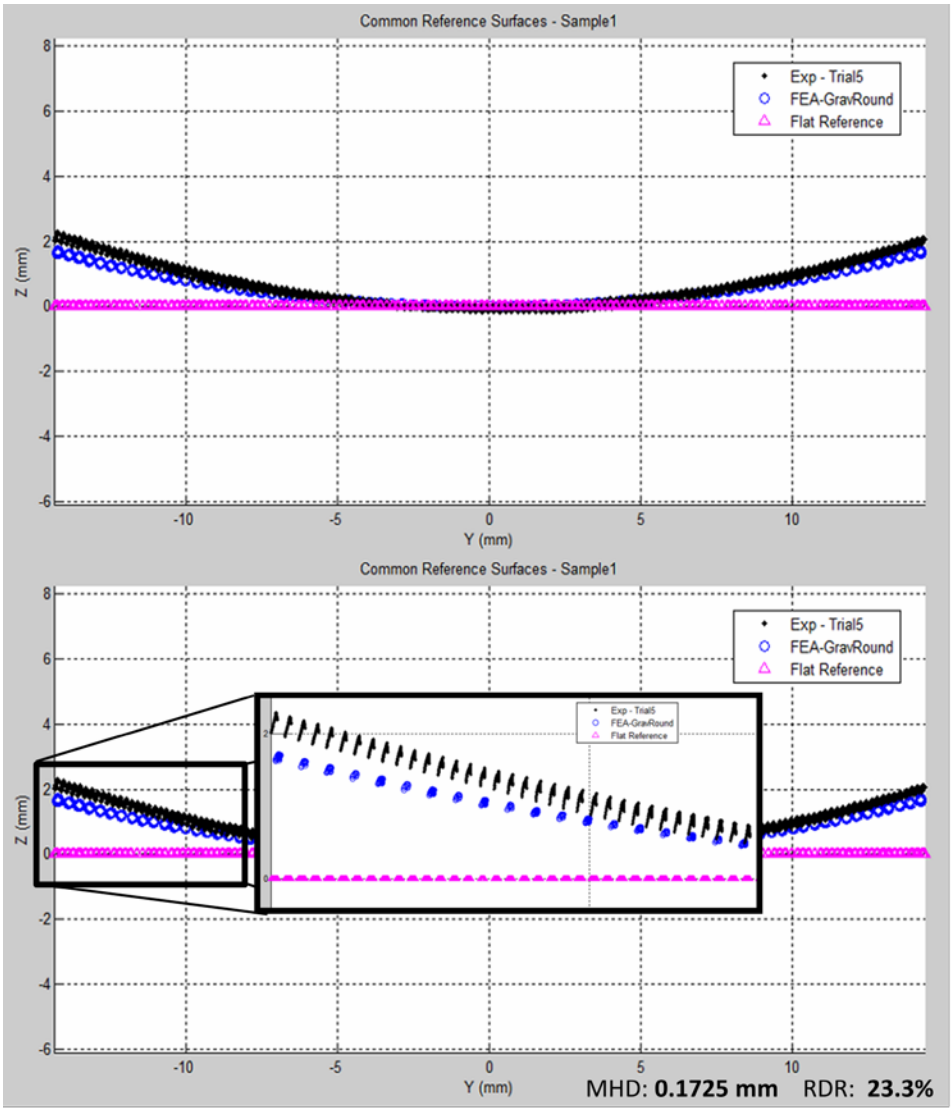

Figure 35. Comparison of experimental and simulated surface data for sample 1 trial 5 and model 1 showing MHD between simulated and experimental surfaces with RDR value. Close up of surfaces shown on bottom.

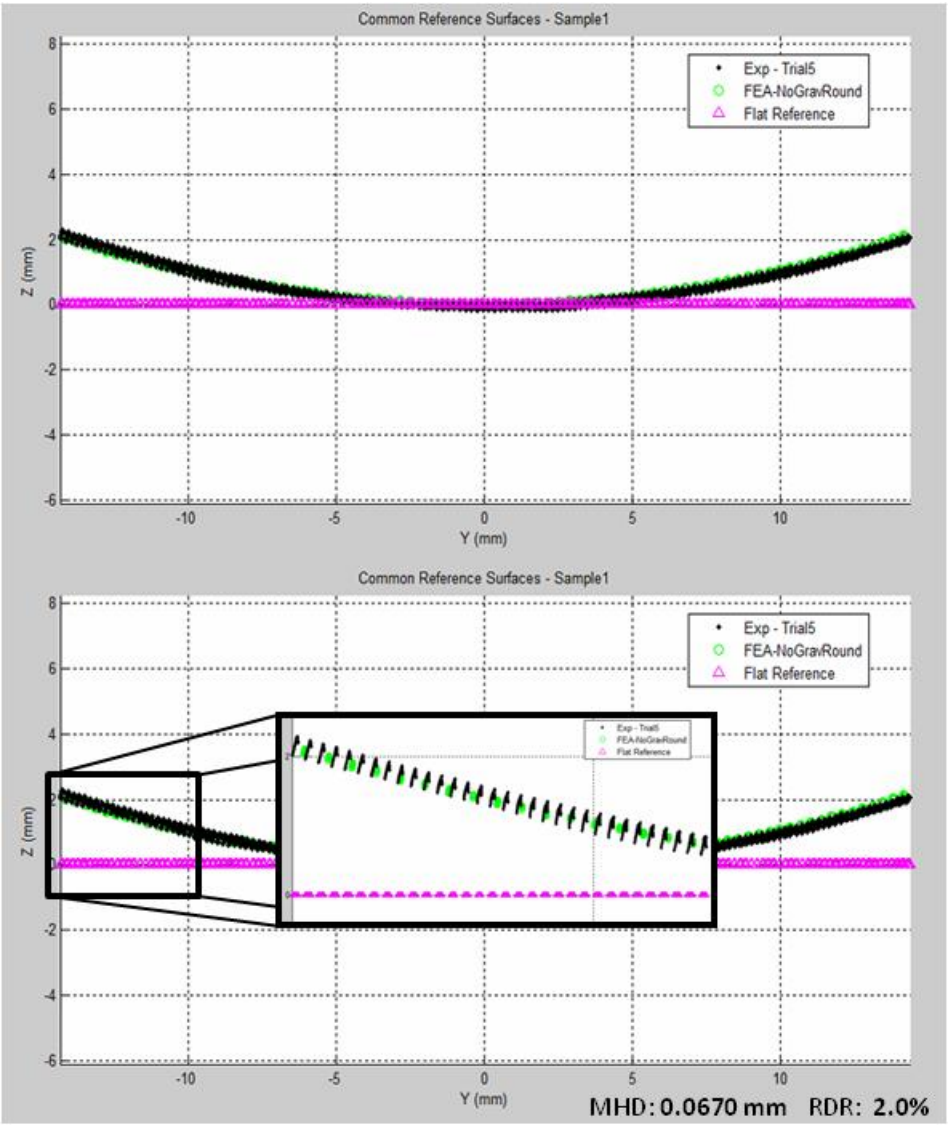

Figure 36. Comparison of experimental and simulated surface data for sample 1 trial 5 and model 3 showing MHD between simulated and experimental surfaces with RDR value. Close up of surfaces shown on bottom.

In addition to considering the MHD value and relative difference ratio, it is also useful to consider the radius of curvature, which is chosen for characterizing behavior of a single fold. In combination, the MHD, relative difference ratio and radius of curvature

portray a clear and meaningful comparison between simulated and experimentally measured data. Table 12 and Table 13 present the key results from comparing data for design parameters representing samples 1, 2, and 3 as defined in Chapter 3. Though the key findings are presented here, the remainder of the data comparing each model to each trial run of each experimentally tested sample is presented in the Appendix.

Table 12. Validation results: MHD values and relative difference ratio

	Average MHD (5 Trials)			Relative Difference Ratio		
	Sample 1 (mm)	Sample 2 (mm)	Sample 3 (mm)	Sample 1	Sample 2	Sample 3
Model 1	0.1544	1.1159	1.4579	21.2%	64.9%	79.8%
Model 2	0.3051	1.2829	1.5165	43.6%	74.0%	83.5%
Model 3	0.0652	0.4358	1.3089	0.7%	14.8%	45.6%
Model 4	0.2227	1.3329	1.2176	29.1%	75.7%	65.9%
Model 5	0.1102	0.5006	0.7793	12.5%	22.2%	39.0%
Model 6	0.1168	0.5684	0.8758	13.7%	29.4%	44.1%
Exp. Data	Std. Dev. in MHD					
	0.0068	0.0924	0.0474			

Table 13. Validation results: radius of curvature values

	Radius of Curvature			% Difference to Avg. Radius of Curvature		
	Sample 1 (mm)	Sample 2 (mm)	Sample 3 (mm)	Sample 1	Sample 2	Sample 3
Model 1	61.0	76.2	133.5	37.8%	12.5%	103.4%
Model 2	87.2	104.3	169.8	11.1%	54.0%	158.6%
Model 3	49.1	41.4	63.5	50.0%	38.9%	3.3%
Model 4	70.6	140.0	91.4	28.0%	106.7%	39.2%
Model 5	57.4	47.1	65.9	40.6%	30.5%	0.3%
Model 6	56.6	43.6	59.5	42.2%	35.7%	9.4%
Exp. Data	5 Trial Average			Std. Dev. in Radius of Curvature (mm)		
	98.0	67.7	65.6	2.5	3.9	1.4

Though the modeling assumptions were previously presented in Section 4.2, they are presented again here in Table 14 for the sake of clarity and ease of reference when considering the validation results.

Table 14. Modeling assumptions considered.

	Method	Gravity Consideration	SMA Shape
Physical System	3D DIC	Gravity	Round Wires
Model 1	FEA	Gravity	Round Wires
Model 2	FEA	Gravity	Square Wires
Model 3	FEA	No Gravity	Round Wires
Model 4	FEA	No Gravity	Square Wires
Model 5	CLPT	No Gravity	Round Wires
Model 6	CLPT	No Gravity	Square Wires

Regarding the performance of the experimental samples presented in Chapter 3, the standard deviation in the MHD and radius of curvature measurements of experimental data is relatively low. For each of the three samples later compared to physics-based models, the relative standard deviation in the radius of curvature measurements is below 6%. Between the three nominally similar variants used to investigate stochastic variance, the relative standard deviation in the radius of curvature measurements was below 7%. This suggests that both the fabrication techniques and methods of measuring and analyzing the performance of the physical specimens are sufficiently developed as to produce consistent behavior for a given set of design parameters. For the purpose of demonstrating the capabilities of the SMA laminate

system, which is continuing to undergo further development, this level of consistency in the fabrication and measurement of physical samples is adequate at this time.

Having established that the experimental data is sufficiently consistent, it is useful to compare the physics-based model predictions to average values of the experimentally measured sample performance. As the validation results show, each of the models which consider the SMA wires to have round wire geometry (models 1, 3, and 5) have a smaller relative difference ratio than their counterparts (models 2, 4, and 6) utilizing the square wire approximation. For the wire geometry consideration, this difference is smaller for the CLPT model (1.6 – 6.4%) than for the corresponding FEA models. This trend is expected for the wire geometry consideration, as the physical system utilizes round wires; models which more closely represent the actual system might be reasonably expected to more closely predict system behavior.

By plotting the average MHD between experimental trial surfaces and simulated surfaces for each sample, as is shown in Figure 37, the trend is again observed that round wire geometry considerations yield better agreement than their square wire counterparts. However, it is also apparent that there is a distinct trend amongst all of the models regarding fidelity across the three samples; for each model, there is a lower MHD for sample 1 than for sample 2, and in most cases the MHD for each model for sample 2 is lower than the MHD for sample 3. For all three samples however, the MHD between simulated and measured surfaces for a given sample is greater than the standard deviation amongst all experimental trials for that sample.

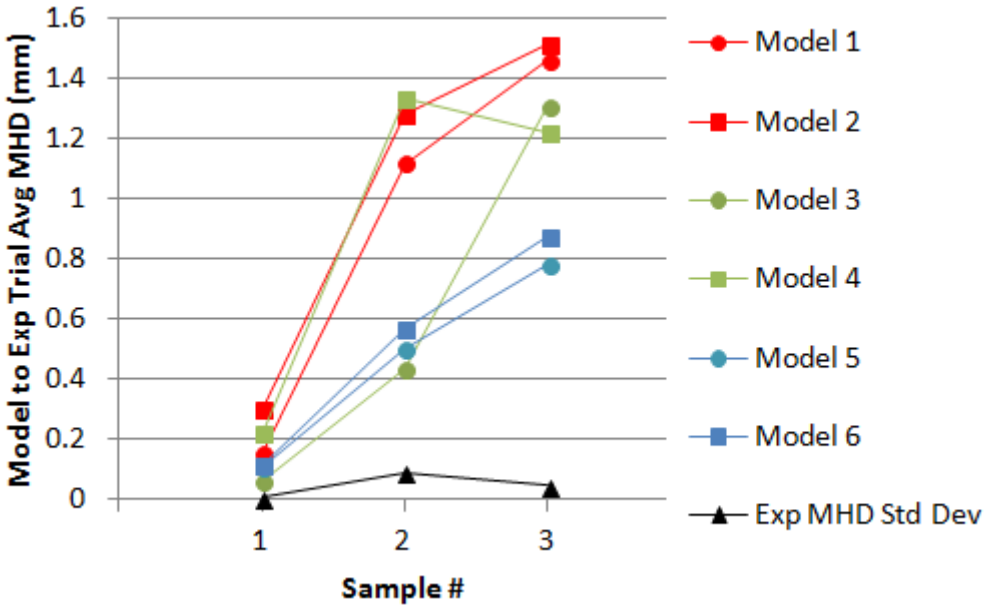

Figure 37. Average MHD as calculated between simulated surfaces and experimentally measured surfaces for each sample.

When considering the MHD or relative difference ratio of Model 3 and 4, which do not consider gravity effects, these models typically predict behavior closer to the measured system than Models 1 and 2, which do consider gravity. Looking at the radius of curvature values for these models, we see that in most cases, Models 1 and 2 have a larger radius of curvature for each sample than their counterparts for the corresponding samples. This trend is shown in Figure 38 and Figure 39 where models considering gravity are shown with dashed lines.

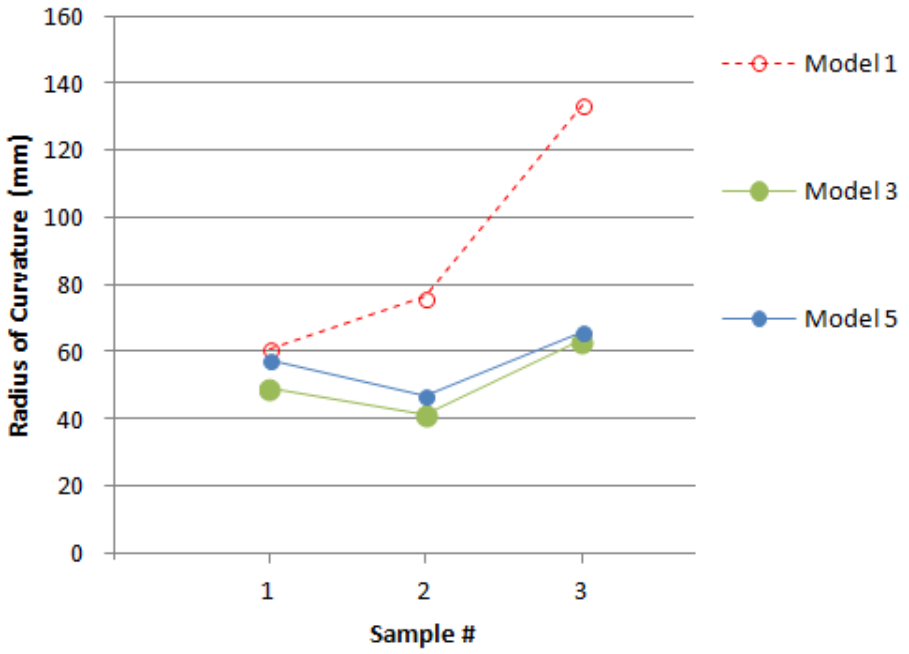

Figure 38. Radius of curvature comparison for comparable round wire models.

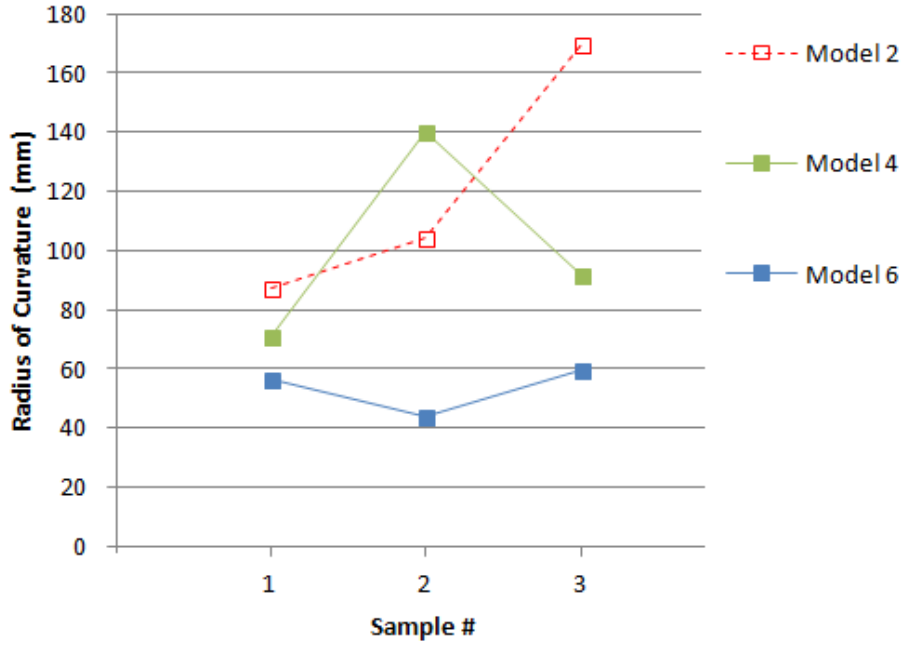

Figure 39. Radius of curvature comparison for comparable square wire models.

One might expect that models considering gravity should yield a higher radius of curvature measurement than a similar model without this consideration, as gravity forces act in a direction opposing the folding motion. The only exception to this trend shown here is that Model 2 has a lower radius of curvature, MHD, and relative difference ratio than Model 4 for Sample 2. While gravity considerations might be expected to yield higher radius of curvature values, one should expect that models with gravity considerations would more closely match the physical system than models that do not account for this.

The fact is that the data contradicts this expectation and there are still large errors between what is predicted by the models and what is measured by experiment. This suggests that the models may not represent the physical system to a sufficient degree. There are several potential factors which may contribute to such a case, including but not limited to: a difference between the material properties used in simulation and real material properties in each physical sample, stress applied mechanically to the SMA during fabrication, defects or variance in the samples causing deviations from nominally measured dimensions, or thermal gradient considerations within the material or the testing enclosure.

6. CONCLUSION

The presentation of the validation framework proposed in this work focuses on an application to the specific case study involving the SMA based laminate system proposed by the research group at Texas A&M University [7-12]. However, by taking a higher level view of the methodology discussed, it is apparent that the framework is applicable to systems beyond the SMA laminate case study. The validation framework accepts data inputs which represent the user specified area of interest for the physical system. This data is input in two forms: simulation data from a physics-based model of the system and experimental data from conducting multiple experimental trials on a physical implementation of the system. Regardless of the system being considered, the validation of any model should consider experimental data in order to compare the simulation results against data reflecting what is physically feasible for a comparable system to achieve.

For systems in which the area of interest undergoes out of plane or complex deformation in three dimensions, such as is the case with the SMA laminate system, the experimental testing procedures used should be chosen so as to faithfully capture this deformation. Methods such as 2D DIC or other simple photogrammetric techniques have limitations as to their accuracy in the out of plane directions and may not adequately capture such deformations. For this reason, 3D DIC techniques are proposed and demonstrated to be a suitable method for adequately capturing the deformations within the region of interest for systems exhibiting out of plane deformations such as the SMA

laminate system. Other stereophotogrammetric, or photogrammetric methods which are augmented with another technique to better capture out of plane distances, may also be suitable for such purposes.

No matter what modeling approach is used in creating simulations to predict system behavior, one should be careful to examine the assumptions of the modeling techniques being used. There are both intrinsic and explicit assumptions in a given model; one must be careful that these assumptions are reasonable for the system being simulated, as a modeling approach which is ill-suited for a certain type of system will likely return inadequate results. Further, it is important to understand the simplifying assumptions chosen. While making fewer simplifying assumptions should generally improve the fidelity of a model, doing so may require additional resources. Additionally, if the system behavior is not fully understood, investigation of the tradeoff between assumptions may help to shed light on which factors have the greatest impact on system performance. After establishing these factors, one may make a more informed decision about what assumptions are reasonable to make for a particular system in a given situation. In this work, the radius of curvature and the MHD were used together to analyze the resulting surface topography of a single fold action induced in the SMA composite sheet. These measures were demonstrated to be useful for comparing experimentally measured surface deformations to simulated surface predictions under multiple sets of modeling assumptions, to assess the impact various assumptions had on surface curvature predictions.

As FEA modeling approaches are commonly used to simulate system behavior, such techniques were used as a baseline for comparison to the experimentally measured samples in the case study presented. Analytical models may also serve well if reasonable assumptions can be made to fit the system behavior to a particular analytical approach. For the SMA laminate system presented, the laminate layer containing SMA material was relatively thin compared to the layer containing only elastomeric material – this allowed the CLPT model, based on classical laminate plate theory, to be reasonably effective [6, 7]. Such considerations must be taken when evaluating an approach to simulating different types of systems.

To validate the physics-based models of the system, there must be a comparison between the simulated and physical sample surfaces. Common approaches typically identify a metric which characterizes the performance of the system measured at some critical location [15-17]. This metric may then be used as a means of comparison between experimental and simulated data. Often, when systems utilizing SMA as an actuator material are modeled, those models rely upon measurements of stress, strain, temperature, martensitic volume fraction, or displacement at certain positions as a basis for confirmation of validation efforts. While these values are important to the system behavior being modeled, these values alone may or may not completely satisfy the behavioral description for which the model was created. It is often the overall shape or state of the deformed system which the model seeks to predict; while stress, strain and temperature measured at critical points are factors which dictate the overall shape or state, a complete comparison might require matching stress, strain, or temperature fields

over the entire surface to convey a complete description needed to make a comparison between experimentally measured data and simulation predictions. For systems where it is applicable, using a shape matching metric such as the MHD achieves this goal without necessarily requiring this stress, strain, or temperature data to be taken at the time of experiment. This is important because it is not always feasible or even possible to obtain stress, strain, temperature, or martensitic volume fraction field measurements over the entire area of interest. Non-invasive stereophotogrammetric techniques such as 3D DIC allow for measured displacement data to be used to calculate strain fields over the entire surface. While photogrammetric methods, which capture data over the entire surface, have been utilized for other types of systems [31-33], it is also viable for many smart material systems applications and has successfully been applied for certain cases [35, 36].

For a deforming system such as the SMA laminate system, the chosen metric for characterizing the performance of a single folding action is the radius of curvature. For comparing multiple surfaces and measuring more complex folding actions, the MHD is chosen as a more powerful metric for comparisons. This radius of curvature measurement considers how tightly the laminate is able to fold – though there may be variations due to defects or non-uniformities in the specimen, this provides an intuitive and meaningful measure of performance directly relating to how tightly the region of interest folds. However, the radius of curvature alone is not sufficient to compare surfaces with more complex surface topography which can result from multiple folds or surface distortions. For this reason, the MHD is the primary metric used for the

comparison of multiple surfaces. While the radius of curvature measurement should be used to describe only a single folding action, the MHD is capable of being used to compare more complicated geometry induced by multiple folding actions as it provides a measure of shape matching.

Incorporating the mean Hausdorff distance into the comparison conveniently conveys the difference between surfaces as a single figure, yet retains the strength of conveying information about the whole surface, as the computation of the MHD considers a fine distribution of distance measurements between surfaces. This allows for the evaluation of small differences such as between experimental variation manifesting in trial data and a high-fidelity model which predicts an idealized system response. The framework proposed in this work demonstrated that this metric can be effectively applied to validating physics-based models considering deformation of a surface in three dimensions. Further, a relative difference ratio can be established using a common reference, such as the flat reference plane used in the case of the SMA laminate system, so that a non-dimensional percentage of difference, based on a normalization of MHD values, can be used to develop an intuitive sense of how much the model differs from the experimentally measured surface without relying upon a unit scale determined by the size of the area of interest. While the relative difference ratio is not mathematically rigorous, it is useful for helping to provide an intuitive understanding of how much variance exists between two similar surfaces using the MHD as a robust method of comparison. Utilizing the MHD in conjunction with the relative difference ratio for data comparison and a more conventional performance metric, like the radius of curvature to

analyze the performance of a single fold for the SMA laminate system, provides a more complete understanding of the difference between model predicted behavior and experimentally measured behavior. This more complete understanding is useful not only for system analysis but also in the development of new models to predict system behavior, as these metrics used together can highlight the value of implementing certain modeling assumptions.

These methods were applied to the SMA laminate system as a case study throughout this work. In regards to the results and discussion presented in Section 5.3, the fabrication techniques and methods used for measuring surface deformations in the SMA laminate system conveyed that the tightest achievable folding state of the system was repeatable and consistent over several varying values of design parameters within a relative standard deviation of 7%. While this level of consistency may be sufficient for some applications, it may be desirable to further refine the fabrication techniques to be able to achieve greater consistency among samples. While the molds currently used are capable of tightly controlling laminate thickness and wire spacing, the mold design could be improved to provide greater consistency for the length and width of the cured sample and provide a more controlled application of stress to the wires as they are woven into place.

In order to predict the system behavior, several physics-based models were developed, using both FEA and CLPT models, to consider the impact of varying multiple modeling assumptions. While some of the trends observed from examining the simulation results tended to reasonably follow expectations, none of the models were

able to sufficiently or consistently predict system behavior across the range of design parameters considered amongst the modeled samples. This suggests that a more accurate model may be needed. While multiple potential factors for this were discussed regarding this shortcoming, further development of a model of the SMA laminate system is recommended.

The notion that one or more factors affecting system behavior are likely misaccounted or unaccounted for even after careful consideration of laminate fabrication, experimental measurement, and model development demonstrates the importance of conducting a thorough validation study prior to relying upon simulation results without confirmation by experimental testing. For complex systems, it is possible that coupled mechanisms have influence over system behavior in a way that is not entirely understood or grasped, or cannot be feasibly modeled. To develop a model which is reliably capable of predicting system performance, evaluating the impact of various modeling assumptions is essential to furthering an understanding of the aspects governing the system performance.

As presented in earlier chapters, the fabrication and measurement of physical implementations of the SMA composite sheet allowed for an investigation of not only the repeatability between multiple nominally similar samples and multiple experimental trials of nominally different parameterized samples, but also allowed for an investigation of varying two design parameters: total laminate thickness and wire spacing. Using 3D measurement techniques to analyze the surface topography at tightest folding, the radius of curvature measurement was used to characterize the tightness of a single fold. The

MHD was then used to capture differences between multiple surfaces for the sake of making a meaningful comparison. By comparing five experimental trials of each of the three parameterized samples, it was observed that total laminate thickness had a much stronger impact on the tightness of folding. This trend is shown in the final figure of Chapter 3.

For more complicated configurations of the SMA composite sheet, the same methods would prove useful for analysis and characterization of system performance. While the radius of curvature is useful for analyzing only a single folding action, the MHD would remain a powerful tool for comparing surface topologies resulting from complex folding actions or even compound folding. Additionally, the MHD was demonstrated to be useful for comparing experimentally measured surface data to surface deformation predicted by simulation. For more complicated system configurations or model implementations, the MHD would continue to be both powerful and useful for capturing subtle differences in surface topography.

While the methods and processes presented and discussed in this work are most immediately valuable for the continuation and extension of the SMA composite sheet development, the methods and processes are useful and valuable for application in other smart material systems. Where the MHD has primarily been used in computer graphics or visualization applications, it is easily implemented for applications where imaging techniques are appropriate to measure system deformations and provides a powerful means of comparing and distinguishing between even small differences between surfaces. This allows the MHD metric and imaging measurement technique pairing to be

useful not only for judging how well simulated system predictions match experimentally measured performance, but also allows for comparisons to be made between multiple experimental trials to establish a means of judging consistency for complicated surface deformations, by using a reference surface. Whereas many systems have conventionally relied upon measurements taken at specific locations to determine how the overall system deforms, these processes provide a more complete analysis by capturing the entire deforming surface.

REFERENCES

[1] Robinson, S., 1997, "Simulation Model Verification and Validation: Increasing the Users' Confidence," Proc. Proceedings of the 29th conference on Winter Simulation Conference, Atlanta, Georgia, pp. 53-59.

[2] Malak Jr, R. J., and Paredis, C. J., 2004, "Foundations of Validating Reusable Behavioral Models in Engineering Design Problems," Proc. Simulation Conference, 2004. Proceedings of the 2004 Winter Simulation Conference, Washington, D.C., 1.

[3] Malak, R. J., and Paredis, C. J., 2004, "On Characterizing and Assessing the Validity of Behavioral Models and Their Predictions," Proc. ASME 2004 International Design Engineering Technical Conferences and Computers and Information in Engineering Conference, Salt Lake City, Utah, pp. 325-336.

[4] Malak Jr, R. J., and Paredis, C. J., 2007, "Validating Behavioral Models for Reuse," Research in Engineering Design, 18(3), pp. 111-128.

[5] Sargent, R. G., 2005, "Verification and Validation of Simulation Models," Proc. Proceedings of the 37th conference on Winter Simulation Conference, Orlando, Florida, pp. 130-143.

[6] Halbert, T., Peraza-Hernandez, E., Malak, R., Hartl, D., 2015, "Numerically Validated Reduced-Order Model for Laminates Containing Shape Memory Alloy Wire Meshes," Journal of Intelligent Material Systems and Structures.

[7] Halbert, T., Moghadas, P., Malak, R., and Hartl, D., 2014, "Control of a Shape Memory Alloy Based Self-Folding Sheet," Proc. ASME 2014 International Design Engineering Technical Conferences and Computers and Information in Engineering Conference, Buffalo, New York, pp. V05BT08A041-V05BT08A041.

[8] Peraza-Hernandez, E., Hartl, D., and Lagoudas, D., 2013, "Modeling of Shape Memory Alloy Wire Meshes Using Effective Lamina Properties for Improved Analysis Efficiency," Proc. ASME 2013 Conference on Smart Materials, Adaptive Structures and Intelligent Systems, Snowbird, Utah, pp. V001T01A009-V001T01A009.

[9] Peraza-Hernandez, E. A., Frei, K. R., Hartl, D. J., and Lagoudas, D. C., 2014, "Folding Patterns and Shape Optimization Using Sma-Based Self-Folding Laminates," Proc. SPIE Smart Structures and Materials+ Nondestructive Evaluation and Health Monitoring, San Diego, California, pp. 90571G-90571G-13.

[10] Peraza-Hernandez, E. A., Hartl, D. J., Frei, K. R., and Akleman, E., 2014, "Connectivity of Shape Memory Alloy-Based Self-Folding Structures," Proceedings of AIAA SciTech, National Harbor, MD.

[11] Peraza-Hernandez, E. A., Hartl, D. J., and Malak Jr, R. J., 2013, "Design and Numerical Analysis of an Sma Mesh-Based Self-Folding Sheet," Smart Materials and Structures, 22(9), pp. 094008.

[12] Powledge, A. C., Hartl, D. J., and Malak, R. J., 2014, "Experimental Analysis of Self-Folding Sma-Based Sheet Design for Simulation Validation," Proc. ASME 2014 Conference on Smart Materials, Adaptive Structures and Intelligent Systems, Newport, Rhode Island, pp. V001T01A016-V001T01A016.

[13] Lagoudas, D. C., Entchev, P., Popov, P., Patoor, E., Brinson, L., and Gao, X., 2006, "Shape Memory Alloys," Mech. Mater, 38(pp. 389-564.

[14] Hartl, D., and Lagoudas, D. C., 2007, "Aerospace Applications of Shape Memory Alloys," Proceedings of the Institution of Mechanical Engineers, Part G: Journal of Aerospace Engineering, 221(4), pp. 535-552.

[15] Chandrashekhara, K., and Bhatia, K., 1993, "Active Buckling Control of Smart Composite Plates-Finite-Element Analysis," Smart Materials and Structures, 2(1), pp. 31.

[16] Hartl, D., Mooney, J., Lagoudas, D., Calkins, F., and Mabe, J., 2010, "Use of a Ni60ti Shape Memory Alloy for Active Jet Engine Chevron Application: Ii. Experimentally Validated Numerical Analysis," Smart Materials and Structures, 19(1), pp. 015021.

[17] Lim, S. M., Lee, S., Park, H. C., Yoon, K. J., and Goo, N. S., 2005, "Design and Demonstration of a Biomimetic Wing Section Using a Lightweight Piezo-Composite Actuator (Lipca)," Smart Materials and Structures, 14(4), pp. 496.

[18] Seelecke, S., and Muller, I., 2004, "Shape Memory Alloy Actuators in Smart Structures: Modeling and Simulation," Applied Mechanics Reviews, 57(1), pp. 23-46.

[19] Peraza-Hernandez, E. A., Hartl, D. J., Malak Jr, R. J., and Lagoudas, D. C., 2014, "Origami-Inspired Active Structures: A Synthesis and Review," Smart Materials and Structures, 23(9), pp. 094001.

[20] Hernandez, E. a. P., Hartl, D. J., Kotz, A., and Malak, R. J., 2014, "Design and Optimization of an Sma-Based Self-Folding Structural Sheet with Sparse Insulating Layers," Proc. ASME 2014 Conference on Smart Materials, Adaptive Structures and Intelligent Systems, Newport, Rhode Island, pp. V001T01A015-V001T01A015.

[21] Hartl, D., Lane, K., and Malak, R., 2012, "Computational Design of a Reconfigurable Origami Space Structure Incorporating Shape Memory Alloy Thin Films," Proc. ASME 2012 Conference on Smart Materials, Adaptive Structures and Intelligent Systems, Stone Mountain, Georgia, pp. 277-285.

[22] Hartl, D., Lagoudas, D., Malak, R., Frecker, M., and Ounaies, Z., 2014, "Active Materials and Structures for Origami Engineering," Smart Materials and Structures, 23(9), pp. 090201.

[23] Schick, J. R., Hartl, D. J., and Lagoudas, D. C., 2012, "Incorporation of Shape Memory Alloy Actuators into Morphing Aerostructures," Morphing Aerospace Vehicles and Structures, pp. 231-260.

[24] Aspert, N., Santa Cruz, D., and Ebrahimi, T., 2002, "Mesh: Measuring Errors between Surfaces Using the Hausdorff Distance," Proc. ICME (1), Lausanne, Switzerland, pp. 705-708.

[25] Chetverikov, D., and Khenokh, Y., 1999, "Matching for Shape Defect Detection," Proc. Computer Analysis of Images and Patterns, Ljubljana, Slovenia, pp. 367-374.

[26] Cignoni, P., Rocchini, C., and Scopigno, R., 1998, "Metro: Measuring Error on Simplified Surfaces," Computer Graphics Forum, 17(pp. 167-174.

[27] Dubuisson, M.-P., and Jain, A. K., 1994, "A Modified Hausdorff Distance for Object Matching," Proc. Pattern Recognition, 1994. Vol. 1-Conference A: Computer Vision & Image Processing., Proceedings of the 12th IAPR International Conference on Pattern Recognition, Jerusalem, Israel, 1, pp. 566-568.

[28] Vergeest, J. S., Spanjaard, S., and Song, Y., 2003, "Directed Mean Hausdorff Distance of Parameterized Freeform Shapes in 3d: A Case Study," The visual computer, 19(7-8), pp. 480-492.

[29] Galvan, E., and Malak, R., 2012, "A Genetic Algorithm Approach for Technology Characterization," Proc. ASME 2012 International Design Engineering Technical Conferences and Computers and Information in Engineering Conference, Stone Mountain, Georgia, pp. 777-788.

[30] Gorthi, S. S., and Rastogi, P., 2010, "Fringe Projection Techniques: Whither We Are?," Optics and lasers in engineering, 48(IMAC-REVIEW-2009-001), pp. 133-140.

[31] Cardenal, J., Mata, E., Perez-Garcia, J., Delgado, J., Hernandez, M., Gonzalez, A., and Díaz De Terán, J., 2008, "Close-Range Digital Photogrammetry Techniques Applied to Landslide Monitoring," International Archives of Photogrammetry, Remote Sensing and Spatial Information Sciences, 37(

[32] Bitelli, G., Dubbini, M., and Zanutta, A., 2004, "Terrestrial Laser Scanning and Digital Photogrammetry Techniques to Monitor Landslide Bodies," International Archives of Photogrammetry, Remote Sensing and Spatial Information Sciences, 35(Part B 5), pp. 246-251.

[33] Bythell, J., Pan, P., and Lee, J., 2001, "Three-Dimensional Morphometric Measurements of Reef Corals Using Underwater Photogrammetry Techniques," Coral Reefs, 20(3), pp. 193-199.

[34] Pan, B., and Li, K., 2011, "A Fast Digital Image Correlation Method for Deformation Measurement," Optics and Lasers in Engineering, 49(7), pp. 841-847.

[35] Cornell, S. R., Hartl, D. J., and Lagoudas, D. C., 2013, "Experimental Validation of a Shape Memory Alloy Constitutive Model by Heterogeneous Thermal Loading Using Infrared Thermography and Digital Image Correlation," Proc. ASME 2013 Conference on Smart Materials, Adaptive Structures and Intelligent Systems, Snowbird, Utah, pp. V002T02A009-V002T02A009.

[36] Cornell, S. R., Leser, W. P., Hochhalter, J. D., Newman, J. A., and Hartl, D. J., 2014, "Development and Characterization of Embedded Sensory Particles Using Multi-Scale 3d Digital Image Correlation," Proc. ASME 2014 Conference on Smart Materials, Adaptive Structures and Intelligent Systems, Newport, Rhode Island, pp. V002T02A010-V002T02A010.

[37] Correlated Solutions, I., 2009, "Digital Image Correlation: Overview of Principles and Software."

[38] Lagoudas, D., Hartl, D., Chemisky, Y., Machado, L., and Popov, P., 2012, "Constitutive Model for the Numerical Analysis of Phase Transformation in Polycrystalline Shape Memory Alloys," International Journal of Plasticity, 32–33(0), pp. 155-183.

[39] Hartl, D. J., Chatzigeorgiou, G., and Lagoudas, D. C., 2010, "Three-Dimensional Modeling and Numerical Analysis of Rate-Dependent Irrecoverable Deformation in Shape Memory Alloys," International Journal of Plasticity, 26(10), pp. 1485-1507.

[40] Hartl, D. J., Lagoudas, D. C., and Calkins, F., 2011, "Advanced Methods for the Analysis, Design, and Optimization of Sma-Based Aerostructures," Smart Materials and Structures, 20(9), pp. 094006.

[41] Widdle Jr, R. D., Grimshaw, M. T., and Shome, M., 2009, "Optimal Design of a Shape Memory Alloy Actuated Composite Structure with Iterative Finite Element Analysis," Proc. SPIE Smart Structures and Materials+ Nondestructive Evaluation and Health Monitoring, San Diego, California, pp. 728818-728818-11.

[42] Manzo, J., and Garcia, E., 2009, "Analysis and Optimization of the Active Rigidity Joint," Smart Materials and Structures, 18(12), pp. 125020.

[43] Oehler, S., Hartl, D., Lopez, R., Malak, R., and Lagoudas, D., 2012, "Design Optimization and Uncertainty Analysis of Sma Morphing Structures," Smart Materials and Structures, 21(9), pp. 094016.

[44] Kleijnen, J. P., 1995, "Verification and Validation of Simulation Models," European Journal of Operational Research, 82(1), pp. 145-162.

APPENDIX A

In further investigation of the FEA simulations, the consequences of using elements with a high aspect ratio in the SMA wires were considered. Two models were created using the methods discussed in Chapter 4, and were developed to be identical except in the establishment of the mesh – both models were partitioned the same way to provide symmetry in the assignment of elements around the wires, but one model had seed size defined manually, while the other allowed Abaqus to automatically assign global seeds to determine the size and shape of elements throughout the mesh. As a consequence of this difference, the elements between the round wire geometry and square partitions in the model have a high aspect ratio, though the aspect ratio of these elements in the automatically generated mesh were lower than in the model with manually defined element seeds by about 20%. Figure 40 shows the change in aspect ratio and associated stress for a particular element in these models. As a result of this change, the stress distribution in the SMA wires at tightest achieved curvature was Figure 3observed to be lower for the higher aspect ratio elements. Comparing the surfaces at tightest folding between these models, no significant difference in predicted curvature was observed; the MHD measured between surfaces of these models was calculated to be 0.0948 mm, and the difference in measured radius of curvature values across the surface was 0.2374 mm.

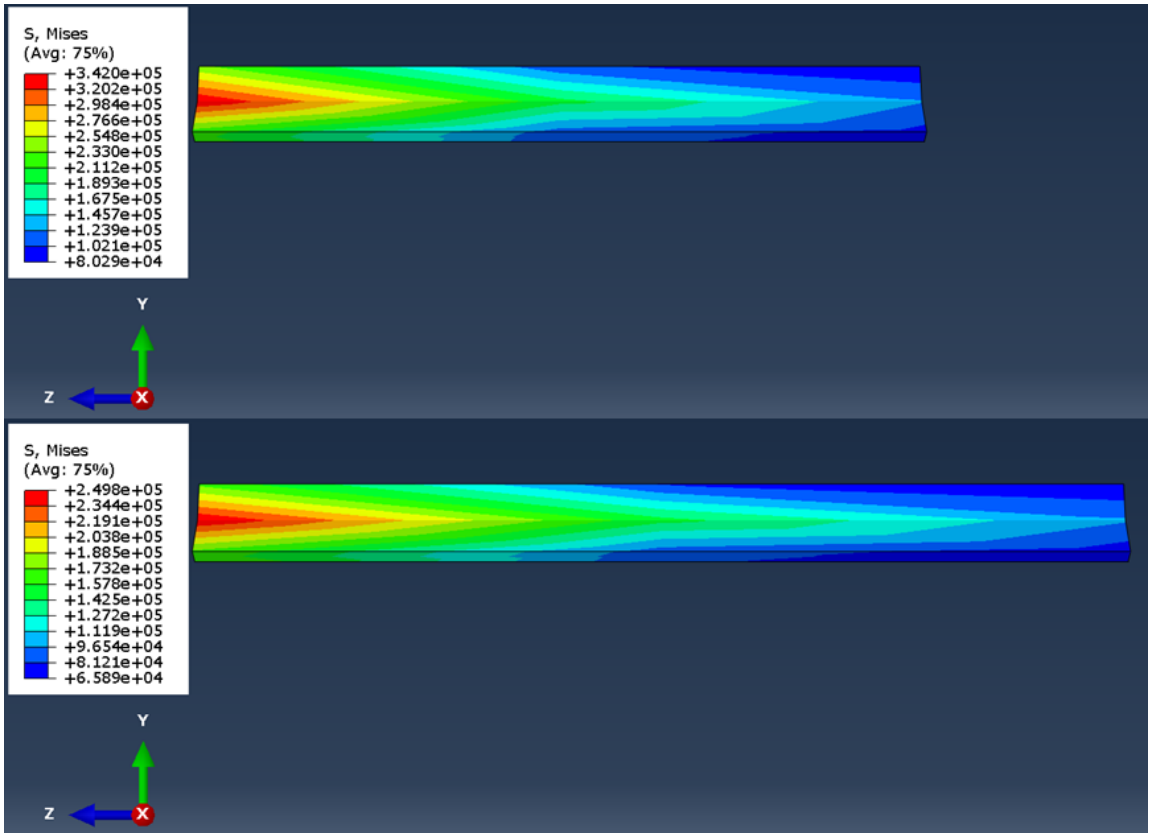

Figure 40. Change in aspect ratio of elements near wire in FEA model: (top) lower aspect ratio, (bottom) higher aspect ratio.

APPENDIX B

The complete analysis comparing all of the physics-based models to each trial run for each of the three experimental sample variants is presented below. Provided in the analysis of each comparison is the summary of the sample characteristics and temperature of tightest achieved curvature, followed by the MHD and associated relative difference ratio between each set of modeling assumptions and each experimental trial. At the end of the data for a given sample, summaries are given providing information about trial average values for MHD and radius of curvature.

```
%%%%%%%%%%%%%%%%%%%%%%%%%%%%%%%%
%  Sample Properties Compared  %
%%%%%%%%%%%%%%%%%%%%%%%%%%%%%%%%

  Nominal Thickness: 3.0 mm
  Wire Spacing:      6.5 mm
  Wire Diameter:     0.3 mm
  Temperature:       361.4 K
  Div. per Dim.:     150 divisions

%%%%%%%%%%%%%%%%%%%%%%%%%%%%%%%%%%%%%%%%%%%%%%%%%%%%%%%%%%%%%%%%%%%%%%%%%%%%%%%
%   Mean Hausdorff Distances   %%   Relative Difference Ratio  %
%%%%%%%%%%%%%%%%%%%%%%%%%%%%%%%%%%%%%%%%%%%%%%%%%%%%%%%%%%%%%%%%%%%%%%%%%%%%%%%
      -----     Displaying Comparison to Trial 1:     -----

With Gravity Constraint:
  FEA  - Round  Wires: 0.1513 mm       Ratio: 20.55%
  FEA  - Square Wires: 0.3010 mm       Ratio: 43.12%

Without Gravity Constraint:
  FEA  - Round  Wires: 0.0743 mm       Ratio: 1.50%
  FEA  - Square Wires: 0.2254 mm       Ratio: 28.54%
  CLPT - Round  Wires: 0.1111 mm       Ratio: 11.81%
  CLPT - Square Wires: 0.1170 mm       Ratio: 13.00%
```

```
%%%%%%%%%%%%%%%%%%%%%%%%%%%%%%%%%%%%%%%%%%%%%%%%%%%%%%%%%%%%%%%%%%%%%%%%%%%%
%   Mean Hausdorff Distances   %%   Relative Difference Ratio  %
%%%%%%%%%%%%%%%%%%%%%%%%%%%%%%%%%%%%%%%%%%%%%%%%%%%%%%%%%%%%%%%%%%%%%%%%%%%%
      -----     Displaying Comparison to Trial 2:     -----

With Gravity Constraint:
  FEA  - Round  Wires: 0.1514 mm       Ratio: 20.70%
  FEA  - Square Wires: 0.3031 mm       Ratio: 43.22%

Without Gravity Constraint:
  FEA  - Round  Wires: 0.0598 mm       Ratio: 1.31%
  FEA  - Square Wires: 0.2258 mm       Ratio: 28.67%
  CLPT - Round  Wires: 0.1077 mm       Ratio: 11.97%
  CLPT - Square Wires: 0.1144 mm       Ratio: 13.16%

%%%%%%%%%%%%%%%%%%%%%%%%%%%%%%%%%%%%%%%%%%%%%%%%%%%%%%%%%%%%%%%%%%%%%%%%%%%%
%   Mean Hausdorff Distances   %%   Relative Difference Ratio  %
%%%%%%%%%%%%%%%%%%%%%%%%%%%%%%%%%%%%%%%%%%%%%%%%%%%%%%%%%%%%%%%%%%%%%%%%%%%%
      -----     Displaying Comparison to Trial 3:     -----

With Gravity Constraint:
  FEA  - Round  Wires: 0.1535 mm       Ratio: 21.38%
  FEA  - Square Wires: 0.3046 mm       Ratio: 43.71%

Without Gravity Constraint:
  FEA  - Round  Wires: 0.0753 mm       Ratio: 0.44%
  FEA  - Square Wires: 0.2177 mm       Ratio: 29.28%
  CLPT - Round  Wires: 0.1112 mm       Ratio: 12.73%
  CLPT - Square Wires: 0.1174 mm       Ratio: 13.91%

%%%%%%%%%%%%%%%%%%%%%%%%%%%%%%%%%%%%%%%%%%%%%%%%%%%%%%%%%%%%%%%%%%%%%%%%%%%%
%   Mean Hausdorff Distances   %%   Relative Difference Ratio  %
%%%%%%%%%%%%%%%%%%%%%%%%%%%%%%%%%%%%%%%%%%%%%%%%%%%%%%%%%%%%%%%%%%%%%%%%%%%%
      -----     Displaying Comparison to Trial 4:     -----

With Gravity Constraint:
  FEA  - Round  Wires: 0.1507 mm       Ratio: 20.79%
  FEA  - Square Wires: 0.3001 mm       Ratio: 43.28%

Without Gravity Constraint:
  FEA  - Round  Wires: 0.0535 mm       Ratio: 1.20%
  FEA  - Square Wires: 0.2130 mm       Ratio: 28.75%
  CLPT - Round  Wires: 0.1040 mm       Ratio: 12.07%
  CLPT - Square Wires: 0.1109 mm       Ratio: 13.26%
```

```
%%%%%%%%%%%%%%%%%%%%%%%%%%%%%%%%%%%%%%%%%%%%%%%%%%%%%%%%%%%%%%%%%%%%%%%%%%%%
%   Mean Hausdorff Distances   %%   Relative Difference Ratio  %
%%%%%%%%%%%%%%%%%%%%%%%%%%%%%%%%%%%%%%%%%%%%%%%%%%%%%%%%%%%%%%%%%%%%%%%%%%%%
      -----     Displaying Comparison to Trial 5:     -----

With Gravity Constraint:
  FEA  - Round  Wires: 0.1651 mm       Ratio: 22.42%
  FEA  - Square Wires: 0.3164 mm       Ratio: 44.45%

Without Gravity Constraint:
  FEA  - Round  Wires: 0.0628 mm       Ratio: 0.89%
  FEA  - Square Wires: 0.2315 mm       Ratio: 30.22%
  CLPT - Round  Wires: 0.1172 mm       Ratio: 13.88%
  CLPT - Square Wires: 0.1244 mm       Ratio: 15.05%
```

```
%%%%%%%%%%%%%%%%%%%%%%%%%%%%%%%%%%%%%%%%%%%%%%%%%%%%%%%%%%%%%%%%%%%%%%%%%%%%
%%                                  %%                                  %%
%%  AVG MHD Across All Trials       %%  Relative Difference Ratio       %%
%%                                  %%                                  %%
%%%%%%%%%%%%%%%%%%%%%%%%%%%%%%%%%%%%%%%%%%%%%%%%%%%%%%%%%%%%%%%%%%%%%%%%%%%%
With Gravity Constraint:
  FEA  - Round  Wires: 0.1544 mm       Ratio: 21.17%
  FEA  - Square Wires: 0.3051 mm       Ratio: 43.56%

Without Gravity Constraint:
  FEA  - Round  Wires: 0.0652 mm       Ratio: 0.70%
  FEA  - Square Wires: 0.2227 mm       Ratio: 29.10%
  CLPT - Round  Wires: 0.1102 mm       Ratio: 12.50%
  CLPT - Square Wires: 0.1168 mm       Ratio: 13.68%

  EXP MHD Std Dev (5 Trials):  0.0068 mm

%%%%%%%%%%%%%%%%%%%%%%%%%%%%%%%%%%%%%%%%%%%%%%%%%%%%%%%%%%%%%%%%%%%%%%%%%%%%
%%                                                                      %%
%%  Surfaced Averaged Radius of Curvature                               %%
%%                                                                      %%
%%%%%%%%%%%%%%%%%%%%%%%%%%%%%%%%%%%%%%%%%%%%%%%%%%%%%%%%%%%%%%%%%%%%%%%%%%%%
  EXP - Surface Trial 1: 94.4 mm
  EXP - Surface Trial 2: 98.3 mm
  EXP - Surface Trial 3: 100.9 mm
  EXP - Surface Trial 4: 99.6 mm
  EXP - Surface Trial 5: 96.9 mm
  ---> 5  Trial Average: 98.0 mm
  ---> 5  Trial Std Dev: 2.5 mm
  ---> Relative Std Dev: 2.6%

With Gravity Constraint:
  FEA  - Round  Wires: 61.0 mm. Diff: 37.0 mm (37.8%)
  FEA  - Square Wires: 87.2 mm. Diff: 10.9 mm (11.1%)

Without Gravity Constraint:
  FEA  - Round  Wires: 49.1 mm. Diff: 49.0 mm (50.0%)
  FEA  - Square Wires: 70.6 mm. Diff: 27.4 mm (28.0%)
  CLPT - Round  Wires: 57.4 mm. Diff: 40.6 mm (41.4%)
  CLPT - Square Wires: 56.6 mm. Diff: 41.4 mm (42.2%)
```

```
%%%%%%%%%%%%%%%%%%%%%%%%%%%%%%%%
%  Sample Properties Compared  %
%%%%%%%%%%%%%%%%%%%%%%%%%%%%%%%%

  Nominal Thickness: 1.2 mm
  Wire Spacing:      6.5 mm
  Wire Diameter:     0.3 mm
  Temperature:       361.3 K
  Div. per Dim.:     150 divisions

%%%%%%%%%%%%%%%%%%%%%%%%%%%%%%%%%%%%%%%%%%%%%%%%%%%%%%%%%%%%%%%%%%%%%%%%%%%%%%%
%   Mean Hausdorff Distances   %%   Relative Difference Ratio  %
%%%%%%%%%%%%%%%%%%%%%%%%%%%%%%%%%%%%%%%%%%%%%%%%%%%%%%%%%%%%%%%%%%%%%%%%%%%%%%%
      -----     Displaying Comparison to Trial 1:     -----

With Gravity Constraint:
  FEA  - Round  Wires: 1.2813 mm       Ratio: 67.81%
  FEA  - Square Wires: 1.4481 mm       Ratio: 76.12%

Without Gravity Constraint:
  FEA  - Round  Wires: 0.5787 mm       Ratio: 21.83%
  FEA  - Square Wires: 1.4984 mm       Ratio: 77.65%
  CLPT - Round  Wires: 0.6670 mm       Ratio: 28.57%
  CLPT - Square Wires: 0.7389 mm       Ratio: 35.26%

%%%%%%%%%%%%%%%%%%%%%%%%%%%%%%%%%%%%%%%%%%%%%%%%%%%%%%%%%%%%%%%%%%%%%%%%%%%%%%%
%   Mean Hausdorff Distances   %%   Relative Difference Ratio  %
%%%%%%%%%%%%%%%%%%%%%%%%%%%%%%%%%%%%%%%%%%%%%%%%%%%%%%%%%%%%%%%%%%%%%%%%%%%%%%%
      -----     Displaying Comparison to Trial 2:     -----

With Gravity Constraint:
  FEA  - Round  Wires: 1.0740 mm       Ratio: 64.12%
  FEA  - Square Wires: 1.2404 mm       Ratio: 73.38%

Without Gravity Constraint:
  FEA  - Round  Wires: 0.4328 mm       Ratio: 12.87%
  FEA  - Square Wires: 1.2925 mm       Ratio: 75.10%
  CLPT - Round  Wires: 0.4708 mm       Ratio: 20.39%
  CLPT - Square Wires: 0.5355 mm       Ratio: 27.84%
```

```
%%%%%%%%%%%%%%%%%%%%%%%%%%%%%%%%%%%%%%%%%%%%%%%%%%%%%%%%%%%%%%%%%%%%%%%
%   Mean Hausdorff Distances   %%   Relative Difference Ratio  %
%%%%%%%%%%%%%%%%%%%%%%%%%%%%%%%%%%%%%%%%%%%%%%%%%%%%%%%%%%%%%%%%%%%%%%%
      -----     Displaying Comparison to Trial 3:     -----

With Gravity Constraint:
  FEA  - Round  Wires: 1.1095 mm       Ratio: 64.87%
  FEA  - Square Wires: 1.2779 mm       Ratio: 73.94%

Without Gravity Constraint:
  FEA  - Round  Wires: 0.3744 mm       Ratio: 14.69%
  FEA  - Square Wires: 1.3240 mm       Ratio: 75.62%
  CLPT - Round  Wires: 0.4449 mm       Ratio: 22.05%
  CLPT - Square Wires: 0.5244 mm       Ratio: 29.35%

%%%%%%%%%%%%%%%%%%%%%%%%%%%%%%%%%%%%%%%%%%%%%%%%%%%%%%%%%%%%%%%%%%%%%%%
%   Mean Hausdorff Distances   %%   Relative Difference Ratio  %
%%%%%%%%%%%%%%%%%%%%%%%%%%%%%%%%%%%%%%%%%%%%%%%%%%%%%%%%%%%%%%%%%%%%%%%
      -----     Displaying Comparison to Trial 4:     -----

With Gravity Constraint:
  FEA  - Round  Wires: 1.0680 mm       Ratio: 63.90%
  FEA  - Square Wires: 1.2346 mm       Ratio: 73.22%

Without Gravity Constraint:
  FEA  - Round  Wires: 0.4058 mm       Ratio: 12.34%
  FEA  - Square Wires: 1.2869 mm       Ratio: 74.94%
  CLPT - Round  Wires: 0.4896 mm       Ratio: 19.90%
  CLPT - Square Wires: 0.5458 mm       Ratio: 27.40%

%%%%%%%%%%%%%%%%%%%%%%%%%%%%%%%%%%%%%%%%%%%%%%%%%%%%%%%%%%%%%%%%%%%%%%%
%   Mean Hausdorff Distances   %%   Relative Difference Ratio  %
%%%%%%%%%%%%%%%%%%%%%%%%%%%%%%%%%%%%%%%%%%%%%%%%%%%%%%%%%%%%%%%%%%%%%%%
      -----     Displaying Comparison to Trial 5:     -----

With Gravity Constraint:
  FEA  - Round  Wires: 1.0467 mm       Ratio: 63.53%
  FEA  - Square Wires: 1.2136 mm       Ratio: 72.95%

Without Gravity Constraint:
  FEA  - Round  Wires: 0.3875 mm       Ratio: 11.45%
  FEA  - Square Wires: 1.2630 mm       Ratio: 74.69%
  CLPT - Round  Wires: 0.4308 mm       Ratio: 19.09%
  CLPT - Square Wires: 0.4975 mm       Ratio: 26.66%
```

```
%%%%%%%%%%%%%%%%%%%%%%%%%%%%%%%%%%%%%%%%%%%%%%%%%%%%%%%%%%%%%%%%%%%%%%%%%%%%
%%                                %%                                %%
%%  AVG MHD Across All Trials     %%  Relative Difference Ratio     %%
%%                                %%                                %%
%%%%%%%%%%%%%%%%%%%%%%%%%%%%%%%%%%%%%%%%%%%%%%%%%%%%%%%%%%%%%%%%%%%%%%%%%%%%
With Gravity Constraint:
  FEA  - Round  Wires: 1.1159 mm       Ratio: 64.92%
  FEA  - Square Wires: 1.2829 mm       Ratio: 73.97%

Without Gravity Constraint:
  FEA  - Round  Wires: 0.4358 mm       Ratio: 14.81%
  FEA  - Square Wires: 1.3329 mm       Ratio: 75.65%
  CLPT - Round  Wires: 0.5006 mm       Ratio: 22.16%
  CLPT - Square Wires: 0.5684 mm       Ratio: 29.44%

  EXP MHD Std Dev (5 Trials):  0.0924 mm

%%%%%%%%%%%%%%%%%%%%%%%%%%%%%%%%%%%%%%%%%%%%%%%%%%%%%%%%%%%%%%%%%%%%%%%%%%%%
%%                                                                %%
%%  Surfaced Averaged Radius of Curvature                         %%
%%                                                                %%
%%%%%%%%%%%%%%%%%%%%%%%%%%%%%%%%%%%%%%%%%%%%%%%%%%%%%%%%%%%%%%%%%%%%%%%%%%%%
  EXP - Surface Trial 1: 68.1 mm
  EXP - Surface Trial 2: 61.6 mm
  EXP - Surface Trial 3: 70.8 mm
  EXP - Surface Trial 4: 71.4 mm
  EXP - Surface Trial 5: 66.7 mm
  ---> 5  Trial Average: 67.7 mm
  ---> 5  Trial Std Dev: 3.9 mm
  ---> Relative Std Dev: 5.8%

With Gravity Constraint:
  FEA  - Round  Wires: 76.2 mm. Diff: 8.4 mm (12.5%)
  FEA  - Square Wires: 86.9 mm. Diff: 19.1 mm (28.2%)

Without Gravity Constraint:
  FEA  - Round  Wires: 41.5 mm. Diff: 26.3 mm (38.8%)
  FEA  - Square Wires: 140.0 mm. Diff: 72.3 mm (106.8%)
  CLPT - Round  Wires: 47.1 mm. Diff: 20.7 mm (30.5%)
  CLPT - Square Wires: 43.6 mm. Diff: 24.2 mm (35.7%)
```

```
%%%%%%%%%%%%%%%%%%%%%%%%%%%%%%%%
%  Sample Properties Compared  %
%%%%%%%%%%%%%%%%%%%%%%%%%%%%%%%%

  Nominal Thickness: 1.2 mm
  Wire Spacing:      3.3 mm
  Wire Diameter:     0.3 mm
  Temperature:       361.6 K
  Div. per Dim.:     150 divisions

%%%%%%%%%%%%%%%%%%%%%%%%%%%%%%%%%%%%%%%%%%%%%%%%%%%%%%%%%%%%%%%%%%%%%%%%%%%%%%%
%   Mean Hausdorff Distances   %%   Relative Difference Ratio  %
%%%%%%%%%%%%%%%%%%%%%%%%%%%%%%%%%%%%%%%%%%%%%%%%%%%%%%%%%%%%%%%%%%%%%%%%%%%%%%%
      -----     Displaying Comparison to Trial 1:     -----

With Gravity Constraint:
  FEA  - Round  Wires: 1.4380 mm       Ratio: 79.61%
  FEA  - Square Wires: 1.4960 mm       Ratio: 83.30%

Without Gravity Constraint:
  FEA  - Round  Wires: 1.3056 mm       Ratio: 45.02%
  FEA  - Square Wires: 1.2009 mm       Ratio: 65.49%
  CLPT - Round  Wires: 0.7729 mm       Ratio: 38.36%
  CLPT - Square Wires: 0.8686 mm       Ratio: 43.51%

%%%%%%%%%%%%%%%%%%%%%%%%%%%%%%%%%%%%%%%%%%%%%%%%%%%%%%%%%%%%%%%%%%%%%%%%%%%%%%%
%   Mean Hausdorff Distances   %%   Relative Difference Ratio  %
%%%%%%%%%%%%%%%%%%%%%%%%%%%%%%%%%%%%%%%%%%%%%%%%%%%%%%%%%%%%%%%%%%%%%%%%%%%%%%%
      -----     Displaying Comparison to Trial 2:     -----

With Gravity Constraint:
  FEA  - Round  Wires: 1.4660 mm       Ratio: 79.91%
  FEA  - Square Wires: 1.5245 mm       Ratio: 83.55%

Without Gravity Constraint:
  FEA  - Round  Wires: 1.3154 mm       Ratio: 45.84%
  FEA  - Square Wires: 1.2252 mm       Ratio: 66.01%
  CLPT - Round  Wires: 0.7813 mm       Ratio: 39.28%
  CLPT - Square Wires: 0.8784 mm       Ratio: 44.35%
```

```
%%%%%%%%%%%%%%%%%%%%%%%%%%%%%%%%%%%%%%%%%%%%%%%%%%%%%%%%%%%%%%%%%%%%%%%%%%%%
%   Mean Hausdorff Distances   %%   Relative Difference Ratio  %
%%%%%%%%%%%%%%%%%%%%%%%%%%%%%%%%%%%%%%%%%%%%%%%%%%%%%%%%%%%%%%%%%%%%%%%%%%%%
      -----     Displaying Comparison to Trial 3:     -----

With Gravity Constraint:
  FEA  - Round  Wires: 1.4944 mm       Ratio: 80.24%
  FEA  - Square Wires: 1.5536 mm       Ratio: 83.82%

Without Gravity Constraint:
  FEA  - Round  Wires: 1.3430 mm       Ratio: 46.73%
  FEA  - Square Wires: 1.2524 mm       Ratio: 66.57%
  CLPT - Round  Wires: 0.8039 mm       Ratio: 40.28%
  CLPT - Square Wires: 0.9018 mm       Ratio: 45.27%

%%%%%%%%%%%%%%%%%%%%%%%%%%%%%%%%%%%%%%%%%%%%%%%%%%%%%%%%%%%%%%%%%%%%%%%%%%%%
%   Mean Hausdorff Distances   %%   Relative Difference Ratio  %
%%%%%%%%%%%%%%%%%%%%%%%%%%%%%%%%%%%%%%%%%%%%%%%%%%%%%%%%%%%%%%%%%%%%%%%%%%%%
      -----     Displaying Comparison to Trial 4:     -----

With Gravity Constraint:
  FEA  - Round  Wires: 1.4936 mm       Ratio: 80.36%
  FEA  - Square Wires: 1.5539 mm       Ratio: 83.91%

Without Gravity Constraint:
  FEA  - Round  Wires: 1.3499 mm       Ratio: 47.04%
  FEA  - Square Wires: 1.2509 mm       Ratio: 66.76%
  CLPT - Round  Wires: 0.8205 mm       Ratio: 40.63%
  CLPT - Square Wires: 0.9176 mm       Ratio: 45.59%

%%%%%%%%%%%%%%%%%%%%%%%%%%%%%%%%%%%%%%%%%%%%%%%%%%%%%%%%%%%%%%%%%%%%%%%%%%%%
%   Mean Hausdorff Distances   %%   Relative Difference Ratio  %
%%%%%%%%%%%%%%%%%%%%%%%%%%%%%%%%%%%%%%%%%%%%%%%%%%%%%%%%%%%%%%%%%%%%%%%%%%%%
      -----     Displaying Comparison to Trial 5:     -----

With Gravity Constraint:
  FEA  - Round  Wires: 1.3972 mm       Ratio: 78.99%
  FEA  - Square Wires: 1.4548 mm       Ratio: 82.80%

Without Gravity Constraint:
  FEA  - Round  Wires: 1.2305 mm       Ratio: 43.36%
  FEA  - Square Wires: 1.1588 mm       Ratio: 64.45%
  CLPT - Round  Wires: 0.7180 mm       Ratio: 36.50%
  CLPT - Square Wires: 0.8127 mm       Ratio: 41.81%
```

```
%%%%%%%%%%%%%%%%%%%%%%%%%%%%%%%%%%%%%%%%%%%%%%%%%%%%%%%%%%%%%%%%%%%%%%%%%%%%
%%                                %%                                %%
%%  AVG MHD Across All Trials     %%  Relative Difference Ratio     %%
%%                                %%                                %%
%%%%%%%%%%%%%%%%%%%%%%%%%%%%%%%%%%%%%%%%%%%%%%%%%%%%%%%%%%%%%%%%%%%%%%%%%%%%
With Gravity Constraint:
  FEA  - Round  Wires: 1.4579 mm       Ratio: 79.83%
  FEA  - Square Wires: 1.5165 mm       Ratio: 83.49%

Without Gravity Constraint:
  FEA  - Round  Wires: 1.3089 mm       Ratio: 45.63%
  FEA  - Square Wires: 1.2176 mm       Ratio: 65.88%
  CLPT - Round  Wires: 0.7793 mm       Ratio: 39.04%
  CLPT - Square Wires: 0.8758 mm       Ratio: 44.14%

  EXP MHD Std Dev (5 Trials):  0.0474 mm

%%%%%%%%%%%%%%%%%%%%%%%%%%%%%%%%%%%%%%%%%%%%%%%%%%%%%%%%%%%%%%%%%%%%%%%%%%%%
%%                                                                %%
%%  Surfaced Averaged Radius of Curvature                         %%
%%                                                                %%
%%%%%%%%%%%%%%%%%%%%%%%%%%%%%%%%%%%%%%%%%%%%%%%%%%%%%%%%%%%%%%%%%%%%%%%%%%%%
  EXP - Surface Trial 1: 64.2 mm
  EXP - Surface Trial 2: 65.8 mm
  EXP - Surface Trial 3: 66.7 mm
  EXP - Surface Trial 4: 64.2 mm
  EXP - Surface Trial 5: 67.3 mm
  ---> 5  Trial Average: 65.6 mm
  ---> 5  Trial Std Dev: 1.4 mm
  ---> Relative Std Dev: 2.2%

With Gravity Constraint:
  FEA  - Round  Wires: 133.5 mm. Diff: 67.9 mm (103.4%)
  FEA  - Square Wires: 169.8 mm. Diff: 104.1 mm (158.6%)

Without Gravity Constraint:
  FEA  - Round  Wires: 63.5 mm. Diff: 2.1 mm (3.3%)
  FEA  - Square Wires: 91.4 mm. Diff: 25.8 mm (39.2%)
  CLPT - Round  Wires: 65.9 mm. Diff: 0.2 mm (0.3%)
  CLPT - Square Wires: 59.5 mm. Diff: 6.1 mm (9.4%)
```